

ABSTRACT

OZCAN, SEYMA NUR. Development of Well-Balanced and Asymptotic Preserving Numerical Methods for Partial Differential Equations . (Under the direction of Dr. Alina Chertock.)

In the context of this dissertation, we focus on numerical solutions of two separate models which are encountered in physical and biological studies.

We begin with hyperbolic balance laws and develop a second-order well-balanced central-upwind scheme for various systems of these types of equations, in particular, the models of isothermal gas dynamics with source, traffic flow with relaxation to equilibrium velocities and Euler equations of gas dynamics with gravitation are considered. The proposed scheme is capable of exactly preserving state-state solutions expressed in terms of nonlocal equilibrium variables. The new scheme is based on modifications in the reconstruction and evolution steps of a Godunov-type central-upwind method. The crucial step in the construction of the second-order scheme is a well-balanced piecewise linear reconstruction of equilibrium variables, which is combined with a well-balanced evolution in time, achieved by reducing the amount of numerical viscosity (present at the central-upwind scheme) in the areas where the flow is at (near) steady-state regime. We show the performance of our newly developed central-upwind scheme and demonstrate importance of perfect balance between the fluxes and gravitational forces on a number of one- and two-dimensional examples.

The second part is devoted to the chemotaxis phenomena, taken from biological applications, that describes the biased motion of cells in response to the chemical substance in a medium. We study a two-dimensional multiscale chemotaxis model based on a combination of the macroscopic evolution equation for chemoattractant and the microscopic model for cell evolution. The latter is governed by a Boltzmann-type kinetic equation with a local turning kernel operator which describes the velocity change of the cells. The parabolic scaling yields a non-dimensional kinetic model with a small parameter, which represents the ratio of the mean free path and the typical length scale. We propose a new asymptotic preserving numerical scheme that reflects the convergence of the studied micro-macro model to its macroscopic counterpart—the Patlak-Keller-Segel system—in the singular limit. The method is based on the operator splitting strategy and suitable higher-order time discretizations. In particular, we use the so-called even-odd decoupling and approximate the stiff terms arising in the singular limit implicitly. We prove that the resulting

scheme satisfies the asymptotic preserving property. More precisely, it yields a consistent approximation of the Patlak-Keller-Segel system as the scaling parameter tends to 0. The performance of the proposed scheme is illustrated via a number of numerical experiments.

© Copyright 2017 by Seyma Nur Ozcan

All Rights Reserved

Development of Well-Balanced and Asymptotic Preserving Numerical Methods
for Partial Differential Equations

by
Seyma Nur Ozcan

A dissertation submitted to the Graduate Faculty of
North Carolina State University
in partial fulfillment of the
requirements for the Degree of
Doctor of Philosophy

Applied Mathematics

Raleigh, North Carolina

2017

APPROVED BY:

Dr. Mansoor Haider

Dr. Zhillin Li

Dr. Semyon Tsynkov

Dr. Alina Chertock
Chair of Advisory Committee

DEDICATION

...To My Benevolent Parents...
(...Fedakar Anne ve Babama...)

BIOGRAPHY

Şeyma Nur was born in Simav, a small town in western Turkey. She spent her childhood in Istanbul and then moved to Mersin and Konya due to her father's job, which is being an excellent teacher of Turkish literature. Ever since, Şeyma's goal has always been to become a math teacher. To pursue her dreams, she returned to Istanbul for her undergraduate education. She received a bachelor's degree in mathematics from Bogazici University and a master's degree in mathematics from Fatih University. During her master's study, she earned a scholarship from Turkish Ministry of National Education for a Ph.D. program in the United States. After getting an acceptance from North Carolina State University, she moved to Raleigh in 2011. Since then she has been chasing after her childhood dream of becoming a mathematician.

ACKNOWLEDGEMENTS

First of all, words are not enough to express my gratitude to my advisor, Dr. Alina Chertock. Without her guidance, support, and infinite patience, it would have been impossible for me to complete my graduate study. I have learned many valuable lessons from her in both mathematical and real-life aspects.

I would like to especially thank Dr. Alexander Kurganov for his collaboration and fruitful discussions and want to thank Dr. Mária Lukáčová-Medviďová for her hospitality, kindness, and collaboration. To my other collaborators Dr. Eitan Tadmor, Dr. Micheal Herty, and Dr. Shumo Cui; I appreciate your significant contributions to my research.

I am thankful to Dr. Mansoor Haider, Dr. Zhillin Li, Dr. Semyon Tsynkov, Dr. Kazik Borkowski, for serving on my dissertation committee and giving supportive feedbacks. I would like to add my special thanks to the wonderful staff of the Mathematics department. To Lexy Baracca, Şeyma Bennett-Shabbir, Brendae' Hughes, Denise Seabrooks, thank you all for your willingness to help with anything I needed.

I would like to acknowledge the Turkish Ministry of National Education, National Science Foundation, and KI-Net for the funds they provided me. I also thank the Center for Research in Scientific Computation (CRSC) for their support during my last year of studies, especially to Dr. H. Thomas Banks and Lesa Denning for their valued assistance.

I want to name a few of my friends and classmates, Tülay Ayyıldız, Esra Öztürk, Melissa Strait, Hengrui Hu, Andrew Bernstein, Karlan Wolfkil for their help, encouragement, and friendship. To my roommates, Zeynep Büsra, Perihan, Elif and Sümeyye; I am glad to have your support during this long journey.

To my first teachers and permanent supporters, my parents Naciye and Şaban, thank you for your priceless presences and all your sacrifices. To my sisters Sümeyra and Sevde, my brother Selim, I am very grateful for having you and your joyful support in my life.

My heartfelt thanks go to the Turkish community in North Carolina that has become a new family for me. I know that whenever I need anything, someone will be willing to help.

Finally, to Ceyda and Berra, thank you both for bringing extra energy to my life!

TABLE OF CONTENTS

LIST OF TABLES	vii
LIST OF FIGURES	viii
Chapter 1 Introduction	1
1.1 Hyperbolic Conservation/Balance Laws	2
1.2 Kinetic Chemotaxis Models	6
1.3 Outline of the Dissertation	9
 I Hyperbolic Balance Laws	 10
Chapter 2 Well-Balanced Central-Upwind Schemes	11
2.1 Second-Order Semi-Discrete Central-Upwind Scheme - Overview	11
2.1.1 One-Dimensional Central-Upwind Scheme	12
2.1.2 Two-Dimensional Central-Upwind Scheme	14
2.2 2×2 Systems of Balance Laws	17
2.2.1 Well-Balanced Central-Upwind Scheme	19
2.2.2 Numerical Examples	22
2.3 The One-Dimensional Euler Equations of Gas Dynamics With Gravitation	32
2.3.1 Well-Balanced Central-Upwind Scheme	34
2.3.2 Numerical Examples	38
2.4 The Two-Dimensional Euler Equations of Gas Dynamics With Gravitation	45
2.4.1 Well-Balanced Central-Upwind Scheme	46
2.4.2 Numerical Examples	51
2.5 Conclusions	55
 II Kinetic Chemotaxis Models	 57
Chapter 3 An Asymptotic Preserving Scheme for Kinetic Chemotaxis Models in Two Space Dimensions	58
3.1 Introduction	58
3.2 Local Turning Kernel	61
3.3 Numerical Method	62
3.3.1 Even-Odd Formulation	62
3.3.2 Operator Splitting	65
3.4 AP Property	74

3.5	Numerical Results	76
3.6	Conclusions	84
BIBLIOGRAPHY		86
APPENDIX		99
Appendix A	Time Integration	100
A.1	The Third-Order Strong Stability Preserving Runge-Kutta Methods . . .	100

LIST OF TABLES

Table 2.1	Example 2.4: L^1 -errors and corresponding experimental convergence rates in the well-balanced computation of K and L at $T = 1$. .	23
Table 2.2	Example 2.4: L^1 -errors and corresponding experimental convergence rates in the non-well-balanced computation of K and L at $T = 1$	24
Table 2.3	Example 2.5: L^1 -errors and corresponding experimental convergence rates in the well-balanced computation of K and L at $T = 1$. .	26
Table 2.4	Example 2.5: L^1 -errors and corresponding experimental convergence rates in the non-well-balanced computation of K and L at $T = 1$	26
Table 2.5	Example 2.6: L^1 -errors and corresponding experimental convergence rates in the well-balanced computation of K and L at $T = 1$. .	29
Table 2.6	Example 2.6: L^1 -errors and corresponding experimental convergence rates in the non-well-balanced computation of K and L at $T = 1$	30
Table 2.7	Example 2.3: L^1 -errors and corresponding experimental convergence rates in the non-well-balanced computation of ρ , ρv and E ; $\phi(y) = \frac{1}{2}y^2$	42
Table 2.8	Example 2.3: L^1 -errors and corresponding experimental convergence rates in the non-well-balanced computation of ρ , ρv and E ; $\phi(y) = \sin(2\pi y)$	42
Table 2.9	Example 2.7: L^1 -errors for the non-well-balanced CU scheme.	52
Table 3.1	Example 3.2b: L^∞ - errors for $M = 8, 9.5$ and 11 (from left to right). .	82

LIST OF FIGURES

Figure 1.1	Central (staggered) control volume (left), $F_j^n = F(q(x_j, t^n))$. Upwind control volume (right), $F_{j-1/2}^n = F(q(x_{j-1/2}, t^n))$	4
Figure 1.2	Central-upwind control volumes. The solution is nonsmooth in the blue colored control volume and it is smooth in the green control volume.	5
Figure 1.3	Model of AP schemes. P_ε : a continuous problem; P_0 : a well-posed limiting problem of P_ε ; $P_{\varepsilon,h}$: a stable discretization of P_ε ; $P_{0,h}$: a stable discretization of P_0	8
Figure 2.1	Example 2.4: Momentum perturbation computed by the well-balanced (WB) and non-well-balanced (NWB) schemes at time $T = 0.2$ for $\eta = 10^{-3}$ (left) and $\eta = 10^{-6}$ (right).	25
Figure 2.2	Example 2.5: Momentum perturbations computed by the well-balanced (WB) and non-well-balanced (NWB) schemes for $\eta = 10^{-1}$ (left) and $\eta = 10^{-3}$ (right) at time $T = 0.25$	27
Figure 2.3	Example 2.6: Perturbations on the equilibrium variable K (left column) and L (right column), computed by the well-balanced (WB) and non-well-balanced (NWB) schemes at time $T = 0.1$ for $\eta = 10^{-7}$	31
Figure 2.4	Sketch of $H(\psi)$, (2.63).	37
Figure 2.5	Example 2.1: Solutions computed by the well-balanced CU scheme using $N = 100$ and 2000 cells.	40
Figure 2.6	Example 2.2: Pressure perturbation $(p(y, 0.25) - e^{-y})$ computed by the well-balanced (WB) and non-well-balanced (Non-WB) CU schemes with $N = 200$ and 2000 for $\eta = 10^{-2}$ (left) and $\eta = 10^{-4}$ (right).	41
Figure 2.7	Example 2.3: Pressure perturbation $(p(y, 0.25) - e^{-y^2/2})$ computed by the well-balanced (WB) and non-well-balanced (Non-WB) CU schemes for $\eta = 10^{-5}$ with $N = 200$ for each scheme (left) and $N = 1600$ for the non-well-balanced scheme (right). The reference solution is computed with $N = 2000$ grid pints.	44
Figure 2.8	Example 2.3: Pressure perturbation $(p(y, 0.25) - e^{-\sin(2\pi y)})$ computed by the well-balanced (WB) and non-well-balanced (Non-WB) CU schemes for $\eta = 10^{-3}$ with $N = 200$ for each scheme (left) and $N = 2000$ for the non-well-balanced scheme (right). The reference solution is computed with $N = 2000$ grid pints.	44
Figure 2.9	Example 2.7: Pressure perturbation computed by the well-balanced (left) and non-well-balanced (right) CU schemes using 50×50 uniform cells.	53

Figure 2.10	Example 2.7: Contour plot of the pressure perturbation computed by well-balanced (left column) and non-well-balanced (right column) CU schemes using 50×50 (upper row) and 200×200 (lower row) uniform cells.	54
Figure 2.11	Example 2.8: Density (ρ) and velocity ($\sqrt{u^2 + v^2}$) computed by the well-balanced CU scheme.	55
Figure 2.12	Example 2.8: Density (ρ) and velocity ($\sqrt{u^2 + v^2}$) computed by the non-well-balanced CU scheme.	56
Figure 3.1	Example 3.1: Behavior of $\ \rho\ _\infty/M$ in time for varying values of M ; $N_x = N_y = 128$	78
Figure 3.2	Example 3.1: Behavior of $\ \rho\ _\infty$ in time for $M = 7$ (left) and $M = 9$ (right) on three consecutive meshes.	78
Figure 3.3	Example 3.2a: Behavior of $\ \rho\ _\infty$ in time for $M = 1$ (left), $M = 8$ (middle) and $M = 11$ (right) on four consecutive meshes.	80
Figure 3.4	Example 3.2a: The density $\rho(x, y, T = 0.0005)$ for $M = 11$ computed on the meshes with: $N_x = N_y = 128$ (left) and $N_x = N_y = 256$ (right).	80
Figure 3.5	Example 3.2b: Behavior of $\ \rho\ _\infty$ in time for $M = 8$ (left), $M = 9.5$ (middle) and $M = 11$ (right) on three consecutive meshes.	81
Figure 3.6	Example 3.3: The displacement of the density for $M = 3$	83
Figure 3.7	Example 3.3: The displacement of the density for $M = 7$	83
Figure 3.8	Example 3.3: The displacement of the density for $M = 11$	84

CHAPTER 1

Introduction

In this dissertation, we study two distinct sets of systems that arise in various physical and biological applications.

The first part of the dissertation is devoted to the development of novel numerical methods for hyperbolic conservation laws with the source term, so-called hyperbolic balance laws, in which non-smooth solutions and complicated wave structures may appear. In the second part, we numerically study multiscale chemotaxis models, which are based on macroscopic evolution equations for the chemoattractant concentration coupled with a microscopic model for the cell evolution.

In this introductory chapter, we provide a brief overview of existing shock-capturing methods used to numerically solve the hyperbolic conservation/balance laws and asymptotically preserving methods used to resolve multiscale phenomena.

1.1 Hyperbolic Conservation/Balance Laws

We consider a multi-dimensional system of hyperbolic conservation laws:

$$\mathbf{q}_t + \nabla_x \cdot \mathbf{F}(\mathbf{q}) = 0, \quad (1.1)$$

where $\mathbf{x} \in \mathbb{R}^d$ and $t \in \mathbb{R}^+$ are the spatial and time variables, $\mathbf{q}(\mathbf{x}, t)$ is the vector of conserved variables and $\mathbf{F}(\mathbf{q})$ is the vector of flux terms. The main difficulty in numerically solving the system (1.1) is due to the loss of smoothness even if the initial condition is smooth. Typically, the solutions of (1.1) possess complicated nonlinear structures such as shock and rarefaction waves. Capturing such solutions in an accurate, efficient and robust way requires the use of high-resolution shock capturing techniques, see, e.g. [55, 62, 118, 139, 144, 157].

Godunov-type finite-volume methods, first established in [57], are one of the most typical numerical methods to solve (1.1) due to their accurate and non-oscillatory shock capturing procedure. Those are reconstruction-evolution-projection methods, in which the numerical solution is first realized in terms of cell averages over specific control volumes. These cell-averages are then used to construct a global piece-wise polynomial solution which is evolved in time and finally projected back onto the original grid.

For instance, consider the one-dimensional (1-D) system of conservation laws:

$$\mathbf{q}_t + \mathbf{F}(\mathbf{q})_x = 0. \quad (1.2)$$

The cell averages of the computed solution at a certain time level t^n are obtained by integrating the solution over the spatial grid cells $C_j := [x_{j-\frac{1}{2}}, x_{j+\frac{1}{2}}]$, which is taken to be uniform for simplicity, of size $|C_j| = \Delta x$:

$$\bar{\mathbf{q}}_j^n \approx \frac{1}{\Delta x} \int_{C_j} \mathbf{q}(x, t^n) dx. \quad (1.3)$$

Then, following the Godunov scheme's approach, the approximate solution at time t^n is reconstructed by a global piecewise polynomial:

$$\tilde{\mathbf{q}}(x, t^n) \approx \mathbf{p}_j^n(x), \quad \text{for } x \in (x_{j-\frac{1}{2}}, x_{j+\frac{1}{2}}), \quad (1.4)$$

where p_j^n are polynomial pieces that are generically discontinuous at the cell interfaces $x = x_{j\pm\frac{1}{2}}$. A library of different reconstruction procedures is available, see, e.g. [2, 36, 56, 63, 64, 80, 90, 97, 109, 111, 112, 115, 118–120, 126, 141, 143, 148, 152]. Next, the reconstructed piecewise polynomial interpolant is used as initial data at $t = t^n$, which is evolved to the next time level $t = t^{n+1}$ by integrating the system (1.2) over space-time control volumes $C_j \times [t^n, t^{n+1}]$.

Depending on the choice of the control volume, Godunov-type schemes are mainly split into two subclasses: *central* and *upwind*, as shown in Figure 1.1.

Central (staggered) schemes allow one to evolve the solution without (approximately) solving any Riemann problems, in which the cell averages are computed over the centered grid rather than the original computational cells:

$$\bar{q}_{j+\frac{1}{2}}^{n+1} = \frac{1}{2\Delta x} \left(\int_{x_j}^{x_{j+\frac{1}{2}}} p_j^n(x) dx + \int_{x_{j+\frac{1}{2}}}^{x_{j+1}} p_{j+1}^n(x) dx \right) - \frac{1}{\Delta x} \int_{t^n}^{t^{n+1}} [F(q(x_{j+1}, t)) - F(q(x_j, t))] dt. \quad (1.5)$$

Here, the flux integrals can be evaluated exactly, since the solution $q(x, t)$ is smooth along the lines $x = x_{j\pm\frac{1}{2}}$ for $t \in [t^n, t^{n+1}]$ provided a suitable time-step restriction.

The first-order central schemes were introduced in the 1950s, [51, 106], and called *Lax-Friedrichs (LF) schemes* in the literature. LF schemes are simple and universal to apply due to their *Riemann-problem-solver-free* feature, since particularly in multi-dimensional problems, Riemann problem solvers do not exist. Central schemes have been broadly developed including staggered and nonstaggered variants, higher-order methods, multidimensional generalizations, see, e.g. [4, 10, 35, 81, 91, 96, 97, 103, 104, 111, 112, 114, 117, 120, 126, 131–133, 138].

On the other hand, in the upwind schemes, also proposed in the 1950s, [57], the solution cell averages at $t = t^{n+1}$ are obtained by approximating the integrals on the right-hand side of

$$\bar{q}_j^{n+1} = \bar{q}_j^n - \frac{1}{\Delta x} \int_{t^n}^{t^{n+1}} [F(q(x_{j+\frac{1}{2}}, t)) - F(q(x_{j-\frac{1}{2}}, t))] dt. \quad (1.6)$$

Since the solution $q(x, t^n)$ is discontinuous at $x = x_{j\pm\frac{1}{2}}$, an (approximate) solution of the (generalized) Riemann problems arising at the cell interfaces is required, see, e.g., [9, 14, 36, 56, 57, 90, 109, 150]. Thus, these schemes are restricted to the systems, in which

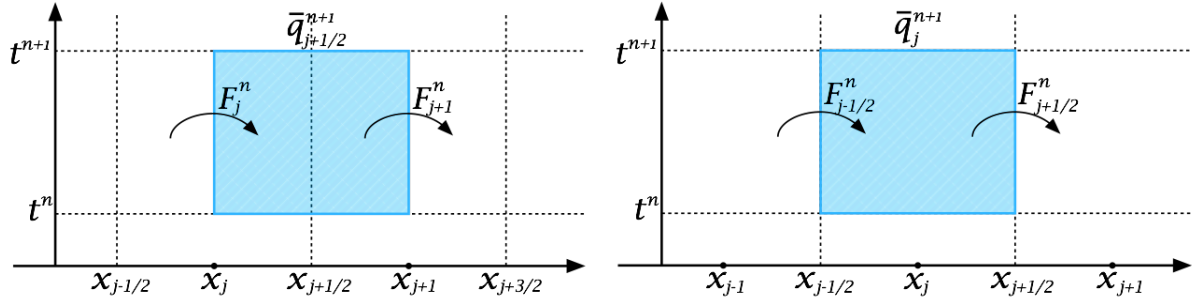


Figure 1.1 Central (staggered) control volume (left), $F_j^n = F(q(x_j, t^n))$. Upwind control volume (right), $F_{j-1/2}^n = F(q(x_{j-1/2}, t^n))$.

Riemann problem solvers are available. However, they are highly accurate, less dissipative and less diffusive than central schemes, since the latter does not catch the resolution of nonlinear waves, which causes a larger numerical dissipation.

Recently, a new class of Godunov-type finite-volume methods –*central-upwind (CU) schemes*– has been developed by combining the simplicity and universality of the central scheme with the high accuracy and low dissipation of the upwind approach. The key idea behind the construction of the CU schemes is to use the *upwinding* information, that is the one-sided *local* speeds of propagation of the waves emerging at cell interfaces. These are right- and left-sided speeds, which allow one to design two special sets of control volumes as shown in Figure 1.2. One of these control volumes (colored with blue in Figure 1.2) contains all (nonsmooth) nonlinear waves generated at time $t = t^n$ at cell interfaces while the second one (colored with green in Figure 1.2) contains smooth parts of the solution. The stability condition, if chosen properly, would then, guarantee that no waves reach the boundaries, hence the evolution mechanism within the control volumes remain *central* and no Riemann problem solver is required. Once evolved in time, the solution must be, as usual, projected back on the original uniform grid.

The CU schemes were initially introduced in [103] for hyperbolic systems of conservation laws and further developed in [19, 20, 38, 93, 95–99, 101, 102, 105]. These schemes are efficient, highly accurate and do not require any (approximate) Riemann problem solver (the latter makes the CU schemes applicable in a “black-box manner” to a wide variety of multidimensional hyperbolic systems of conservation and balance laws). As it is

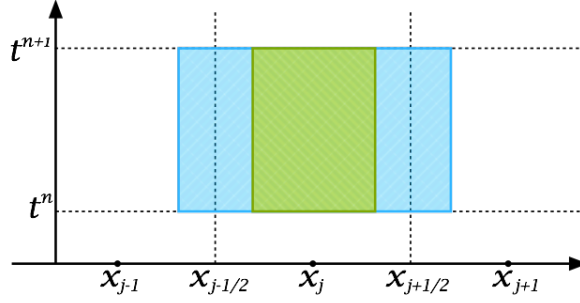


Figure 1.2 Central-upwind control volumes. The solution is nonsmooth in the blue colored control volume and it is smooth in the green control volume.

demonstrated in [93, 95], the CU scheme has reduced numerical dissipation and enhanced resolution of contact waves.

Solving the system of conservation laws (1.1) with additional source terms, i.e. the system of balance laws, makes the development of the solution a more complicated task. A system of balance laws reads:

$$q_t + \nabla_x \cdot F(q) = S(q), \quad (1.7)$$

where $S(q)$ is the vector of source terms. In many applications, a special class of solutions to (1.7), *steady-state solutions*, are of particular interest and especially important in cases when small perturbations of the steady states are considered as solutions of the system (1.7). Capturing such solutions numerically is one of the major difficulties since the size of these perturbations may be smaller than the size of the truncation error on a coarse grid. To overcome this difficulty, one can use a very fine grid, but in many physically relevant situations this may be computationally unaffordable. Another problem one may come across while solving the system of balance laws (1.7) is preserving the positivity of the computed solution of physically relevant problems. The numerical oscillations may cause negative values for physical quantities, such as, density, pressure or water height.

Therefore, it is important to design a well-balanced and positivity preserving, i.e. *structure preserving*, numerical scheme, that is, a method which is capable of exactly preserving some steady-state solutions as well as maintaining the positivity of the numerical solution when it is necessitated by the physical application. Then, perturbations of these solutions

will be resolved on a coarse grid in a non-oscillatory way. Well-balanced schemes were introduced in [61] and mainly developed in the context of shallow water equations; see, e.g., [5, 11, 12, 18, 29, 49, 53, 83, 86, 92, 100, 108, 127, 136, 137, 140, 155]. Positivity preserving well-balanced schemes for shallow water equations can be reviewed in, for example, [5, 11, 12, 18, 28, 53, 92, 100]. Some of these schemes have been extended for the Euler equations with gravitational fields. In [110], quasi-steady wave-propagation methods were developed for models with a static gravitational field. In [13], well-balanced finite-volume methods, which preserve a certain class of steady states, were derived for nearly hydrostatic flows. In recent works [26, 43, 151], finite-volume methods that preserve more general classes of steady states and handle more general gravitational potentials have been introduced. In [121, 149, 156], gas-kinetic schemes were extended to the multidimensional gas dynamic equations and well-balanced numerical methods were developed for problems in which the gravitational potential was modeled by a piecewise step function. More recently, higher order finite-difference [154] and finite-volume [113] methods for the gas dynamics with gravitation have been introduced.

1.2 Kinetic Chemotaxis Models

The second part of the dissertation is focused on the study of the oriented movement of cells in response to a chemical gradient (chemoattractant), so-called *chemotaxis* phenomena.

Chemotaxis can be represented by a multiscale model which involves a class of Boltzmann-type kinetic equation for the evolution of the cell density and a macroscopic equation for the chemoattractant concentration. This model was introduced in [147] based on a stochastic approach and further developed by the kinetic theory in [3, 129, 145] for the chemotaxis. The non-dimensionalized system reads as:

$$\begin{aligned}\varepsilon f_t + \mathbf{v} \cdot \nabla_{\mathbf{x}} f &= \frac{1}{\varepsilon} \mathcal{T}(f), \\ \tau S_t &= \Delta S + \psi(S, \rho),\end{aligned}\tag{1.8}$$

where $f(\mathbf{x}, t, \mathbf{v})$ is the local density of cells at the position $\mathbf{x} \in \mathbb{R}^d$ with the velocity $\mathbf{v} \in V \subset \mathbb{R}^d$ at time t , the gradient term $\mathbf{v} \cdot \nabla_{\mathbf{x}} f$ describes the transport of cells with \mathbf{v} and the turning

kernel operator \mathcal{T} expresses the rate of change from the velocity v' to v . $S(x, t)$ and $\rho(x, t)$ are the macroscopic density of the chemoattractant and cells, respectively. The interaction between cells and the chemoattractant is given by the function ψ . The non-dimensional scaling parameter ε is the ratio of the average distance travelled between two velocity changes (the mean free path) and the typical length scale.

The diffusion limit of the multiscale chemotaxis system (1.8) has been extensively studied within the last few decades. For example, some of the literature can be found in [1, 3, 23–25, 68, 71, 76, 79, 130, 135, 153] and references therein. Under certain assumptions, the limiting problem as $\varepsilon \rightarrow 0$ results in the macroscopic system of equations for the cell density and chemoattractant concentration, known as *Patlak-Keller-Segel (PKS) system*, [134] and [87, 88]:

$$\begin{aligned}\rho_t &= \nabla \cdot (\nabla \rho - \chi \rho \nabla S), \\ \tau S_t &= \Delta S + \psi(S, \rho),\end{aligned}\tag{1.9}$$

where χ is the chemotactic sensitivity constant.

Since solutions of the system (1.8) reveal a multiscale character, their numerical resolution generates some major difficulties. For instance, the limiting solutions of (1.8) as $\varepsilon \rightarrow 0$ may be different in nature from that of the solutions for finite values of $\varepsilon > 0$. As was shown in a number of analytical works, the solution of the PKS system (1.9) may blowup under certain regimes, [21, 34, 52, 65–67, 69, 78, 124], while the behavior of solution to the kinetic chemotaxis model (1.8) depends on the choice of the turning kernel and may not blowup as the solution of the PKS model, see, e.g. [15, 25, 76, 77].

From the numerical point of view, the use of standard explicit numerical methods in the $\varepsilon \rightarrow 0$ regime, would require very restrictive time and space discretization steps: typically they would need to be proportional to ε as $\Delta t, \Delta x \sim \mathcal{O}(\varepsilon)$ or $\Delta t, \Delta x \sim \mathcal{O}(\varepsilon^2)$, due to stability conditions. This rapidly becomes too costly from a practical point of view and consequently numerical solutions for small values of ε may be out of reach. Moreover, standard implicit schemes, which will be uniformly stable for $0 < \varepsilon < 1$, may be inconsistent with the limit problem and thus may provide a wrong solution when $\varepsilon \rightarrow 0$. Thus, designing robust numerical methods, whose accuracy and efficiency is independent of ε is an important and challenging task, which is the focus of this dissertation.

One of the most powerful numerical techniques applicable to such problems is asymptotic-

preserving (AP) methods, originally introduced in [82] to solve kinetic equations in diffusive regimes and were later generalized for a variety of kinetic models; see, e.g., [39, 40, 44, 47, 73–75, 79, 84, 107]. The idea behind the AP methods is proposing a numerical transition from one model to another, which is able to be preserved at the discrete level. More specifically, for a fixed mesh size and time step, an AP scheme should be automatically transformed into a stable discretization of the limiting model as $\varepsilon \rightarrow 0$. An illustrative description of AP schemes is shown in Figure 1.3, where P_ε stands for the continuous problem with its limit problem P_0 and $P_{\varepsilon,h}$ is the stable discretization of the problem P_ε with $h = (\Delta t, \Delta x)$. As $\varepsilon \rightarrow 0$, the AP scheme, $P_{\varepsilon,h}$, results in a consistent discretization $P_{0,h}$ for P_0 as well.

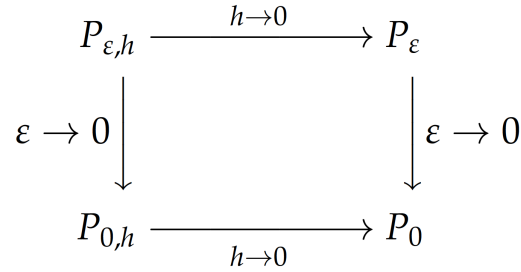


Figure 1.3 Model of AP schemes. P_ε : a continuous problem; P_0 : a well-posed limiting problem of P_ε ; $P_{\varepsilon,h}$: a stable discretization of P_ε ; $P_{0,h}$: a stable discretization of P_0 .

To review the properties of AP schemes referring to Figure 1.3, [73, 125]:

- Consider a continuous problem P_ε and its well-posed limiting problem P_0
- For fixed $\varepsilon > 0$, $P_{\varepsilon,h}$ is a stable discretization of P_ε with a given time and space discretization $h = (\Delta t, \Delta x)$
- For fixed discretization $h = (\Delta t, \Delta x)$, $P_{\varepsilon,h}$ tends to an accurate discretization of P_0
- The stability of the scheme does not rely on ε

In the context of the kinetic chemotaxis model, a 1-D AP method has been designed for various turning kernels in [23]. Additionally, a numerical investigation has been done for

the 2-D spherically symmetric initial data in $\varepsilon = 1$ regime. Moreover, for 1-D models, an AP scheme based on a micro-macro decomposition has been proposed and implemented in [8]. Recently, in [45], a general framework to design an AP scheme has been proposed for the transport equation that models chemotaxis.

1.3 Outline of the Dissertation

The rest of the dissertation is organized as follows.

- In Chapter 2, we describe a second-order semi-discrete CU scheme and illustrate its well-balanced modifications for several systems of equations. Particularly, In Section 2.2, we consider 2×2 balance laws, while in Sections 2.3 and 2.4 the Euler equations of gas dynamics with gravitation in both one- and two-dimensional spaces are considered, respectively. In Section 2.2.2, we provide a number of examples to demonstrate the performance of the prescribed well-balanced numerical scheme for 2×2 systems of balance laws. In Sections 2.3.2 and 2.4.2, we examine the validity of the proposed well-balanced method on several numerical examples for one- and two-dimensional Euler equations with gravitation.
- In Chapter 3, we characterize a micro-macro model for chemotaxis and develop an AP scheme to resolve the multiscale phenomena of the system. In Section 3.3, we present the AP scheme The performance of the proposed AP scheme is illustrated in a number of numerical experiments in Section 3.5.

Part I

Hyperbolic Balance Laws

CHAPTER 2

Well-Balanced Central-Upwind Schemes

The contents of this chapter have been submitted to SIAM Journal on Scientific Computing, [27] and Proceedings of the Sixteenth International Conference on Hyperbolic Problems: Theory, Numerics, Applications, [30].

In this chapter, we first outline a second-order CU scheme from [93] in Section 2.1. We start with considering 2×2 systems of balance laws in Section 2.2 and present how the described CU scheme can be modified to preserve the steady states of the system. In Section 2.3 and Section 2.4, we illustrate the well-balanced modifications of the CU scheme for 1-D and 2-D Euler equations of gas dynamics with gravitation, respectively. In Sections 2.2.2, 2.3.2 and 2.4.2, we implement the proposed CU scheme on a number of numerical examples.

2.1 Second-Order Semi-Discrete Central-Upwind Scheme - Overview

In this section, we briefly describe a second-order semi-discrete CU scheme from [93] applied to the 1-D in Section 2.1.1 and 2-D systems in Section 2.1.2.

2.1.1 One-Dimensional Central-Upwind Scheme

For simplicity, we first partition the computational domain into finite-volume cells $C_j := [x_{j-\frac{1}{2}}, x_{j+\frac{1}{2}}]$ of size $|C_j| = \Delta x$ centered at x_j , $j = j_L, \dots, j_R$. We assume that at time level t , the cell averages of the numerical solution, $\bar{q}_j(t) := \frac{1}{\Delta x} \int_{C_j} q(x, t) dx$, are available.

We consider the following 1-D system

$$q_t + F(q)_x = S(q), \quad (2.1)$$

where $q(x, t)$ is the vector of unknown variables, F and S are the vectors of the flux and source terms and we apply the semi-discrete CU scheme which results in the following system of ODEs:

$$\frac{d}{dt} \bar{q}_j = -\frac{\mathcal{F}_{j+\frac{1}{2}} - \mathcal{F}_{j-\frac{1}{2}}}{\Delta x} + \bar{S}_j, \quad (2.2)$$

where

$$\mathcal{F}_{j+\frac{1}{2}} := \frac{a_{j+\frac{1}{2}}^+ F(q_j^E) - a_{j+\frac{1}{2}}^- F(q_{j+1}^W)}{a_{j+\frac{1}{2}}^+ - a_{j+\frac{1}{2}}^-} + \alpha_{j+\frac{1}{2}} (q_{j+1}^W - q_j^E - \delta q_{j+\frac{1}{2}}), \quad \alpha_{j+\frac{1}{2}} := \frac{a_{j+\frac{1}{2}}^+ a_{j+\frac{1}{2}}^-}{a_{j+\frac{1}{2}}^+ - a_{j+\frac{1}{2}}^-} \quad (2.3)$$

are the CU numerical fluxes, and \bar{S}_j are the approximations of the cell averages of the source term. In (2.3),

$$\delta q_{j+\frac{1}{2}} = \minmod(q_{j+1}^W - q_{j+\frac{1}{2}}^*, q_{j+\frac{1}{2}}^* - q_j^E) \quad (2.4)$$

is a built-in anti-diffusion term with

$$q_{j+\frac{1}{2}}^* = \frac{a_{j+\frac{1}{2}}^+ q_{j+1}^W - a_{j+\frac{1}{2}}^- q_j^E - \{F(q_{j+1}^W) - F(q_j^E)\}}{a_{j+\frac{1}{2}}^+ - a_{j+\frac{1}{2}}^-}, \quad (2.5)$$

and the minmod function defined by

$$\minmod(z_1, z_2, \dots) := \begin{cases} \min(z_1, z_2, \dots), & \text{if } z_i > 0 \ \forall i, \\ \max(z_1, z_2, \dots), & \text{if } z_i < 0 \ \forall i, \\ 0, & \text{otherwise.} \end{cases} \quad (2.6)$$

In (2.3), (2.4) and (2.5), q_j^E and q_{j+1}^W are the one-sided point values of the computed solution at cell interfaces $x = x_{j+\frac{1}{2}}$. To construct a second-order scheme, these variables are to be calculated using the piecewise linear reconstruction

$$\tilde{q}(x, t) = \sum_j (\bar{q}_j(t) + (q_x)_j(x - x_j)) \cdot \chi_{C_j}(x), \quad (2.7)$$

where χ_{C_j} is a characteristic function of the interval C_j . We then obtain

$$q_j^E := \tilde{q}(x_{j+\frac{1}{2}} - 0) = \bar{q}_j + \frac{\Delta x}{2}(q_x)_j, \quad q_{j+1}^W := \tilde{q}(x_{j+\frac{1}{2}} + 0) = \bar{q}_{j+1} - \frac{\Delta x}{2}(q_x)_{j+1}. \quad (2.8)$$

To avoid oscillations, the vertical slopes in (2.8), $(q_x)_j$, are to be computed using a nonlinear limiter applied to the cell averages $\{\bar{q}_j\}$. In all of the numerical experiments presented in Section 2.3.2, we have used a generalized minmod limiter (see, e.g., [115, 126, 148]) applied in the component-wise manner:

$$(q_x)_j = \text{minmod} \left(\theta \frac{\bar{q}_{j+1} - \bar{q}_j}{\Delta x}, \frac{\bar{q}_{j+1} - \bar{q}_{j-1}}{2\Delta x}, \theta \frac{\bar{q}_j - \bar{q}_{j-1}}{\Delta x} \right),$$

where the parameter $\theta \in [1, 2]$ controls the amount of numerical dissipation: the use of larger values of θ typically leads to a less dissipative, but more oscillatory scheme.

The one-sided local speeds of propagation, $a_{j+\frac{1}{2}}^\pm$, are estimated using the smallest λ_1 and largest λ_N eigenvalues of the Jacobian matrix $\partial \mathbf{F}(\mathbf{q}) / \partial \mathbf{q}$:

$$\begin{aligned} a_{j+\frac{1}{2}}^+ &= \max \left\{ \lambda_N \left(\frac{\partial \mathbf{F}}{\partial \mathbf{q}}(q_j^E) \right), \lambda_N \left(\frac{\partial \mathbf{F}}{\partial \mathbf{q}}(q_{j+1}^W) \right), 0 \right\}, \\ a_{j+\frac{1}{2}}^- &= \min \left\{ \lambda_1 \left(\frac{\partial \mathbf{F}}{\partial \mathbf{q}}(q_j^E) \right), \lambda_1 \left(\frac{\partial \mathbf{F}}{\partial \mathbf{q}}(q_{j+1}^W) \right), 0 \right\}. \end{aligned} \quad (2.9)$$

Finally, the semi-discrete ODE system, (2.2) should be integrated in time by a high-order accurate and stable ODE solver. For example, in the numerical examples presented in Sections 2.2.2 and 2.3.2, we use the third-order strong stability preserving (SSP) Runge-Kutta method (see, e.g., [58, 60, 144] and Appendix A.1). In order to make computations

stable, the time step should be chosen with the following CFL condition:

$$\Delta t = \kappa \frac{\Delta x}{\max_j |a_{j+\frac{1}{2}}^\pm|}, \quad \kappa \leq \frac{1}{2}. \quad (2.10)$$

2.1.2 Two-Dimensional Central-Upwind Scheme

In this section, we implement a second-order semi-discrete CU scheme, [93], to the following 2-D system:

$$\mathbf{q}_t + \mathbf{F}(\mathbf{q})_x + \mathbf{G}(\mathbf{q})_y = \mathbf{S}(\mathbf{q}), \quad (2.11)$$

where $\mathbf{q}(x, y, t)$ is the vector of unknown variables, \mathbf{F} and \mathbf{G} are the fluxes in x - and y -directions, respectively, and \mathbf{S} is the source term.

We consider a rectangular computational domain and divide it into the uniform Cartesian cells $C_{j,k} := [x_{j-\frac{1}{2}}, x_{j+\frac{1}{2}}] \times [y_{k-\frac{1}{2}}, y_{k+\frac{1}{2}}]$ of size $|C_{j,k}| = \Delta x \Delta y$ centered at (x_j, y_k) , $j = j_L, \dots, j_R$, $k = k_L, \dots, k_R$. We assume that at a certain time level t , the cell averages of the computed numerical solution,

$$\bar{\mathbf{q}}_{j,k}(t) := \frac{1}{\Delta x \Delta y} \iint_{C_{j,k}} \mathbf{q}(x, y, t) dx dy,$$

are available.

We employ the semi-discrete CU scheme which leads to the following system of ODEs:

$$\frac{d}{dt} \bar{\mathbf{q}}_{j,k} = -\frac{\mathcal{F}_{j+\frac{1}{2},k} - \mathcal{F}_{j-\frac{1}{2},k}}{\Delta x} - \frac{\mathcal{G}_{j,k+\frac{1}{2}} - \mathcal{G}_{j,k-\frac{1}{2}}}{\Delta y} + \bar{\mathbf{S}}_{j,k}, \quad (2.12)$$

where

$$\begin{aligned} \mathcal{F}_{j+\frac{1}{2},k} &:= \frac{a_{j+\frac{1}{2},k}^+ \mathbf{F}(\mathbf{q}_{j,k}^E) - a_{j+\frac{1}{2},k}^- \mathbf{F}(\mathbf{q}_{j+1,k}^W)}{a_{j+\frac{1}{2},k}^+ - a_{j+\frac{1}{2},k}^-} + \alpha_{j+\frac{1}{2},k} \left(\mathbf{q}_{j+1,k}^W - \mathbf{q}_{j,k}^E - \delta \mathbf{q}_{j+\frac{1}{2},k} \right), \\ \alpha_{j+\frac{1}{2},k} &:= \frac{a_{j+\frac{1}{2},k}^+ a_{j+\frac{1}{2},k}^-}{a_{j+\frac{1}{2},k}^+ - a_{j+\frac{1}{2},k}^-} \end{aligned} \quad (2.13)$$

$$\mathcal{G}_{j,k+\frac{1}{2}} := \frac{b_{j,k+\frac{1}{2}}^+ G(q_{j,k}^N) - b_{j,k+\frac{1}{2}}^- G(q_{j,k+1}^S)}{b_{j,k+\frac{1}{2}}^+ - b_{j,k+\frac{1}{2}}^-} + \beta_{j,k+\frac{1}{2}} (q_{j,k+1}^S - q_{j,k}^N - \delta q_{j,k+\frac{1}{2}}), \quad (2.14)$$

$$\beta_{j,k+\frac{1}{2}} := \frac{b_{j,k+\frac{1}{2}}^+ b_{j,k+\frac{1}{2}}^-}{b_{j,k+\frac{1}{2}}^+ - b_{j,k+\frac{1}{2}}^-}$$

are the CU numerical fluxes, and \bar{S}_{jk} is the approximations of the cell averages of the source term and

$$\delta q_{j+\frac{1}{2},k} = \min\text{mod}(q_{j+1,k}^W - q_{j+\frac{1}{2},k}^*, q_{j+\frac{1}{2},k}^* - q_{j,k}^E) \quad (2.15)$$

and

$$\delta q_{j,k+\frac{1}{2}} = \min\text{mod}(q_{j,k+1}^S - q_{j,k+\frac{1}{2}}^*, q_{j,k+\frac{1}{2}}^* - q_{j,k}^N) \quad (2.16)$$

are build-in anti-diffusion terms with

$$q_{j+\frac{1}{2},k}^* = \frac{a_{j+\frac{1}{2},k}^+ q_{j+1,k}^W - a_{j+\frac{1}{2},k}^- q_{j,k}^E - \{F(q_{j+1,k}^W) - F(q_{j,k}^E)\}}{a_{j+\frac{1}{2},k}^+ - a_{j+\frac{1}{2},k}^-},$$

and

$$q_{j,k+\frac{1}{2}}^* = \frac{b_{j,k+\frac{1}{2}}^+ q_{j,k+1}^S - b_{j,k+\frac{1}{2}}^- q_{j,k}^N - \{G(q_{j,k+1}^S) - G(q_{j,k}^N)\}}{b_{j,k+\frac{1}{2}}^+ - b_{j,k+\frac{1}{2}}^-},$$

with the minmod function defined in (2.6). Notice that the anti-diffusion terms (2.15) and (2.16) can be rigorously derived from the fully discrete CU framework; see [93] for details, though they are slightly different from the ones presented in [93].

The one-sided point values of the computed solution at cell interfaces $(x_{j\pm\frac{1}{2}}, y_k)$ and $(x_j, y_{k\pm\frac{1}{2}})$ are obtained using the piecewise linear reconstruction:

$$\tilde{q}(x, y) = \sum_{j,k} [\bar{q}_{j,k} + (q_x)_{j,k}(x - x_j) + (q_y)_{j,k}(y - y_k)] \cdot \chi_{C_{j,k}(x,y)}, \quad (2.17)$$

where $\chi_{C_{j,k}}$ is a characteristic function of the finite-volume-cell $C_{j,k}$.

We then obtain

$$\mathbf{q}_{j,k}^E := \tilde{\mathbf{q}}(x_{j+\frac{1}{2},k} - 0) = \bar{\mathbf{q}}_{j,k} + \frac{\Delta x}{2}(\mathbf{q}_x)_{j,k}, \quad \mathbf{q}_{j+1,k}^W := \tilde{\mathbf{q}}(x_{j+\frac{1}{2},k} + 0) = \bar{\mathbf{q}}_{j+1,k} - \frac{\Delta x}{2}(\mathbf{q}_x)_{j+1,k}, \quad (2.18)$$

$$\mathbf{q}_{j,k}^N := \tilde{\mathbf{q}}(y_{j,k+\frac{1}{2}} - 0) = \bar{\mathbf{q}}_{j,k} + \frac{\Delta y}{2}(\mathbf{q}_y)_{j,k}, \quad \mathbf{q}_{j,k+1}^S := \tilde{\mathbf{q}}(y_{j,k+\frac{1}{2}} + 0) = \bar{\mathbf{q}}_{j,k+1} - \frac{\Delta y}{2}(\mathbf{q}_y)_{j,k+1}. \quad (2.19)$$

Similarly to the 1-D case, to avoid oscillations, the slopes $(\mathbf{q}_x)_{j,k}$ and $(\mathbf{q}_y)_{j,k}$ are computed with a nonlinear limiter, for example, the generalized minmod limiter:

$$\begin{aligned} (\mathbf{q}_x)_{j,k} &= \text{minmod} \left(\theta \frac{\bar{\mathbf{q}}_{j+1,k} - \bar{\mathbf{q}}_{j,k}}{\Delta x}, \frac{\bar{\mathbf{q}}_{j+1,k} - \bar{\mathbf{q}}_{j-1,k}}{2\Delta x}, \theta \frac{\bar{\mathbf{q}}_{j,k} - \bar{\mathbf{q}}_{j-1,k}}{\Delta x} \right), \\ (\mathbf{q}_y)_{j,k} &= \text{minmod} \left(\theta \frac{\bar{\mathbf{q}}_{j,k+1} - \bar{\mathbf{q}}_{j,k}}{\Delta y}, \frac{\bar{\mathbf{q}}_{j,k+1} - \bar{\mathbf{q}}_{j,k-1}}{2\Delta y}, \theta \frac{\bar{\mathbf{q}}_{j,k} - \bar{\mathbf{q}}_{j,k-1}}{\Delta y} \right). \end{aligned} \quad (2.20)$$

We then estimate the one-sided local speeds of propagation in the x - and y - directions, respectively, using the smallest and largest eigenvalues of the Jacobians $\frac{\partial \mathbf{F}}{\partial \mathbf{q}}$ and $\frac{\partial \mathbf{G}}{\partial \mathbf{q}}$:

$$\begin{aligned} a_{j+\frac{1}{2},k}^+ &= \max \left(\lambda_N \left(\frac{\partial \mathbf{F}}{\partial \mathbf{q}}(\mathbf{q}_{j,k}^E) \right), \lambda_N \left(\frac{\partial \mathbf{F}}{\partial \mathbf{q}}(\mathbf{q}_{j+1,k}^W) \right), 0 \right), \\ a_{j+\frac{1}{2},k}^- &= \min \left(\lambda_1 \left(\frac{\partial \mathbf{F}}{\partial \mathbf{q}}(\mathbf{q}_{j,k}^E) \right), \lambda_1 \left(\frac{\partial \mathbf{F}}{\partial \mathbf{q}}(\mathbf{q}_{j+1,k}^W) \right), 0 \right), \\ b_{j,k+\frac{1}{2}}^+ &= \max \left(\lambda_N \left(\frac{\partial \mathbf{G}}{\partial \mathbf{q}}(\mathbf{q}_{j,k}^N) \right), \lambda_N \left(\frac{\partial \mathbf{G}}{\partial \mathbf{q}}(\mathbf{q}_{j,k+1}^S) \right), 0 \right), \\ b_{j,k+\frac{1}{2}}^- &= \min \left(\lambda_1 \left(\frac{\partial \mathbf{G}}{\partial \mathbf{q}}(\mathbf{q}_{j,k}^N) \right), \lambda_1 \left(\frac{\partial \mathbf{G}}{\partial \mathbf{q}}(\mathbf{q}_{j,k+1}^S) \right), 0 \right), \end{aligned} \quad (2.21)$$

where $\lambda_1 < \dots < \lambda_N$ are the N eigenvalues of the corresponding Jacobians.

Finally, a sufficiently accurate and stable ODE solver, for example, the third-order SSP Runge-Kutta method (see, e.g. [58, 60, 144] and Appendix A.1), is used to solve the ODE system (2.12) with a modified CFL condition:

$$\Delta t = \kappa \min \left\{ \frac{\Delta x}{\max_{j,k} |a_{j+\frac{1}{2},k}^\pm|}, \frac{\Delta y}{\max_{j,k} |b_{j,k+\frac{1}{2}}^\pm|} \right\}, \quad \kappa \leq \frac{1}{2}. \quad (2.22)$$

Remark 2.1.1 It should be observed, that the CU schemes, (2.1)-(2.9) or (2.11)-(2.21), do not, in general, preserve steady state solutions when applied to systems of balance laws. In what follows, we explain the well-balanced adjustments of the prescribed CU schemes, (2.1)-(2.9) and (2.11)-(2.21), in regard to several models.

2.2 2×2 Systems of Balance Laws

In this section, we consider a 2×2 system of balance laws of the following form:

$$\begin{cases} \rho_t + f_1(\rho, q)_x = 0, \\ q_t + f_2(\rho, q)_x = -s(\rho, q), \end{cases} \quad (2.23)$$

which can be rewritten in the vector form as

$$\mathbf{q}_t + \mathbf{F}(\mathbf{q})_x = \mathbf{S}(\mathbf{q}), \quad (2.24)$$

where

$$\mathbf{q} := \begin{pmatrix} \rho \\ q \end{pmatrix}, \quad \mathbf{F}(\mathbf{q}) := \begin{pmatrix} f_1(\rho, q) \\ f_2(\rho, q) \end{pmatrix}, \quad \mathbf{S}(\mathbf{q}) := \begin{pmatrix} 0 \\ -s(\rho, q) \end{pmatrix}, \quad (2.25)$$

are the vectors of the conservative variables, flux and source terms, respectively, and $x \in \mathbb{R}$ and $t \in \mathbb{R}^+$ are the spatial and time variables. These type of balance laws systems appear as mathematical models in many applications, see, e.g., [16, 41, 42, 50, 54]. System (2.23) is also a common model for gas flow in high-pressure transmission pipelines [7, 128] and traffic flow [6, 37], both will be our primary motivation for designing a numerical method and validating computational results in this section.

The steady states, $\rho_t = q_t = 0$, of (2.23) satisfy the following time-independent system:

$$\begin{cases} f_1(\rho, q)_x = 0, \\ f_2(\rho, q)_x = -s(\rho, q), \end{cases} \quad (2.26)$$

as well as $f_1(\rho, q)_t = f_2(\rho, q)_t = s(\rho, q)_t = 0$, which yields

$$f_1(\rho, q) \equiv \text{Const}, \quad f_2(\rho, q) + \int^x s(\rho, q) d\xi \equiv \text{Const}, \quad \forall x, t. \quad (2.27)$$

The goal is to construct a numerical scheme which is able to preserve the given steady states (2.27) and their small perturbations. To this end, we incorporate the source term into the flux in the second equation of the system (2.23) and introduce a new reconstruction-evolution process to guarantee that all steady states of (2.23) are captured exactly. Following [27, 29], we introduce new equilibrium variables, which are preserved during the reconstruction and propagate in time according to a modified evolution step.

It is instructive to note that the scheme described in Section 2.1 does not necessarily preserve the steady state solutions (2.27). To cite an example, we consider the case where $f_1(\rho, q) = q$ and therefore $q = \text{Const}$ and $\rho = \rho(x)$ satisfies the steady state (2.27). Implementing the CU scheme (2.2)–(2.9) with $\delta \mathbf{q}_{j+\frac{1}{2}} \equiv 0$ in (2.3) for, say, the first component of the solution will result in the following semi-discrete approximation:

$$\begin{aligned} \frac{d\bar{\rho}_j}{dt} = & -\frac{1}{\Delta x} \left[\frac{a_{j+\frac{1}{2}}^+ q_j^E - a_{j+\frac{1}{2}}^- q_{j+1}^W}{a_{j+\frac{1}{2}}^+ - a_{j+\frac{1}{2}}^-} + \alpha_{j+\frac{1}{2}} (\rho_{j+1}^W - \rho_j^E) \right. \\ & \left. - \frac{a_{j-\frac{1}{2}}^+ q_{j-1}^E - a_{j-\frac{1}{2}}^- q_j^W}{a_{j-\frac{1}{2}}^+ - a_{j-\frac{1}{2}}^-} + \alpha_{j-\frac{1}{2}} (\rho_j^W - \rho_{j-1}^E) \right]. \end{aligned}$$

The last equation reduces to

$$\frac{d\bar{\rho}_j}{dt} = -\frac{\alpha_{j+\frac{1}{2}} (\rho_{j+1}^W - \rho_j^E) - \alpha_{j-\frac{1}{2}} (\rho_j^W - \rho_{j-1}^E)}{\Delta x}, \quad (2.28)$$

since $q_j^E = q_{j+1}^W = q_{j-1}^E = q_j^W = \text{Const}$. However, in general, the piecewise linear approximation, (2.7), forms discontinuities at the cell interfaces, so that the point values ρ_{j+1}^W and ρ_j^E (ρ_j^W and ρ_{j-1}^E) are not necessarily equal. Thus, right hand side of the ODE (2.28) does not vanish and the scheme fails to preserve the steady state.

2.2.1 Well-Balanced Central-Upwind Scheme

In this section, we present a well-balanced modification of the CU scheme described in Section 2.1. To this end, we first define new variables:

$$K := f_1(\rho, q), \quad \text{and} \quad L := f_2(\rho, q) + R, \quad R := \int^x s(\rho, q) d\xi, \quad (2.29)$$

and rewrite the system (2.23) as:

$$\begin{cases} \rho_t + K_x = 0, \\ q_t + L_x = 0, \end{cases} \quad (2.30)$$

which can be put into the vector form (2.24) with the different flux and zero source terms: where $\mathbf{q} = (\rho, q)^T$, $\mathbf{F}(\mathbf{q}) = (K, L)^T$ and $\mathbf{S}(\mathbf{q}) \equiv (0, 0)^T$. Obviously, the steady state of (2.30) will be in the following form:

$$K \equiv \text{Const}, \quad L \equiv \text{Const}. \quad (2.31)$$

2.2.1.1 Reconstruction

We start by describing a special reconstruction procedure, which is implemented to obtain the point values, \mathbf{q}_j^E and \mathbf{q}_{j+1}^W , used in (2.3), and is based on reconstructing equilibrium variables, K and L , instead of conservative ones, ρ and q . To this end, we first compute the values K_j and L_j from the cell averages, $\bar{\rho}_j$ and \bar{q}_j , i.e.,

$$K_j = f_1(\bar{\rho}_j, \bar{q}_j), \quad L_j = f_2(\bar{\rho}_j, \bar{q}_j) + R_j, \quad (2.32)$$

where the values of R_j are evaluated by applying the midpoint quadrature rule to the integral in (2.29) and using the following recursive relation:

$$R_j = \frac{1}{2}(R_{j-\frac{1}{2}} + R_{j+\frac{1}{2}}), \quad R_{j+\frac{1}{2}} = R(x_{j+\frac{1}{2}}) = R_{j-\frac{1}{2}} + \Delta x s(\bar{\rho}_j, \bar{q}_j), \quad (2.33)$$

starting from $R_{1/2} \equiv 0$.

The point values of K and L at the cell interfaces $x = x_{j \pm \frac{1}{2}}$ are then obtained from

(2.7)–(2.6):

$$\begin{aligned} K_j^E &= K_j + \frac{\Delta x}{2}(K_x)_j, & L_j^E &= L_j + \frac{\Delta x}{2}(L_x)_j, \\ K_j^W &= K_j - \frac{\Delta x}{2}(K_x)_j, & L_j^W &= L_j - \frac{\Delta x}{2}(L_x)_j. \end{aligned} \quad (2.34)$$

Finally, equipped with the values of $K_j^{E,W}$, $L_j^{E,W}$ and $R_{j\pm\frac{1}{2}}$, we compute the corresponding point values of ρ and q by solving the following four nonlinear equations in terms of $\rho_j^E, \rho_j^W, q_j^E$ and q_j^W , respectively:

$$\begin{aligned} K_j^E &= f_1(\rho_j^E, q_j^E), & L_j^E &= f_2(\rho_j^E, q_j^E) + R_{j+\frac{1}{2}}, \\ K_j^W &= f_1(\rho_j^W, q_j^W), & L_j^W &= f_2(\rho_j^W, q_j^W) + R_{j-\frac{1}{2}}. \end{aligned}$$

Clearly, the procedure would significantly simplify when one of the conservative variables is also an equilibrium one, say, $K = f_1(\rho, q) = q$. In such case, the point values $q_j^{E,W}$ can be obtained directly from (2.6)–(2.7) and thus only two nonlinear equations should be solved to obtain $\rho_j^{E,W}$ for each j . In all of our examples presented below, the set of nonlinear equations (2.34) was solved analytically.

2.2.1.2 Evolution

We then evolve the cell averages, $\bar{q}_j = (\bar{\rho}_j, \bar{q}_j)^T$, in time by using the following system of ODEs:

$$\frac{d}{dt} \bar{q}_j = - \frac{\mathcal{F}_{j+\frac{1}{2}} - \mathcal{F}_{j-\frac{1}{2}}}{\Delta x}. \quad (2.35)$$

Here, we take the built-in anti-diffusion term $q_{j+\frac{1}{2}} \equiv 0$ in the numerical fluxes $\mathcal{F}_{j\pm\frac{1}{2}}$ whose two components are given as follows:

$$\begin{aligned}
\mathcal{F}_{j+\frac{1}{2}}^{(1)} &= \frac{a_{j+\frac{1}{2}}^+ K_j^E - a_{j+\frac{1}{2}}^- K_{j+1}^W}{a_{j+\frac{1}{2}}^+ - a_{j+\frac{1}{2}}^-} \\
&\quad + \alpha_{j+\frac{1}{2}} (\rho_{j+1}^W - \rho_j^E) \mathcal{H} \left(\frac{|K_{j+1} - K_j|}{\Delta x} \cdot \frac{|\Omega|}{\max_j \{K_j, K_{j+1}\}} \right), \\
\mathcal{F}_{j+\frac{1}{2}}^{(2)} &= \frac{a_{j+\frac{1}{2}}^+ L_j^E - a_{j+\frac{1}{2}}^- L_{j+1}^W}{a_{j+\frac{1}{2}}^+ - a_{j+\frac{1}{2}}^-} \\
&\quad + \alpha_{j+\frac{1}{2}} (q_{j+1}^W - q_j^E) \mathcal{H} \left(\frac{|L_{j+1} - L_j|}{\Delta x} \cdot \frac{|\Omega|}{\max_j \{L_j, L_{j+1}\}} \right),
\end{aligned} \tag{2.36}$$

and $\alpha_{j+\frac{1}{2}}$ is defined in (2.3) with the corresponding one-sided local speeds $a_{j+\frac{1}{2}}^\pm$, which are estimated by using the smallest and largest eigenvalues of the Jacobian $\partial \mathbf{F} / \partial \mathbf{q}$.

The second components in the numerical flux functions (2.36) are modified (compared to (2.3)) to preserve the steady states. Namely, a smooth function \mathcal{H} , satisfying

$$\mathcal{H}(\phi) = \frac{(C\phi)^m}{1 + (C\phi)^m}, \quad \mathcal{H}(0) = 0, \tag{2.37}$$

is introduced for some constants $C > 0$ and $m > 0$. When the solution is a steady state, e.g. both $K_j^E = K_{j+1}^W = K_j \equiv \text{Const}$ and $L_j^E = L_{j+1}^W = L_j \equiv \text{Const}$, \mathcal{H} vanishes, so is each component of the numerical flux in (2.36). Otherwise, \mathcal{H} is very close to 1 and then the scheme reduces to the classical semi-discrete central upwind scheme (2.3). The normalization factors, $\frac{|\Omega|}{\max_j \{K_j, K_{j+1}\}}$ and $\frac{|\Omega|}{\max_j \{L_j, L_{j+1}\}}$, where $|\Omega|$ is the size of the computational domain, are introduced in order to make the function \mathcal{H} nondimensional and independent of the choice of C and m .

We summarize this observation in the following theorem.

Theorem 2.2.1 *The semi-discrete CU scheme, (2.35)–(2.37), with the reconstruction described in Section 2.2.1.1 gives an absolute balance between the source and flux terms and thus preserves the steady state, (2.27), exactly, i.e. the scheme is well-balanced.*

Proof: Let us start with assuming that at a certain time level t the solution reaches its steady state and

$$K_j^E = K_{j+1}^W = K_j \equiv K^* \quad \text{and} \quad L_j^E = L_{j+1}^W = L_j \equiv L^*, \quad \forall j, \tag{2.38}$$

where K^* and L^* are constants. We show that $\bar{q}_j = (\bar{\rho}_j, \bar{q}_j)^T$ remains constant in time, which means the right-hand side of the ODE system (2.35) diminishes with given conditions (2.66). Indeed, identities in (2.66) imply $\mathcal{H} = 0$, which in turns results in $\mathcal{F}_{j+\frac{1}{2}}^{(1)} = K^*$ and $\mathcal{F}_{j+\frac{1}{2}}^{(2)} = L^*$. Therefore, both $\mathcal{F}_{j+\frac{1}{2}}^{(1)} - \mathcal{F}_{j-\frac{1}{2}}^{(1)} = 0$ and $\mathcal{F}_{j+\frac{1}{2}}^{(2)} - \mathcal{F}_{j-\frac{1}{2}}^{(2)} = 0$ and thus from (2.35) we obtain $\frac{d\bar{q}_j}{dt} = 0, \forall j$. ■

2.2.2 Numerical Examples

In this section, we test the performance of the developed well-balanced method and show that it preserves steady state solutions exactly for several 2×2 systems. In particular, the system of isothermal Euler equations of gas dynamics with friction and with the bottom profile and the model for traffic flow with relaxation are studied.

In all of the experiments reported below, we implemented the second-order well-balanced CU scheme (2.35)–(2.37) and compared the obtained results with those computed by the non well-balanced CU scheme (2.1)–(2.3). The scheme parameters were taken as $\theta = 1.3$ in Examples 2.4, 2.5 and $\theta = 1$ in Example 2.6; $C = 200$ in Examples 2.4, 2.6 and $C = 400$ in Example 2.5 and $m = 1$ in (2.37) in all of the examples. For the time evolution, we used the third-order SSP Runge-Kutta method (see, e.g., [58, 60, 144] and Appendix A.1) to solve the semi-discrete ODE system (2.35) with the CFL constant in (2.10) taken as $\kappa = 0.4$ in Examples 2.4, 2.6 and $\kappa = 0.1$ in Example 2.5.

Example 2.4—Gas dynamics with pipe-wall friction.

In this example, we solve the isothermal Euler equations of gas dynamics with pipe-wall friction, which is used for the simulation of high-pressure gas transmission systems [17, 128]. The model is governed by the following system of hyperbolic balance laws:

$$\begin{cases} \rho_t + q_x = 0, \\ q_t + \left(c^2 \rho + \frac{q^2}{\rho} \right)_x = -\mu \frac{q}{\rho} |q|, \end{cases} \quad (2.39)$$

Table 2.1 Example 2.4: L^1 -errors and corresponding experimental convergence rates in the well-balanced computation of K and L at $T = 1$.

N	$\ K(\cdot, 1) - K^*\ _1$	$\ L(\cdot, 1) - L^*\ _1$
100	1.94E-18	7.77E-18
200	9.71E-19	9.71E-18
400	1.66E-18	9.57E-18
800	2.18E-18	1.18E-17

where, $\rho(x, t)$ is the density of the fluid with the velocity $u(x, t)$, $q(x, t)$ is the momentum, $\mu > 0$ is the friction coefficient (divided by the pipe cross section) and $c > 0$ is the speed of sound.

We first check the well-balanced property of the developed scheme by considering (2.39) with $c = \mu = 1$ and subject to the following initial data (given in terms of equilibrium variables):

$$K(x, 0) = q(x, 0) = K^* = 0.15 \quad \text{and} \quad L(x, 0) = L^* = 0.4, \quad (2.40)$$

in a single pipe $x \in [0, 1]$. Here,

$$K(x, t) = q(x, t) \quad \text{and} \quad L(x, t) = \left(c^2 \rho + \frac{q^2}{\rho} \right) (x, t) + R(x, t), \quad (2.41)$$

are the steady states and $R(x, t) = \int_0^x \mu \frac{q(\xi, t)}{\rho(\xi, t)} |q(\xi, t)| d\xi$.

To run the computations we divide the interval $\Omega = [0, 1]$ into N uniform grid cells and apply the well-balanced second-order CU scheme (2.35)–(2.37) to the system (2.39) with zero-order extrapolations for both K and L at the boundaries of the domain. We compute the solution until the final time $T = 1$ with $N = 100, 200, 400$ and 800 and report L^1 -errors, measured as $\|K(\cdot, T) - K^*\|_1$ and $\|L(\cdot, T) - L^*\|_1$, in Table 2.1. As one can see, on all of these grids, the initial data are preserved within the machine accuracy. For comparison, we run the same computations using the non-well-balanced CU scheme (2.1)–(2.3), in which case the initial equilibria are preserved within the accuracy of the scheme only, as can be seen in Table 2.2.

Table 2.2 Example 2.4: L^1 -errors and corresponding experimental convergence rates in the non-well-balanced computation of K and L at $T = 1$.

N	$\ K(\cdot, 1) - K^*\ _1$	rate	$\ L(\cdot, 1) - L^*\ _1$	rate
100	1.29E-06	-	8.81E-07	-
200	3.30E-07	1.96	2.25E-07	1.97
400	8.34E-08	1.98	5.69E-08	1.98
800	2.09E-08	1.99	1.43E-08	1.99

Next, we solve the system (2.39) with the perturbed initial data:

$$K(x, 0) = K^* + \eta e^{-100(x-0.5)^2} = 0.5 + \eta e^{-100(x-0.5)^2}, \quad L(x, 0) = L^* = 0.4, \quad (2.42)$$

with the perturbation constant $\eta > 0$. In Fig. 2.1, we plot the obtained momentum perturbations computed using both well-balanced and non-well-balanced schemes with two different perturbation constants, $\eta = 10^{-3}$ and $\eta = 10^{-6}$ at time $T = 0.2$ on $N = 100$ uniform grid cells. We also calculate a solution using the non-well-balanced method on finer grids, i.e., $N = 1600$ for $\eta = 10^{-3}$ and $N = 3200$ for $\eta = 10^{-6}$. We observe that for the larger value of the constant $\eta = 10^{-3}$, both the well-balanced and non-well-balanced schemes can capture the perturbation even on a coarse mesh. However, when the perturbation is relatively small, $\eta = 10^{-6}$, the well-balanced scheme still can resolve the perturbation on a coarse grid ($N = 100$), while the non-well-balanced method is not capable of catching it unless it is employed on a very fine mesh, say $N = 3200$.

Example 2.5—Gas dynamics with the bottom profile.

In the second example, we consider the 2×2 system of gas dynamics with bottom profile where the governing equations are given by:

$$\begin{cases} \rho_t + q_x = 0, \\ q_t + \left(c^2 \rho + \frac{q^2}{\rho} \right)_x = -g \rho h_x(x), \end{cases} \quad (2.43)$$

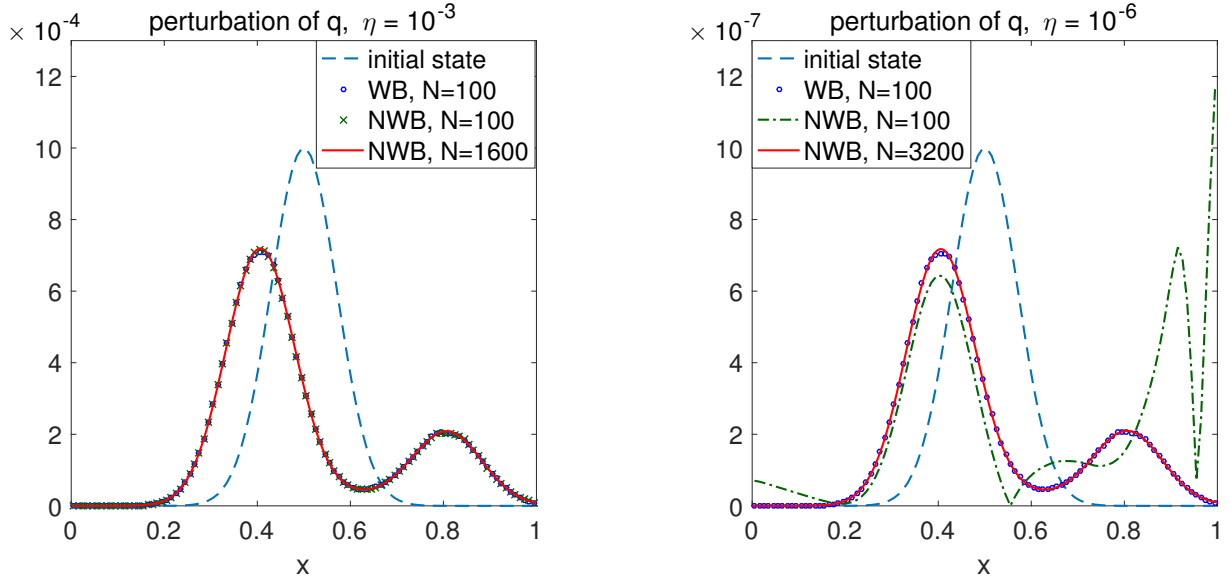


Figure 2.1 Example 2.4: Momentum perturbation computed by the well-balanced (WB) and non-well-balanced (NWB) schemes at time $T = 0.2$ for $\eta = 10^{-3}$ (left) and $\eta = 10^{-6}$ (right).

with $h(x)$ being the bottom profile. This case is relevant to the practical applications when gas pipes are not horizontal. In particular, the gravitational force needs to be considered in mountainous regions with high-pressure gas transmission.

Here, we consider the system (2.43) with $c = 1$, $g = 9.81$ and an exponential function

$$h(x) = e^{-(x-0.5)^2}. \quad (2.44)$$

We solve the system on the computational domain $x \in [0, 1]$ and subject to the following initial data (again given in terms of equilibrium variables):

$$K(x, 0) = q(x, 0) = K^* = 1 \quad \text{and} \quad L(x, 0) = L^* = 20, \quad (2.45)$$

where

$$K(x, t) = q(x, t) \quad \text{and} \quad L(x, t) = \left(c^2 \rho + \frac{q^2}{\rho} \right) (x, t) + R(x, t), \quad (2.46)$$

Table 2.3 Example 2.5: L^1 -errors and corresponding experimental convergence rates in the well-balanced computation of K and L at $T = 1$.

N	$\ K(\cdot, 1) - K^*\ _1$	$\ L(\cdot, 1) - L^*\ _1$
100	3.19E-16	1.17E-15
200	3.90E-16	9.76E-16
400	1.99E-16	8.70E-16
800	1.41E-16	9.45E-16

Table 2.4 Example 2.5: L^1 -errors and corresponding experimental convergence rates in the non-well-balanced computation of K and L at $T = 1$.

N	$\ K(\cdot, 1) - K^*\ _1$	rate	$\ L(\cdot, 1) - L^*\ _1$	rate
100	8.97E-03	-	0.117	-
200	2.25E-03	1.99	2.98E-02	1.97
400	5.64E-04	1.99	7.54E-03	1.98
800	1.41E-04	2.00	1.89E-03	1.99

and $R = \int_0^x g\rho(\xi, t)h_x(\xi)d\xi$. Since (2.45) is a steady state solution of (2.43), we adopt it to illustrate that the CU scheme (2.35)–(2.37) is well-balanced.

Similarly to the first example, we obtain the solutions of the system (2.43) by implementing both the well-balanced and non-well-balanced CU schemes on a uniform grid with $N = 100, 200, 400$ and 800 cells. Tables 2.3 and 2.4 indicate the L^1 -errors as estimated in the previous example in measuring the equilibrium states K and L computed by both the well-balanced and non-well-balanced schemes. One can clearly see that while the well-balanced scheme gives errors within machine accuracy, the non-well-balanced method requires very fine grid, to preserve steady state solution.

We, then, introduce an initial perturbation on momentum as follows:

$$K(x, 0) = K^* + \eta e^{-100(x-0.5)^2} = 1 + \eta e^{-100(x-0.5)^2}, \quad L(x, 0) = L^* = 20, \quad (2.47)$$

where $\eta > 0$ is the perturbation constant. We first run the computations with $\eta = 10^{-1}$ and plot the results in Fig. 2.2 (left) obtained at time $T = 0.25$ by both the well-balanced and non-well-balanced methods with $N = 100$ uniform grid cells. In both cases, zero-order extrapolations are implemented at the boundaries of the computational interval $\Omega = [0, 1]$. For comparison, we also plot a solution obtained by the non-well-balanced scheme with $N = 1600$. We observe that, while the well-balanced scheme is capable of resolving the perturbation on a coarse mesh, the non-well-balanced method requires a finer mesh, e.g., $N = 1600$. In Fig. 2.2 (right), we illustrate the momentum perturbation at time $T = 0.25$

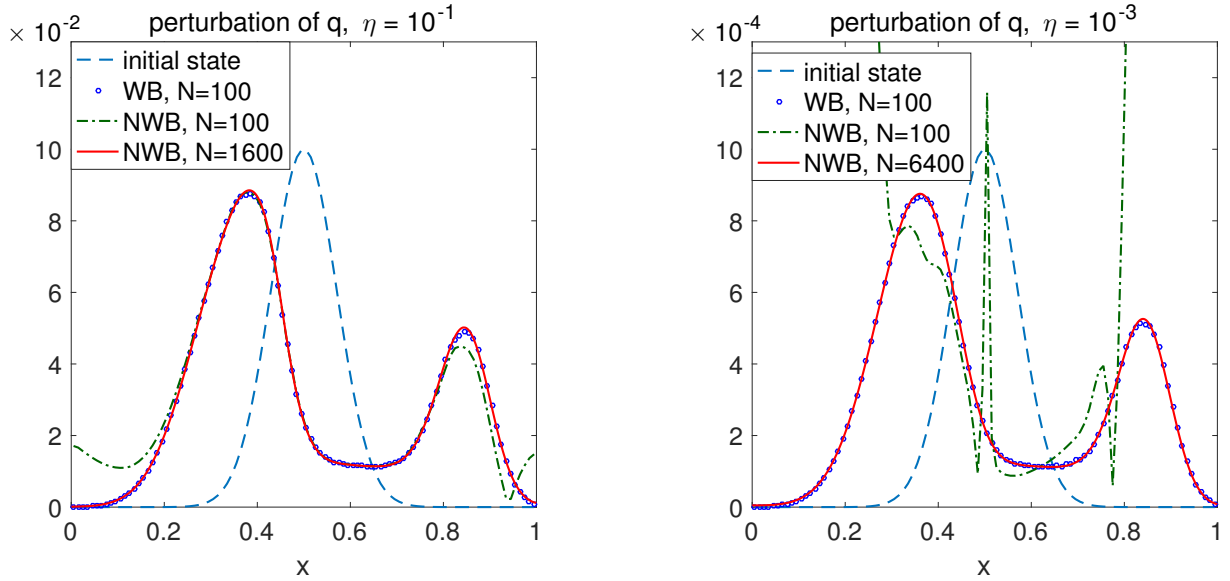


Figure 2.2 Example 2.5: Momentum perturbations computed by the well-balanced (WB) and non-well-balanced (NWB) schemes for $\eta = 10^{-1}$ (left) and $\eta = 10^{-3}$ (right) at time $T = 0.25$.

obtained by both the well-balanced and non-well-balanced schemes for a smaller value of the perturbation constant $\eta = 10^{-3}$. We note that our well-balanced scheme can capture smaller perturbations of the steady states on a coarse mesh, $N = 100$, while to obtain corresponding results with the non-well-balanced method, one needs to use a very refined mesh, $N = 6400$, which would be costly in most of the cases.

Example 2.6—Traffic flow with relaxation to equilibrium velocities.

In the last example, we study a second-order model for traffic flow, which has been introduced in [6] to model driver dependent traffic conditions. The model has been investigated since then by many authors and we refer to [46] for a recent comparison and discussion.

The governing equations are written in terms of the density of cars $\rho(x, t)$ and the velocity $u(x, t)$, as well as a driver property $w(x, t)$. The latter can be viewed as distance towards an equilibrium velocity $V_{eq}(\rho)$. For simplicity, we chose as $V_{eq}(\rho) = 1 - \rho$, where $\rho = 1$ represents maximum density and introduce a fixed relaxation time $\tau > 0$ for all drivers, in which case the model reads:

$$\begin{cases} \rho_t + (\rho u)_x = 0, \\ (\rho w)_t + (\rho u w)_x = \frac{\rho}{\tau} ((1 - \rho) - u), \\ w = u + \rho. \end{cases}$$

We substitute $u = w - \rho$, introduce a new variable $q = \rho u = \rho(w - 1)$ and rewrite the above system in the conservative form:

$$\begin{cases} \rho_t + (q + \rho(1 - \rho))_x = 0, \\ q_t + \left(\frac{q^2}{\rho} + q(1 - \rho) \right)_x = -\frac{1}{\tau} q. \end{cases} \quad (2.48)$$

We observe that in the limit of small relaxation times ($\tau \rightarrow 0$), the second equation in (2.48) formally ensures $q \rightarrow 0$ and $\rho \in [0, 1]$, and the model predictions of (2.48) are expected to be close to those of the classical Lighthill–Whitham–Richards (LWR) model [116] given by $\rho_t + (\rho(1 - \rho))_x = 0$.

Clearly, $q = 0$ is a steady state solution of the system (2.48) for any constant ρ . However, for fixed positive τ , the system has steady states deviating from the LWR model. In view of the previous discussion we introduce the equilibrium variables K and L as

$$K = q + \rho(1 - \rho), \quad L = \frac{q^2}{\rho} + q(1 - \rho) + R, \quad (2.49)$$

Table 2.5 Example 2.6: L^1 -errors and corresponding experimental convergence rates in the well-balanced computation of K and L at $T = 1$.

N	$\ K(\cdot, 1) - K^*\ _1$	$\ L(\cdot, 1) - L^*\ _1$
100	4.21E-17	1.00E-16
200	5.57E-17	8.74E-17
400	1.48E-15	2.46E-15
800	5.50E-17	1.17E-16

where $R(x, t) = \int_0^x \frac{1}{\tau} q(\xi, t) d\xi$. Then, the steady states are $K, L = \text{Const}$.

We consider the system (2.48) with $\tau = 1$ and set the following initial data given with respect to the equilibrium variables:

$$K(x, 0) = K^* = 0.375, \quad L(x, 0) = L^* = 0.5, \quad (2.50)$$

which also satisfy the steady state solutions of (2.48).

As before, we first verify that the developed well-balanced CU scheme (2.35)–(2.37) is capable of preserving steady states of the system (2.48) exactly. To this end, we partition the computational domain $\Omega = [0, 1]$ into N uniform cells and assign zero-order extrapolations for K and L at the boundaries. We obtain the results at final time $T = 1$ by implementing the well-balanced CU scheme with $N = 100, 200, 400$ and 800 grid cells. In Table 2.5, we present the L^1 -errors computed as before, for equilibrium variables K and L , that is, $\|K(\cdot, T) - K^*\|_1$ and $\|L(\cdot, T) - L^*\|_1$, and observe the errors of machine accuracy for the well-balanced scheme. However, we can conclude that non-well-balanced scheme can maintain the steady states only within the order of the scheme, as seen in Table 2.6. We then investigate the performance of the well-balanced scheme by capturing the perturbations of the steady states. Here, we add a small perturbation to the initial value of the variable q :

$$q^p(x, 0) = q(x, 0) + \eta e^{-50(x-0.5)^2}, \quad (2.51)$$

where $\eta = 10^{-7}$ is taken in this example. In Fig. 2.3, we plot the perturbations on the

Table 2.6 Example 2.6: L^1 -errors and corresponding experimental convergence rates in the non-well-balanced computation of K and L at $T = 1$.

N	$\ K(\cdot, 1) - K^*\ _1$	rate	$\ L(\cdot, 1) - L^*\ _1$	rate
100	2.59E-06	-	8.10E-06	-
200	6.47E-07	2.00	2.02E-06	2.00
400	1.61E-07	2.01	5.04E-07	2.00
800	4.04E-08	1.99	1.25E-07	2.01

equilibrium variables K and L , respectively, obtained by both well-balanced and non-well-balanced schemes with $N = 100$ and 200 uniform grid cells at time $T = 0.1$. For observation, we also plot the solutions computed by non-well-balanced method on a very fine mesh with $N = 6400$. We conclude that while the well-balanced scheme is capable of capturing the perturbations on a relatively coarse grid, the non-well-balanced scheme needs to be implemented on a much finer grid.

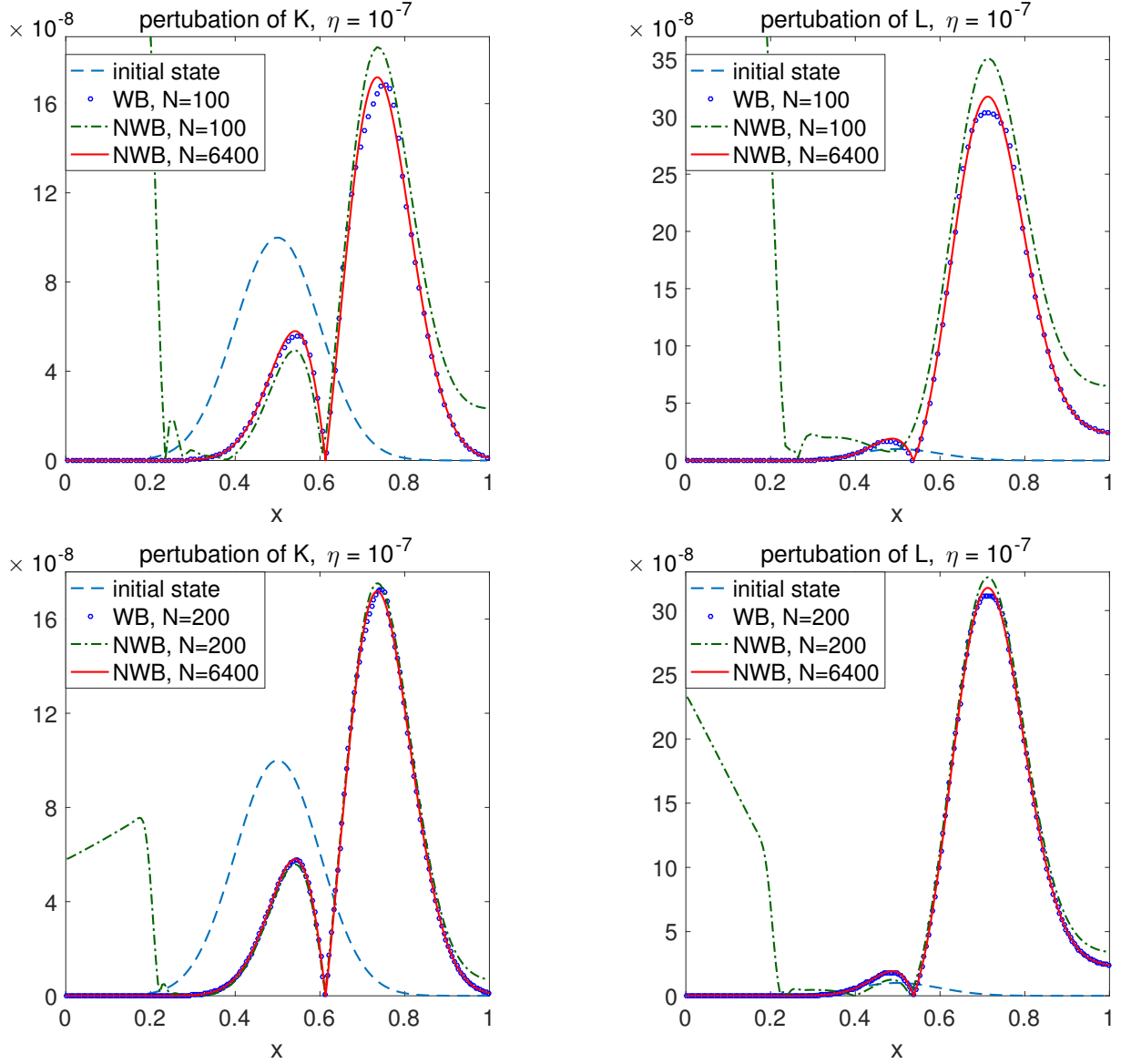


Figure 2.3 Example 2.6: Perturbations on the equilibrium variable K (left column) and L (right column), computed by the well-balanced (WB) and non-well-balanced (NWB) schemes at time $T = 0.1$ for $\eta = 10^{-7}$.

2.3 The One-Dimensional Euler Equations of Gas Dynamics With Gravitation

In this section, we consider the one-dimensional (1-D) Euler equations of gas dynamics with gravitation in the y -direction:

$$\mathbf{q}_t + \mathbf{G}(\mathbf{q})_y = \mathbf{S}(\mathbf{q}), \quad (2.52)$$

where

$$\mathbf{q} := \begin{pmatrix} \rho \\ \rho v \\ E \end{pmatrix}, \quad \mathbf{G}(\mathbf{q}) := \begin{pmatrix} \rho v \\ \rho v^2 + p \\ v(E + p) \end{pmatrix} \quad \text{and} \quad \mathbf{S}(\mathbf{q}) := \begin{pmatrix} 0 \\ -\rho \phi_y \\ -\rho v \phi_y \end{pmatrix} \quad (2.53)$$

are the vectors of the conservative variables, flux and gravitational source term, respectively, and the corresponding equation of state is

$$E = \frac{p}{\gamma - 1} + \frac{\rho v^2}{2}. \quad (2.54)$$

Here, ρ is the density, v is the y -velocity, E is the total energy, p is the pressure and ϕ is the time-independent gravitational potential.

Once again, the aim is to construct a well-balanced numerical method which is capable of exactly capturing steady state solutions, which can be derived as follows. We consider the system (2.52)-(2.54) and obtain its steady state solutions from the time-independent system $\mathbf{G}(\mathbf{q})_y = \mathbf{S}(\mathbf{q})$. To this end, we first incorporate the source term $-\rho \phi_y$ into the flux and rewrite the system as follows:

$$\begin{cases} \rho_t + (\rho v)_y = 0, \\ (\rho v)_t + (\rho v^2 + L)_y = 0, \\ E_t + (v(E + p))_y = -\rho v \phi_y, \end{cases} \quad (2.55)$$

which can be put into the vector form (2.52) with different flux and source terms:

$$G(q) := \begin{pmatrix} \rho v \\ \rho v^2 + L \\ v(E + p) \end{pmatrix}, \quad S(q) := \begin{pmatrix} 0 \\ 0 \\ -\rho v \phi_y \end{pmatrix}, \quad (2.56)$$

where L is a global variable given by

$$L := p + R, \quad R(y, t) := \int_y^y \rho(\eta, t) \phi_y(\eta) d\eta. \quad (2.57)$$

It then immediately follows that the simplest steady state of (2.55) is the motionless one, for which

$$v \equiv 0 \quad \text{and} \quad L \equiv \text{Const.} \quad (2.58)$$

As before, we observe that the semi-discrete CU scheme (2.2)–(2.9) illustrated in Section 2.1 is not capable of exactly preserving the steady-state solutions of (2.52). Indeed, substituting $v \equiv 0$ into (2.2)–(2.3) and noting that for all k , $b_{k+\frac{1}{2}}^+ = -b_{k+\frac{1}{2}}^-$ (since $v_k^N = v_{k+1}^S = 0$), we obtain the ODE system

$$\begin{cases} \frac{d\bar{\rho}_k}{dt} = -\frac{\beta_{k+\frac{1}{2}}(\rho_{k+1}^S - \rho_k^N - \delta\rho_{k+\frac{1}{2}}) - \beta_{k-\frac{1}{2}}(\rho_k^S - \rho_{k-1}^N - \delta\rho_{k-\frac{1}{2}})}{\Delta y}, \\ \frac{d(\bar{\rho}v)_k}{dt} = -\frac{(p_{k+1}^S + p_k^N) - (p_k^S + p_{k-1}^N)}{2\Delta y} - \bar{\rho}_k(\phi_y)_k, \\ \frac{d\bar{E}_k}{dt} = -\frac{\beta_{k+\frac{1}{2}}(E_{k+1}^S - E_k^N - \delta E_{k+\frac{1}{2}}) - \beta_{k-\frac{1}{2}}(E_k^S - E_{k-1}^N - \delta E_{k-\frac{1}{2}})}{\Delta y}, \end{cases} \quad (2.59)$$

whose right-hand side (RHS) does not necessarily vanish and hence the steady state would not be preserved at the discrete level. We would like to stress that even for the first-order version of the CU scheme (2.2)–(2.9), that is, when $(q_y)_k \equiv 0$ in (2.7), (2.8), the RHS of (2.59) does not vanish. This means that the lack of balance between the numerical flux and source terms is a fundamental problem of the scheme. We also note that for smooth solutions, the balance error in (2.59) is expected to be of order $(\Delta y)^2$, but a coarse grid solution may contain large spurious waves as demonstrated in the numerical experiments presented in Section 2.3.2. We, then, in Section 2.3.1, derive a well-balanced modification

of the described CU scheme.

2.3.1 Well-Balanced Central-Upwind Scheme

In this section, we present a well-balanced modification of the CU scheme from Section 2.1. The new scheme will be developed by first introducing a well-balanced reconstruction performed on the equilibrium variables, $(\rho, \rho v, L)$, rather than the conservative ones, $(\rho, \rho v, E)$, see, e.g., [27, 29], and then applying a slightly modified CU scheme to the system (2.55)- (2.57).

2.3.1.1 Well-Balanced Reconstruction

We now point out a special reconstruction, which is used in the derivation of a well-balanced CU scheme. The main idea is to reconstruct equilibrium variable L rather than E . For the first two components we still use formula (2.7) to obtain the same piecewise linear reconstructions as before, $\tilde{\rho}(y)$ and $(\tilde{\rho}v)(y)$, and compute the corresponding point values of $\rho^{N,S}$ and $(\rho v)^{N,S}$, and then obtain $v^{N,S} = (\rho v)^{N,S} / \rho^{N,S}$.

To reconstruct L , we first compute the point values of R at the cell interfaces and the cell centers, recursively, by using the midpoint rule:

$$R_{k_L - \frac{1}{2}} = 0, \quad \begin{cases} R_{k+\frac{1}{2}} = R_{k-\frac{1}{2}} + \Delta y \bar{\rho}_k (\phi_y)_k, \\ R_k = \frac{1}{2} (R_{k-\frac{1}{2}} + R_{k+\frac{1}{2}}), \end{cases} \quad k = k_L, \dots, k_R,$$

and thus the values of L at the cell centers are

$$L_k = p_k + R_k, \tag{2.60}$$

where $p_k = (\gamma - 1) \left(\bar{E}_k - \frac{\bar{\rho}_k}{2} v_k^2 \right)$ is obtained from the corresponding EOS (2.54) and $v_k = (\bar{\rho}v)_k / \bar{\rho}_k$. Equipped with (2.60), we then apply the minmod reconstruction procedure to $\{L_k\}$ and obtain the point values of L at the cell interfaces:

$$L_k^N = L_k + \frac{\Delta y}{2} (L_y)_k, \quad L_{k+1}^S = L_{k+1} - \frac{\Delta y}{2} (L_y)_{k+1},$$

where

$$(L_y)_k = \min\left(\theta \frac{L_{k+1} - L_k}{\Delta y}, \frac{L_{k+1} - L_{k-1}}{2\Delta y}, \theta \frac{L_k - L_{k-1}}{\Delta y}\right).$$

Finally, the point values of p and E needed for computation of numerical fluxes are

$$p_k^N = L_k^N - R_{k+\frac{1}{2}}, \quad p_k^S = L_k^S - R_{k-\frac{1}{2}}$$

and

$$E_k^N = \frac{p_k^N}{\gamma - 1} + \frac{((\rho v)_k^N)^2}{2\rho_k^N}, \quad E_k^S = \frac{p_k^S}{\gamma - 1} + \frac{((\rho v)_k^S)^2}{2\rho_k^S},$$

respectively.

Remark 2.3.1 If the gravitational potential is linear (e.g. $\phi(y) = g y$ with g being the gravitational constant), then R can be computed by using the piecewise linear reconstruction of ρ , (2.7), which results in the piecewise quadratic approximation of R :

$$\tilde{R}(y) = g \int_{y_{k_L-\frac{1}{2}}}^y \tilde{\rho}(\xi) d\xi = g \sum_k \left[\Delta y \sum_{i=k_L}^{k-1} \bar{\rho}_i + \bar{\rho}_k (y - y_{k-\frac{1}{2}}) + \frac{(\rho_y)_k}{2} (y - y_{k-\frac{1}{2}})(y - y_{k+\frac{1}{2}}) \right] \cdot \chi_{C_k}(y).$$

Then, the point values of R at the cell interfaces and cell centers are

$$R_{k+\frac{1}{2}} = g \Delta y \sum_{i=k_L}^k \bar{\rho}_i \quad \text{and} \quad R_k = g \Delta y \sum_{i=k_L}^{k-1} \bar{\rho}_i + \frac{g \Delta y}{2} \bar{\rho}_k - \frac{g (\Delta y)^2}{8} (\rho_y)_k,$$

respectively.

2.3.1.2 Well-Balanced Evolution

The cell-averages of \bar{q} are evolved in time according to the system of ODEs (2.2). The second and third components of the numerical fluxes \mathcal{G} are computed the same way as in (2.3), but with G given by (2.56), that is,

$$\begin{aligned}
\mathcal{G}_{k+\frac{1}{2}}^{(2)} &= \frac{b_{k+\frac{1}{2}}^+ (\rho_k^N (v_k^N)^2 + L_k^N) - b_{k+\frac{1}{2}}^- (\rho_{k+1}^S (v_{k+1}^S)^2 + L_{k+1}^S)}{b_{k+\frac{1}{2}}^+ - b_{k+\frac{1}{2}}^-} \\
&\quad + \beta_{k+\frac{1}{2}} ((\rho v)_{k+1}^S - (\rho v)_k^N - \delta(\rho v)_{k+\frac{1}{2}}), \quad (2.61) \\
\mathcal{G}_{k+\frac{1}{2}}^{(3)} &= \frac{b_{k+\frac{1}{2}}^+ v_k^N (E_k^N + p_k^N) - b_{k+\frac{1}{2}}^- v_{k+1}^S (E_{k+1}^S + p_{k+1}^S)}{b_{k+\frac{1}{2}}^+ - b_{k+\frac{1}{2}}^-} + \beta_{k+\frac{1}{2}} (E_{k+1}^S - E_k^N - \delta \rho_{k+\frac{1}{2}}),
\end{aligned}$$

while the first component is modified in order to exactly preserve the steady state (2.58):

$$\begin{aligned}
\mathcal{G}_{k+\frac{1}{2}}^{(1)} &= \frac{b_{k+\frac{1}{2}}^+ (\rho v)_k^N - b_{k+\frac{1}{2}}^- (\rho v)_{k+1}^S}{b_{k+\frac{1}{2}}^+ - b_{k+\frac{1}{2}}^-} \\
&\quad + \beta_{k+\frac{1}{2}} H \left(\frac{|L_{k+1} - L_k|}{\Delta y} \cdot \frac{y_{k_R+\frac{1}{2}} - y_{k_L-\frac{1}{2}}}{\max\{L_k, L_{k+1}\}} \right) \cdot (\rho_{k+1}^S - \rho_k^N - \delta \rho_{k+\frac{1}{2}}). \quad (2.62)
\end{aligned}$$

Notice that the last term in (2.62) is now multiplied by a smooth function H , designed to be very small when the computed solution is locally (almost) at steady state, that is, at the cell interfaces where $\frac{|L_{k+1} - L_k|}{\Delta y} \sim 0$, and to be very close to 1 elsewhere. This is done in order to guarantee the well-balanced property of the scheme as we show in Theorem 2.3.1 proved in Section 2.3.1.3. On the other hand, the modification of the original CU flux is quite minor since $H(\psi)$ is very close to 1 unless ψ is very small.

A sketch of a typical function H is shown in Figure 2.4. In all of our numerical experiments, we have used

$$H(\psi) = \frac{(C\psi)^m}{1 + (C\psi)^m}, \quad (2.63)$$

with $C = 200$ and $m = 6$. To reduce the dependence of the computed solution on the choice of particular values of C and m , the argument of H in (2.62) is normalized by a factor $\frac{y_{k_R+\frac{1}{2}} - y_{k_L-\frac{1}{2}}}{\max\{L_k, L_{k+1}\}}$, which makes $H(\psi)$ dimensionless.

The one-sided local speeds of propagation, $b_{k+\frac{1}{2}}^\pm$, are estimated using the smallest and largest eigenvalues of the Jacobian $\frac{\partial G}{\partial q}$:

$$b_{k+\frac{1}{2}}^+ = \max(v_k^N + c_k^N, v_{k+1}^S + c_{k+1}^S, 0), \quad b_{k+\frac{1}{2}}^- = \min(v_k^N - c_k^N, v_{k+1}^S - c_{k+1}^S, 0), \quad (2.64)$$

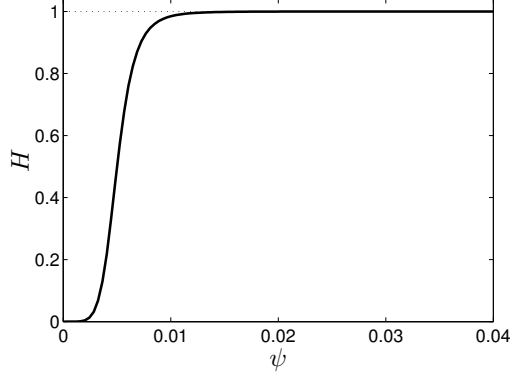


Figure 2.4 Sketch of $H(\psi)$, (2.63).

where the velocities, v_k^N and v_{k+1}^S , are obtained using the identity $v \equiv (\rho v)/\rho$, c_k^N and c_{k+1}^S are the speeds of sound defined by $c^2 = \gamma p/\rho$, and the pressures, p_k^N and p_{k+1}^S , are obtained using the EOS (2.54).

Finally, the cell averages of the source term are approximated using the midpoint quadrature rule as follows:

$$\bar{\mathcal{S}}_k = (0, 0, -(\overline{\rho v})_k(\phi_y)_k)^T. \quad (2.65)$$

2.3.1.3 Proof of the Well-Balanced Property

Theorem 2.3.1 *The semi-discrete CU scheme (2.2), (2.61)–(2.65) coupled with the reconstruction described in Section 2.3.1.1 is well-balanced in the sense that it exactly preserves the steady state (2.58).*

Proof: Assume that at certain time level, we have

$$v_k^N \equiv v_k \equiv v_k^S \equiv 0 \quad \text{and} \quad L_k^N \equiv L_k \equiv L_k^S \equiv \widehat{L}, \quad (2.66)$$

where \widehat{L} is a constant. To show that the proposed scheme is well-balanced, we need to show that the RHS of (2.2) is identically equal to zero for the data in (2.66). Since the source term (2.65) vanishes for $v_k = 0$, it is enough to prove that the numerical fluxes are constant for all k for the data in (2.66).

Indeed, the first component (2.62) of the numerical flux vanishes since $v_k^N = v_{k+1}^S = 0$ and $L_k = L_{k+1} = \widehat{L}$ (the latter implies $H\left(\frac{|L_{k+1}-L_k|}{\Delta y} \cdot \frac{y_{k_R+\frac{1}{2}}-y_{k_L-\frac{1}{2}}}{\max\{L_k, L_{k+1}\}}\right) = H(0) = 0$). The second component in (2.61) of the numerical flux is constant and equal to \widehat{L} since $v_k^N = v_{k+1}^S = 0$ and $L_k^N = L_{k+1}^S = \widehat{L}$. Finally, the third component in (2.61) of the numerical flux also vanishes:

$$\begin{aligned}\mathcal{G}_{k+\frac{1}{2}}^{(3)} &= \beta_{k+\frac{1}{2}} (E_{k+1}^S - E_k^N - \delta E_{k+\frac{1}{2}}) = \frac{\beta_{k+\frac{1}{2}}}{\gamma-1} \cdot \frac{p_{k+1}^S - p_k^N}{2} \\ &= \frac{\beta_{k+\frac{1}{2}}}{2(\gamma-1)} [(L_{k+1}^S - R_{k+\frac{1}{2}}) - (L_k^N - R_{k+\frac{1}{2}})] = 0,\end{aligned}$$

since $L_k^N = L_{k+1}^S = \widehat{L}$ and $\delta E_{k+\frac{1}{2}} = \frac{1}{2}(E_{k+1}^S - E_k^N)$. ■

2.3.2 Numerical Examples

In this section, we present a number of 1-D numerical examples, in which we demonstrate the performance of the proposed well-balanced semi-discrete CU scheme.

In all of the examples below, we have used the three-stage third-order strong stability preserving Runge-Kutta method (see, e.g., [58, 60, 144]) to solve the ODE systems (2.2) and (2.79). The CFL number in (2.10) has been set to $\kappa = 0.4$. Also, we have used the following constant values: the minmod parameter $\theta = 1.3$ and the specific heat ratio $\gamma = 1.4$.

In all of the 1-D numerical experiments, we use a uniform mesh with the total number of grid cells $N = k_R - k_L + 1$.

Example 2.1—Shock tube problem.

The first example is a modification of the Sod shock tube problem taken from [121, 154]. We solve the system (2.52)–(2.54) with $\phi_y \equiv 1$ in the computational domain $[0, 1]$ using the following initial data:

$$(\rho(y, 0), v(y, 0), p(y, 0)) = \begin{cases} (1, 0, 1), & \text{if } y \leq 0.5, \\ (0.125, 0, 0.1), & \text{if } y > 0.5, \end{cases}$$

and reflecting boundary conditions at both ends of the computational domain. These boundary conditions are implemented using the ghost cell technique as follows:

$$\begin{aligned}\bar{\rho}_{k_L-1} &:= \bar{\rho}_{k_L}, & v_{k_L-1} &:= -v_{k_L}, & L_{k_L-1} &:= L_{k_L}, \\ \bar{\rho}_{k_R+1} &:= \bar{\rho}_{k_R}, & v_{k_R+1} &:= -v_{k_R}, & L_{k_R+1} &:= L_{k_R}.\end{aligned}$$

We compute the solution using $N = 100$ uniformly placed grid cells and compare it with the reference solution obtained using $N = 2000$ uniform cells. In Figure 2.5, we plot both the coarse and fine grid solutions at time $T = 0.2$. As one can see, the proposed CU scheme captures the solutions on coarse mesh quite well showing a good agreement with both the reference solution and the results obtained in [121, 154].

Example 2.2—Isothermal equilibrium solution.

In the second example, taken from [154] (see also [110, 121, 149]), we test the ability of the proposed CU scheme to accurately capture small perturbations of the steady state

$$\rho(y) = e^{-\phi(y)}, \quad v(y) \equiv 0, \quad p(y) = e^{-\phi(y)}, \quad (2.67)$$

which satisfies (2.58) for the system (2.52)–(2.54) with the linear gravitational potential $\phi(y) = y$.

We take the computational domain $[0, 1]$ and use a zero-order extrapolation at the boundaries:

$$\begin{aligned}\bar{\rho}_{k_L-1} &:= \bar{\rho}_{k_L} e^{\Delta y (\phi_y)_{k_L}}, & v_{k_L-1} &:= v_{k_L}, & L_{k_L-1} &:= L_{k_L}, \\ \bar{\rho}_{k_R+1} &:= \bar{\rho}_{k_R} e^{-\Delta y (\phi_y)_{k_R}}, & v_{k_R+1} &:= v_{k_R}, & L_{k_R+1} &:= L_{k_R}.\end{aligned}$$

Note that the boundary conditions on L can be recast in terms of p and ρ as

$$p_{k_L-1} = p_{k_L} + \Delta y \bar{\rho}_{k_L} (\phi_y)_{k_L}, \quad p_{k_R+1} = p_{k_R} - \Delta y \bar{\rho}_{k_R} (\phi_y)_{k_R}.$$

We first numerically verify the proposed CU scheme capable of exactly preserving the steady state (2.67). We use several uniform grids and observe that the initial conditions are preserved within the machine accuracy.

Next, we introduce a small initial pressure perturbation and consider the system (2.52)–

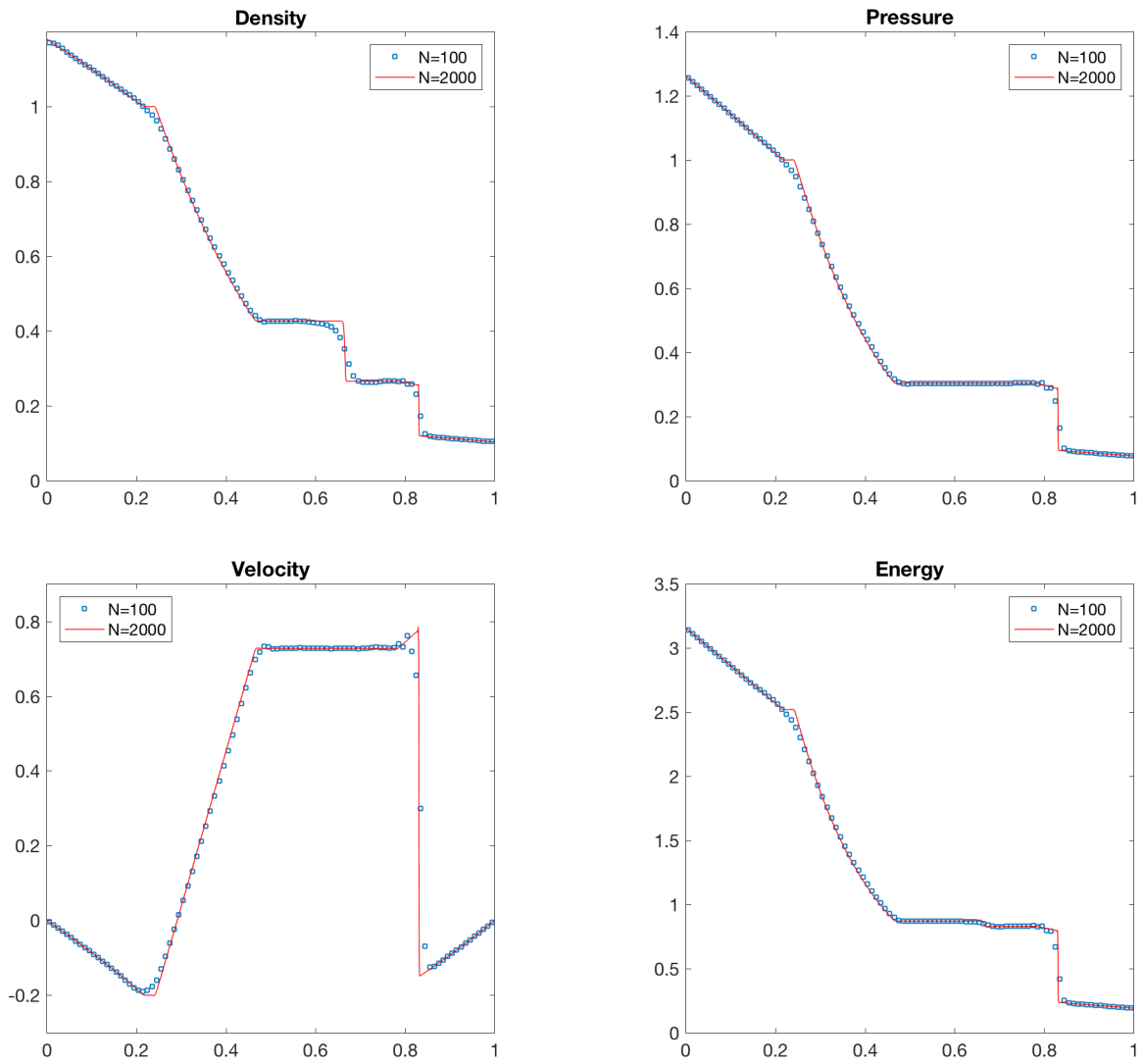


Figure 2.5 Example 2.1: Solutions computed by the well-balanced CU scheme using $N = 100$ and 2000 cells.

(2.54) subject to the following initial data:

$$\rho(y, 0) = e^{-y}, \quad v(y, 0) \equiv 0, \quad p(y, 0) = e^{-y} + \eta e^{-100(y-0.5)^2},$$

where η is a small positive number. In the numerical experiments, we use larger ($\eta = 10^{-2}$) and smaller ($\eta = 10^{-4}$) perturbations.

We first apply the proposed well-balanced CU scheme to this problem and compute the solution at time $T = 0.25$. The obtained pressure perturbation ($p(y, 0.25) - e^{-y}$) computed using $N = 200$ and 2000 (reference solution) uniform grid cells are plotted in Figure 2.6 for both $\eta = 10^{-2}$ and 10^{-4} . As one can see, the scheme accurately captures both small and large perturbations on a relatively coarse mesh with $N = 200$. In order to demonstrate the importance of the well-balanced property, we apply the non-well-balanced CU scheme described in Section 2.1 to the same initial-boundary value problem (IBVP). The obtained results are shown in Figure 2.6 as well. It should be observed that while the larger perturbation is quite accurately computed by both schemes, the non-well-balanced CU scheme fails to capture the smaller one.

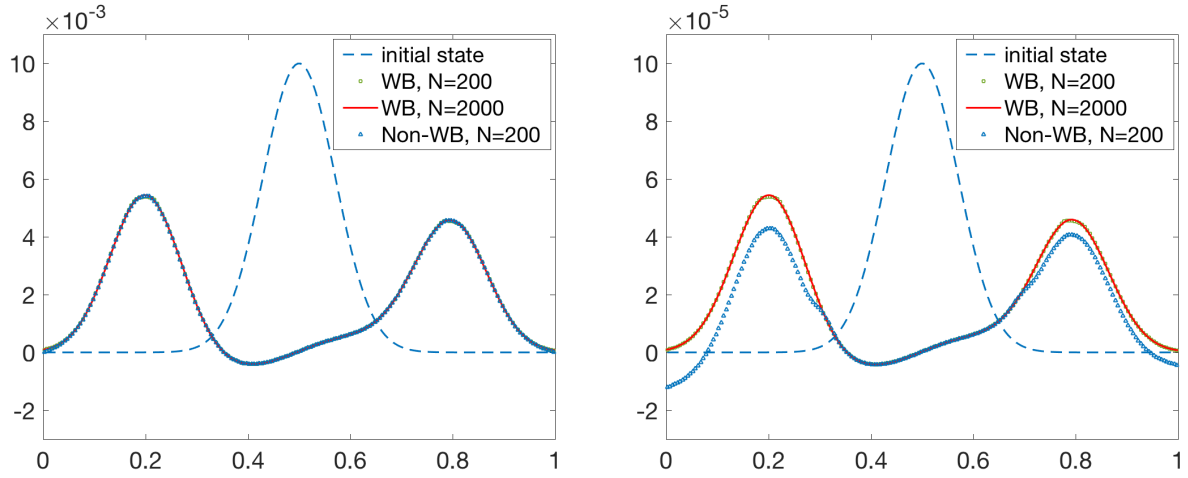


Figure 2.6 Example 2.2: Pressure perturbation ($p(y, 0.25) - e^{-y}$) computed by the well-balanced (WB) and non-well-balanced (Non-WB) CU schemes with $N = 200$ and 2000 for $\eta = 10^{-2}$ (left) and $\eta = 10^{-4}$ (right).

Example 2.3—Nonlinear gravitational potential.

In this example, we consider the system (2.52)–(2.54) with the nonlinear gravitational potentials $\phi(y) = \frac{1}{2}y^2$ and $\phi(y) = \sin(2\pi y)$ subject to the steady-state initial data

$$\rho(y, 0) = e^{-\phi(y)}, \quad v(y, 0) \equiv 0, \quad p(y, 0) = e^{-\phi(y)}, \quad (2.68)$$

with the same boundary conditions as in Example 2.2. We first apply both the well-balanced and non-well-balanced CU schemes to this IBVP and compute the solution on a sequence of different meshes until the final time $T = 1$. We observe that while the well-balanced scheme preserves the steady state (2.68) within the machine accuracy, the errors in the non-well-balanced computations are of the second order of accuracy as shown in Tables 2.7 and 2.8.

Table 2.7 Example 2.3: L^1 -errors and corresponding experimental convergence rates in the non-well-balanced computation of ρ , ρv and E ; $\phi(y) = \frac{1}{2}y^2$.

N	$\ \rho(\cdot, 1) - \rho(\cdot, 0)\ _1$	rate	$\ (\rho v)(\cdot, 1) - (\rho v)(\cdot, 0)\ _1$	rate	$\ E(\cdot, 1) - E(\cdot, 0)\ _1$	rate
100	8.11E-06	–	9.02E-06	–	2.47E-05	–
200	1.94E-06	2.06	2.36E-06	1.93	5.96E-06	2.05
400	4.70E-07	2.04	6.04E-07	1.96	1.46E-06	2.02
800	1.15E-07	2.03	1.53E-07	1.98	3.62E-07	2.01

Table 2.8 Example 2.3: L^1 -errors and corresponding experimental convergence rates in the non-well-balanced computation of ρ , ρv and E ; $\phi(y) = \sin(2\pi y)$.

N	$\ \rho(\cdot, 1) - \rho(\cdot, 0)\ _1$	rate	$\ (\rho v)(\cdot, 1) - (\rho v)(\cdot, 0)\ _1$	rate	$\ E(\cdot, 1) - E(\cdot, 0)\ _1$	rate
100	1.38E-03	–	1.01E-03	–	4.91E-03	–
200	3.38E-04	2.03	2.58E-04	1.97	1.19E-03	2.04
400	8.30E-05	2.01	6.51E-05	1.98	2.93E-04	2.02
800	2.03E-05	2.03	1.63E-05	1.99	7.27E-05	2.01

We, next, consider the same IBVP but with the following perturbed initial data:

$$\rho(y, 0) = e^{-\phi(y)}, \quad v(y, 0) \equiv 0, \quad p(y, 0) = e^{-\phi(y)} + \eta e^{-100(y-0.5)^2}.$$

We take $\eta = 10^{-3}$ and $\eta = 10^{-5}$, then compute the solution until the final time $T = 0.25$ using both the well-balanced and non-well-balanced CU schemes. In Figures 2.7 and 2.8, we plot the pressure perturbations $(p(y, 0.25) - e^{-\phi(y)})$ computed using $N = 200$ and $N = 2000$ (reference solution) uniform grid cells for $\phi(y) = \frac{1}{2}y^2$ and $\phi(y) = \sin(2\pi y)$, respectively. For comparison, we plot the same perturbations computed by applying non-well-balanced CU scheme with $N = 200$ uniform grid points. In Figures 2.7-2.8, we also include the results obtained by non-well-balanced CU scheme with finer mesh sizes. One can conclude that, while both well-balanced and non-well-balanced schemes can capture the larger perturbation, e.g. $\eta = 10^{-4}$, on a coarse grid; the latter one is not able to preserve this property for smaller perturbation constant. As η gets smaller, very fine mesh size is required to control the perturbation with the non-well-balanced method.

In Figure 2.8, we demonstrate the pressure perturbation $(p(y, 0.25) - e^{-\sin(2\pi y)})$ obtained by using well-balanced and non-well-balanced CU schemes on $N = 200$ uniform grid cells for $\eta = 10^{-3}$. Similarly with the previous discussion, the proposed well-balanced CU scheme resolves the perturbation precisely on coarser grids, while the non-well-balanced scheme requires finer grid size, e.g. $N = 2000$ to capture the perturbation as accurate as the well-balanced method does.

Then, similarly, we apply a perturbation to the steady state and present that it is resolved by the well-balanced scheme for each perturbation on a coarse grid. However, the non-well-balanced one fails to capture the smaller perturbations.

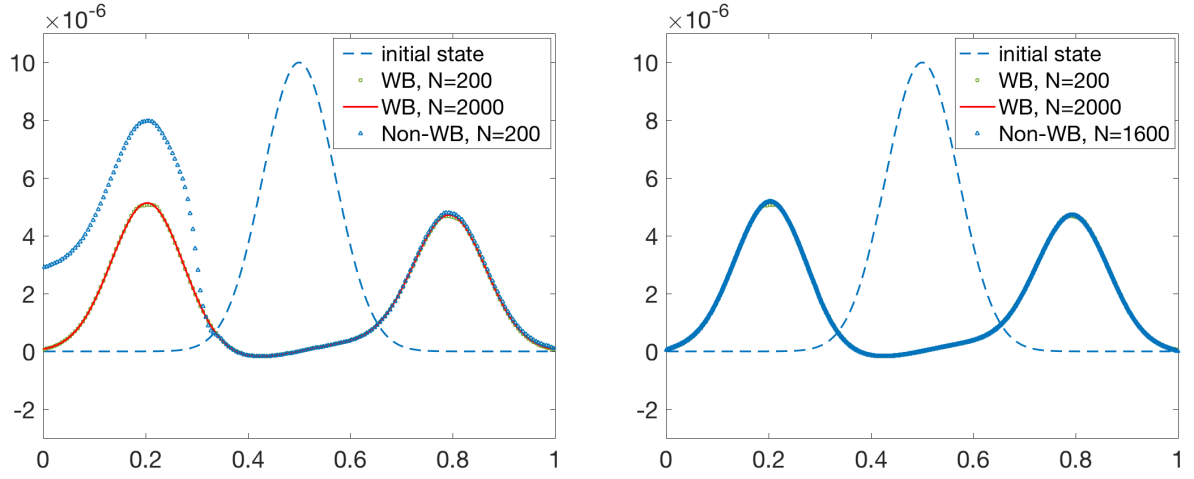


Figure 2.7 Example 2.3: Pressure perturbation $(p(y, 0.25) - e^{-y^2/2})$ computed by the well-balanced (WB) and non-well-balanced (Non-WB) CU schemes for $\eta = 10^{-5}$ with $N = 200$ for each scheme (left) and $N = 1600$ for the non-well-balanced scheme (right). The reference solution is computed with $N = 2000$ grid pints.

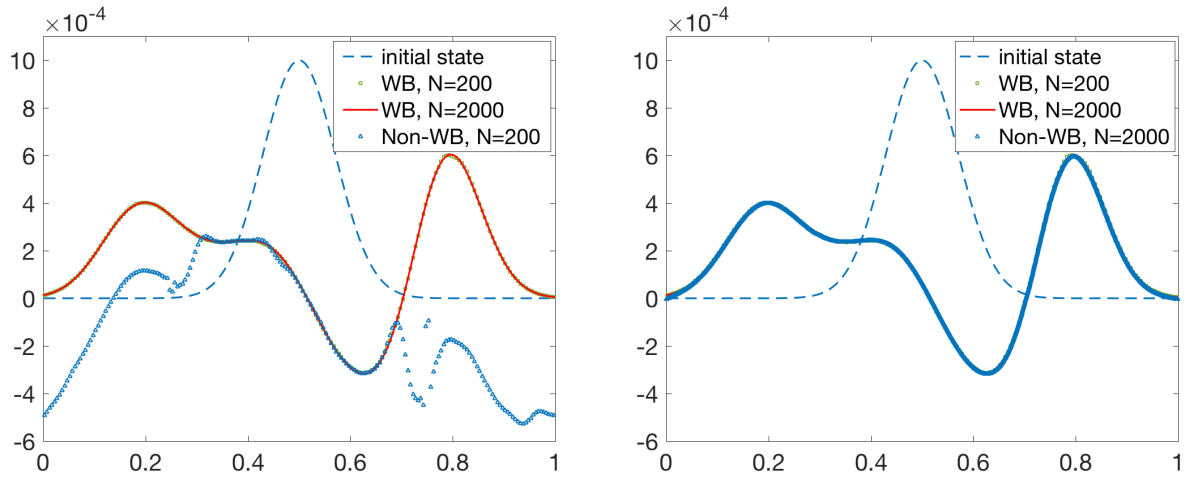


Figure 2.8 Example 2.3: Pressure perturbation $(p(y, 0.25) - e^{-\sin(2\pi y)})$ computed by the well-balanced (WB) and non-well-balanced (Non-WB) CU schemes for $\eta = 10^{-3}$ with $N = 200$ for each scheme (left) and $N = 2000$ for the non-well-balanced scheme (right). The reference solution is computed with $N = 2000$ grid pints.

2.4 The Two-Dimensional Euler Equations of Gas Dynamics With Gravitation

In this section, we describe the well-balanced semi-discrete CU scheme for the 2-D Euler equations of gas dynamics with gravitation. The 2-D system reads as

$$\mathbf{q}_t + \mathbf{F}(\mathbf{q})_x + \mathbf{G}(\mathbf{q})_y = \mathbf{S}(\mathbf{q}), \quad (2.69)$$

where $\mathbf{q} := (\rho, \rho u, \rho v, E)^T$ is a vector of conservative variables, and

$$\mathbf{F}(\mathbf{q}) := \begin{pmatrix} \rho u \\ \rho u^2 + p \\ \rho u v \\ u(E + p) \end{pmatrix} \quad \text{and} \quad \mathbf{G}(\mathbf{q}) := \begin{pmatrix} \rho v \\ \rho u v \\ \rho v^2 + p \\ v(E + p) \end{pmatrix} \quad (2.70)$$

are the fluxes in the x - and y -directions, respectively, and

$$\mathbf{S}(\mathbf{q}) := \begin{pmatrix} 0 \\ -\rho \phi_x \\ -\rho \phi_y \\ -\rho u \phi_x - \rho v \phi_y \end{pmatrix} \quad (2.71)$$

is the gravitational source term. The system (2.69)–(2.71) is closed using the following equation of state (EOS):

$$E = \frac{p}{\gamma - 1} + \frac{\rho}{2}(u^2 + v^2), \quad (2.72)$$

where γ stands for the specific heat ratio.

Similarly to the previous sections, our goal is to design a numerical scheme which exactly preserves the steady states of the system (2.69). First, we rewrite the system (2.69)–(2.72) as follows:

$$\begin{cases} \rho_t + (\rho u)_x + (\rho v)_y = 0, \\ (\rho u)_t + (\rho u^2 + K)_x + (\rho u v)_y = 0, \\ (\rho v)_t + (\rho u v)_x + (\rho v^2 + L)_y = 0, \\ E_t + (u(E + p))_x + (v(E + p))_y = -\rho u \phi_x - \rho v \phi_y. \end{cases} \quad (2.73)$$

This system can also be written in the vector form (2.69) with

$$\mathbf{q} := \begin{pmatrix} \rho \\ \rho u \\ \rho v \\ E \end{pmatrix}, \quad \mathbf{F}(\mathbf{q}) := \begin{pmatrix} \rho u \\ \rho u^2 + K \\ \rho u v \\ u(E + p) \end{pmatrix}, \quad \mathbf{G}(\mathbf{q}) := \begin{pmatrix} \rho v \\ \rho u v \\ \rho v^2 + L \\ v(E + p) \end{pmatrix}, \quad \mathbf{S}(\mathbf{q}) := \begin{pmatrix} 0 \\ 0 \\ 0 \\ -\rho u \phi_x - \rho v \phi_y \end{pmatrix},$$

where

$$K := p + Q \quad \text{end} \quad L := p + R, \quad (2.74)$$

are global variables with

$$Q(x, y, t) := \int_{-\infty}^x \rho(\xi, y, t) \phi_x(\xi, y) d\xi, \quad R(x, y, t) := \int_{-\infty}^y \rho(x, \eta, t) \phi_y(x, \eta) d\eta. \quad (2.75)$$

The motionless steady states are then given by

$$u = v \equiv 0, \quad K_x \equiv 0 \quad \text{and} \quad L_y \equiv 0. \quad (2.76)$$

In the succeeding sections, we illustrate the well-balanced numerical scheme to resolve the steady state solutions of the system (2.73)-(2.75).

2.4.1 Well-Balanced Central-Upwind Scheme

We consider a rectangular computational domain and partition it into the uniform Cartesian cells $C_{j,k} := [x_{j-\frac{1}{2}}, x_{j+\frac{1}{2}}] \times [y_{k-\frac{1}{2}}, y_{k+\frac{1}{2}}]$ of size $|C_{j,k}| = \Delta x \Delta y$ centered at (x_j, y_k) , $j = j_L, \dots, j_R$, $k = k_L, \dots, k_R$. We assume that at a certain time level t , the cell averages of the computed numerical solution,

$$\bar{\mathbf{q}}_{j,k}(t) := \frac{1}{\Delta x \Delta y} \iint_{C_{j,k}} \mathbf{q}(x, y, t) dx dy,$$

are available.

2.4.1.1 Well-Balanced Reconstruction

Similarly to the 1-D case, we reconstruct only the first three components of the conservative variables, q , $(\rho, \rho u$ and $\rho v)$:

$$\tilde{q}^{(i)}(x, y) = \bar{q}_{j,k}^{(i)} + (q_x^{(i)})_{j,k}(x - x_j) + (q_y^{(i)})_{j,k}(y - y_k), \quad (x, y) \in C_{j,k}, \quad i = 1, 2, 3,$$

and compute the corresponding point values at the cell interfaces $(x_{j \pm \frac{1}{2}}, y_k)$ and $(x_j, y_{k \pm \frac{1}{2}})$:

$$\begin{aligned} (q^{(i)})_{j,k}^E &:= \tilde{q}^{(i)}(x_{j+\frac{1}{2}} - 0, y_k) = \bar{q}_{j,k}^{(i)} + \frac{\Delta x}{2}(q_x^{(i)})_{j,k}, \\ (q^{(i)})_{j,k}^W &:= \tilde{q}^{(i)}(x_{j-\frac{1}{2}} + 0, y_k) = \bar{q}_{j,k}^{(i)} - \frac{\Delta x}{2}(q_x^{(i)})_{j,k}, \\ (q^{(i)})_{j,k}^N &:= \tilde{q}^{(i)}(x_j, y_{k+\frac{1}{2}} - 0) = \bar{q}_{j,k}^{(i)} + \frac{\Delta y}{2}(q_y^{(i)})_{j,k}, \\ (q^{(i)})_{j,k}^S &:= \tilde{q}^{(i)}(x_j, y_{k-\frac{1}{2}} + 0) = \bar{q}_{j,k}^{(i)} - \frac{\Delta y}{2}(q_y^{(i)})_{j,k}, \end{aligned} \quad i = 1, 2, 3,$$

where the slopes $(q_x^{(i)})_{j,k}$ and $(q_y^{(i)})_{j,k}$ are computed as in (2.20).

The point values for the forth conservative variable E should be calculated from the new equilibrium variables obtained from the reconstruction of K and L . We stress that since at the steady states (2.76), $K = K(y)$ is independent of x and $L = L(x)$ is independent of y , we, in fact, perform 1-D reconstructions for K and L in the x - and y -directions, respectively.

To this end, we first use the midpoint rule to compute the point values of the integrals Q and R in (2.75) at the cell interfaces in the x - and y -directions, respectively:

$$\begin{aligned} Q_{j_L-\frac{1}{2},k} = 0, \quad & \begin{cases} Q_{j+\frac{1}{2},k} = Q_{j-\frac{1}{2},k} + \Delta x \bar{\rho}_{j,k}(\phi_x)_{j,k}, \\ Q_{j,k} = \frac{1}{2}(Q_{j-\frac{1}{2},k} + Q_{j+\frac{1}{2},k}), \end{cases} \quad j = j_L, \dots, j_R, \quad k = k_L, \dots, k_R, \\ R_{j,k_L-\frac{1}{2}} = 0, \quad & \begin{cases} R_{j,k+\frac{1}{2}} = R_{j,k-\frac{1}{2}} + \Delta y \bar{\rho}_{j,k}(\phi_y)_{j,k}, \\ R_{j,k} = \frac{1}{2}(R_{j,k-\frac{1}{2}} + R_{j,k+\frac{1}{2}}), \end{cases} \quad j = j_L, \dots, j_R, \quad k = k_L, \dots, k_R, \end{aligned}$$

where $(\phi_x)_{j,k} := \phi_x(x_j, y_k)$ and $(\phi_y)_{j,k} := \phi_y(x_j, y_k)$. We then compute the cell center values

$K_{j,k}$ and $L_{j,k}$ as follows:

$$K_{j,k} = p_{j,k} + Q_{j,k} \quad \text{and} \quad L_{j,k} = p_{j,k} + R_{j,k}.$$

We now obtain the point values of K and L at the cell interfaces in the x - and y -directions, respectively:

$$\begin{aligned} K_{j,k}^E &= K_{j,k} + \frac{\Delta x}{2}(K_x)_{j,k}, & K_{j,k}^W &= K_{j,k} - \frac{\Delta x}{2}(K_x)_{j,k}, \\ L_{j,k}^N &= L_{j,k} + \frac{\Delta y}{2}(L_y)_{j,k}, & L_{j,k}^S &= L_{j,k} - \frac{\Delta y}{2}(L_y)_{j,k}, \end{aligned} \quad (2.77)$$

where

$$(K_x)_{j,k} = \text{minmod}\left(\theta \frac{K_{j+1,k} - K_{j,k}}{\Delta x}, \frac{K_{j+1,k} - K_{j-1,k}}{2\Delta x}, \theta \frac{K_{j,k} - K_{j-1,k}}{\Delta x}\right)$$

and

$$(L_y)_{j,k} = \text{minmod}\left(\theta \frac{L_{j,k+1} - L_{j,k}}{\Delta y}, \frac{L_{j,k+1} - L_{j,k-1}}{2\Delta y}, \theta \frac{L_{j,k} - L_{j,k-1}}{\Delta y}\right).$$

Finally, the values obtained in (2.77) are used to evaluate the point values of p from (2.74):

$$\begin{aligned} p_{j,k}^E &= K_{j,k}^E - Q_{j+\frac{1}{2},k}, & p_{j,k}^W &= K_{j,k}^W - Q_{j-\frac{1}{2},k}, \\ p_{j,k}^N &= L_{j,k}^N - R_{j,k+\frac{1}{2}}, & p_{j,k}^S &= L_{j,k}^S - R_{j,k-\frac{1}{2}}, \end{aligned} \quad (2.78)$$

and then the corresponding point values of E are calculated from the EOS (2.72).

2.4.1.2 Well-Balanced Evolution

The cell-averages of \bar{q} are evolved in time according to the following system of ODEs:

$$\frac{d}{dt} \bar{q}_{j,k} = -\frac{\mathcal{F}_{j+\frac{1}{2},k} - \mathcal{F}_{j-\frac{1}{2},k}}{\Delta x} - \frac{\mathcal{G}_{j,k+\frac{1}{2}} - \mathcal{G}_{j,k-\frac{1}{2}}}{\Delta y} + \bar{S}_{j,k}, \quad (2.79)$$

where \mathcal{F} and \mathcal{G} are numerical fluxes. Introducing the notations

$$\alpha_{j+\frac{1}{2},k} := \frac{a_{j+\frac{1}{2},k}^+ a_{j+\frac{1}{2},k}^-}{a_{j+\frac{1}{2},k}^+ - a_{j+\frac{1}{2},k}^-} \quad \text{and} \quad \beta_{j,k+\frac{1}{2}} := \frac{b_{j,k+\frac{1}{2}}^+ b_{j,k+\frac{1}{2}}^-}{b_{j,k+\frac{1}{2}}^+ - b_{j,k+\frac{1}{2}}^-},$$

we write the components of $\mathcal{F}_{j+\frac{1}{2},k}$ and $\mathcal{G}_{j,k+\frac{1}{2}}$ as

$$\begin{aligned}
\mathcal{F}_{j+\frac{1}{2},k}^{(1)} &= \frac{a_{j+\frac{1}{2},k}^+(\rho u)_{j,k}^E - a_{j+\frac{1}{2},k}^-(\rho u)_{j+1,k}^W}{a_{j+\frac{1}{2},k}^+ - a_{j+\frac{1}{2},k}^-} \\
&\quad + \alpha_{j+\frac{1}{2},k} H \left(\frac{|K_{j+1,k} - K_{j,k}|}{\Delta x} \cdot \frac{x_{k_R+\frac{1}{2}} - x_{k_L-\frac{1}{2}}}{\max_{j,k}\{K_{j,k}, K_{j+1,k}\}} \right) \cdot (\rho_{j+1,k}^W - \rho_{j,k}^E - \delta \rho_{j+\frac{1}{2},k}), \\
\mathcal{F}_{j+\frac{1}{2},k}^{(2)} &= \frac{a_{j+\frac{1}{2},k}^+(\rho_{j,k}^E (u_{j,k}^E)^2 + K_{j,k}^E) - a_{j+\frac{1}{2},k}^-(\rho_{j+1,k}^W (u_{j+1,k}^W)^2 + K_{j+1,k}^W)}{a_{j+\frac{1}{2},k}^+ - a_{j+\frac{1}{2},k}^-} \\
&\quad + \alpha_{j+\frac{1}{2},k} ((\rho u)_{j+1,k}^W - (\rho u)_{j,k}^E - \delta(\rho u)_{j+\frac{1}{2},k}), \\
\mathcal{F}_{j+\frac{1}{2},k}^{(3)} &= \frac{a_{j+\frac{1}{2},k}^+ \rho_{j,k}^E u_{j,k}^E v_{j,k}^E - a_{j+\frac{1}{2},k}^- \rho_{j+1,k}^W u_{j+1,k}^W v_{j+1,k}^W}{a_{j+\frac{1}{2},k}^+ - a_{j+\frac{1}{2},k}^-} + \alpha_{j+\frac{1}{2},k} ((\rho v)_{j+1,k}^W - (\rho v)_{j,k}^E - \delta(\rho v)_{j+\frac{1}{2},k}), \\
\mathcal{F}_{j+\frac{1}{2},k}^{(4)} &= \frac{a_{j+\frac{1}{2},k}^+ u_{j,k}^E (E_{j,k}^E + p_{j,k}^E) - a_{j+\frac{1}{2},k}^- u_{j+1,k}^W (E_{j+1,k}^W + p_{j+1,k}^W)}{a_{j+\frac{1}{2},k}^+ - a_{j+\frac{1}{2},k}^-} + \alpha_{j+\frac{1}{2},k} (E_{j+1,k}^W - E_{j,k}^E - \delta E_{j+\frac{1}{2},k}), \\
\\
\mathcal{G}_{j,k+\frac{1}{2}}^{(1)} &= \frac{b_{j,k+\frac{1}{2}}^+(\rho v)_{j,k}^N - b_{j,k+\frac{1}{2}}^-(\rho v)_{j,k+1}^S}{b_{j,k+\frac{1}{2}}^+ - b_{j,k+\frac{1}{2}}^-} \\
&\quad + \beta_{j,k+\frac{1}{2}} H \left(\frac{|L_{j,k+1} - L_{j,k}|}{\Delta y} \cdot \frac{y_{k_R+\frac{1}{2}} - y_{k_L-\frac{1}{2}}}{\max_{j,k}\{L_{j,k}, L_{j,k+1}\}} \right) \cdot (\rho_{j,k+1}^S - \rho_{j,k}^N - \delta \rho_{j,k+\frac{1}{2}}), \\
\mathcal{G}_{j,k+\frac{1}{2}}^{(2)} &= \frac{b_{j,k+\frac{1}{2}}^+ \rho_{j,k}^N u_{j,k}^N v_{j,k}^N - b_{j,k+\frac{1}{2}}^- \rho_{j,k+1}^S u_{j,k+1}^S v_{j,k+1}^S}{b_{j,k+\frac{1}{2}}^+ - b_{j,k+\frac{1}{2}}^-} + \beta_{j,k+\frac{1}{2}} ((\rho u)_{j,k+1}^S - (\rho u)_{j,k}^N - \delta(\rho u)_{j,k+\frac{1}{2}}), \\
\mathcal{G}_{j,k+\frac{1}{2}}^{(3)} &= \frac{b_{j,k+\frac{1}{2}}^+ (\rho_{j,k}^N (v_{j,k}^N)^2 + L_{j,k}^N) - b_{j,k+\frac{1}{2}}^- (\rho_{j,k+1}^S (v_{j,k+1}^S)^2 + L_{j,k+1}^S)}{b_{j,k+\frac{1}{2}}^+ - b_{j,k+\frac{1}{2}}^-} \\
&\quad + \beta_{j,k+\frac{1}{2}} ((\rho v)_{j,k+1}^S - (\rho v)_{j,k}^N - \delta(\rho v)_{j,k+\frac{1}{2}}), \\
\mathcal{G}_{j,k+\frac{1}{2}}^{(4)} &= \frac{b_{j,k+\frac{1}{2}}^+ v_{j,k}^N (E_{j,k}^N + p_{j,k}^N) - b_{j,k+\frac{1}{2}}^- v_{j,k+1}^S (E_{j,k+1}^S + p_{j,k+1}^S)}{b_{j,k+\frac{1}{2}}^+ - b_{j,k+\frac{1}{2}}^-} + \beta_{j,k+\frac{1}{2}} (E_{j,k+1}^S - E_{j,k}^N - \delta E_{j,k+\frac{1}{2}}),
\end{aligned}$$

where the function H in the first components of the x - and y -numerical fluxes is defined, as before, in (2.63). As mentioned earlier, the local speeds are obtained from the smallest and largest eigenvalues of Jacobians $\partial \mathbf{F}/\partial \mathbf{q}$ and $\partial \mathbf{G}/\partial \mathbf{q}$, which are given explicitly as follows:

$$\begin{aligned} a_{j+\frac{1}{2},k}^+ &= \max(u_{j,k}^E + c_{j,k}^E, u_{j+1,k}^W + c_{j+1,k}^W, 0), & a_{j+\frac{1}{2},k}^- &= \min(u_{j,k}^E - c_{j,k}^E, u_{j+1,k}^W - c_{j+1,k}^W, 0), \\ b_{j,k+\frac{1}{2}}^+ &= \max(v_{j,k}^N + c_{j,k}^N, v_{j,k+1}^S + c_{j,k+1}^S, 0), & b_{j,k+\frac{1}{2}}^- &= \min(v_{j,k}^N - c_{j,k}^N, v_{j,k+1}^S - c_{j,k+1}^S, 0), \end{aligned} \quad (2.80)$$

where the velocities $u_{j,k}^E, u_{j+1,k}^W, v_{j,k}^N$ and $v_{j,k+1}^S$ are obtained from the identities $u \equiv (\rho u)/\rho$ and $v \equiv (\rho v)/\rho$ and the speeds of sound $c_{j,k}^E, c_{j+1,k}^W, c_{j,k}^N$ and $c_{j,k+1}^S$ are computed from the definition $c^2 = \gamma p/\rho$.

The cell averages of the source term in (2.79) are approximated using the midpoint rule as follows:

$$\bar{\mathbf{S}}_{j,k} = (0, 0, 0, -(\overline{\rho u})_{j,k}(\phi_x)_{j,k} - (\overline{\rho v})_{j,k}(\phi_y)_{j,k})^T. \quad (2.81)$$

Finally, we state the following well-balanced property of the proposed 2-D CU scheme.

Theorem 2.4.1 *The 2-D semi-discrete CU scheme described in Section 2.4.1.1 and Section 2.4.1.2 above is well-balanced in the sense that it exactly preserves the steady state (2.76).*

Proof: We assume that the following equilibriums hold at certain time level $t = t^n$:

$$u_{j,k}^E \equiv u_{j,k} \equiv u_{j,k}^W \equiv 0, \quad v_{j,k}^N \equiv v_{j,k} \equiv v_{j,k}^S \equiv 0, \quad (2.82)$$

$$K_{j,k}^E \equiv K_{j,k} \equiv K_{j,k}^W \equiv \widehat{K}, \quad L_{j,k}^N \equiv L_{j,k} \equiv L_{j,k}^S \equiv \widehat{L}, \quad (2.83)$$

where \widehat{K} and \widehat{L} are constants. Similarly to the 1-D case, to prove the well-balanced property of the scheme, the right hand side of the equation (2.79) should vanish. By considering (2.82), the source term $\bar{\mathbf{S}}_{j,k}$ given in (2.81) is equal to zero. Thus, we only need to show that the numerical fluxes in both x - and y - directions are constant.

The equalities in (2.82) and (2.83) result in $\mathcal{F}_{j+\frac{1}{2},k}^{(1)} = 0$, where (2.83) yields $H\left(\frac{|K_{j+1,k} - K_{j,k}|}{\Delta x} \cdot \frac{x_{k_R+\frac{1}{2}} - x_{k_L-\frac{1}{2}}}{\max_{j,k}\{K_{j,k}, K_{j+1,k}\}}\right) = H(0) = 0$. The second term of $\mathcal{F}_{j+\frac{1}{2},k}^{(2)}$ also vanishes since $u_{j,k}^E \equiv u_{j,k} \equiv u_{j,k}^W \equiv 0$ and then we have $\mathcal{F}_{j+\frac{1}{2},k}^{(2)} = \widehat{K}$ resulting in $\mathcal{F}_{j+\frac{1}{2},k}^{(2)} - \mathcal{F}_{j-\frac{1}{2},k}^{(2)} = 0$. The third component of the numerical fluxes in the x -direction, $\mathcal{F}_{j+\frac{1}{2},k}^{(3)}$, is immediately equal

to zero by (2.82). Finally, the first term of $\mathcal{F}_{j+\frac{1}{2},k}^{(4)}$ becomes zero and the rest of $\mathcal{F}_{j+\frac{1}{2},k}^{(4)}$ can be computed as follows:

$$\begin{aligned}
\mathcal{F}_{j+\frac{1}{2},k}^{(4)} &= \alpha_{j+\frac{1}{2},k} (E_{j+1,k}^W - E_{j,k}^E - \delta E_{j+\frac{1}{2},k}) \\
&= \alpha_{j+\frac{1}{2},k} \left(\frac{p_{j+1,k}^W}{\gamma-1} - \frac{p_{j,k}^E}{\gamma-1} - \min\text{mod}(a_{j+\frac{1}{2},k}^+, -a_{j+\frac{1}{2},k}^-) \left(\frac{p_{j+1,k}^W}{\gamma-1} - \frac{p_{j,k}^E}{\gamma-1} \right) \right) \\
&= \alpha_{j+\frac{1}{2},k} \left(\left(1 - \min\text{mod}(a_{j+\frac{1}{2},k}^+, -a_{j+\frac{1}{2},k}^-) \right) \left(\frac{K_{j+1,k}^W - Q_{j+\frac{1}{2},k}}{\gamma-1} - \frac{K_{j,k}^E - Q_{j+\frac{1}{2},k}}{\gamma-1} \right) \right) \\
&= 0,
\end{aligned}$$

since $p_{j,k}^E = K_{j,k}^E - Q_{j+\frac{1}{2},k}$ and $p_{j+1,k}^W = K_{j+1,k}^W - Q_{j+\frac{1}{2},k}$ from (2.78).

Similarly to the x -direction, the first and second components of the numerical fluxes in the y -direction, $\mathcal{G}_{j,k+\frac{1}{2}}^{(1)}$ and $\mathcal{G}_{j,k+\frac{1}{2}}^{(2)}$ are equal to zero according to the equations in (2.82) and (2.83). The third one is $\mathcal{G}_{j,k+\frac{1}{2}}^{(3)} = \widehat{L}$, which gives $\mathcal{G}_{j,k+\frac{1}{2}}^{(3)} - \mathcal{G}_{j,k-\frac{1}{2}}^{(3)} = 0$. Lastly, by following (2.78), (2.82) and (2.83), $\mathcal{G}_{j,k+\frac{1}{2}}^{(4)}$ also yields to zero.

Hence, the right hand side of (2.79) vanishes and the scheme preserves the state-states (2.76). ■

2.4.2 Numerical Examples

In this section, we present a number of 2-D numerical examples, in which we demonstrate the performance of the proposed well-balanced semi-discrete CU scheme.

In all of the examples below, we have used the three-stage third-order strong stability preserving Runge-Kutta method (see, e.g., [58, 60, 144] and Appendix A.1) to solve the ODE system (2.79). The CFL number in (2.22) has been set to $\kappa = 0.4$. Also, we have used the following constant values: the minmod parameter $\theta = 1.3$ and the specific heat ratio $\gamma = 1.4$.

Example 2.7—Isothermal equilibrium solution.

The first 2-D example was studied in [154]. We consider the system (2.73) with $g = 1$ subject to the initial data that are in isothermal equilibrium:

$$\rho(x, y, 0) = \rho_0 e^{-\frac{\rho_0 g y}{p_0}}, \quad p(x, y, 0) = p_0 e^{-\frac{\rho_0 g y}{p_0}}, \quad u(x, y, 0) \equiv v(x, y, 0) \equiv 0, \quad (2.84)$$

where $\rho_0 = 1.21$ and $p_0 = 1$, and the solid wall boundary conditions imposed at the edges of the unit square $[0, 1] \times [0, 1]$.

We compute the solution until the final time $T = 1$ using the proposed well-balanced CU scheme on 50×50 , 100×100 and 200×200 uniform cells. On all of these grids, the initial data are preserved within the machine accuracy. On contrary, the non-well-balanced CU scheme preserves the initial equilibrium within the accuracy of the scheme only, as can be seen in Table 2.9, where we present the L^1 -errors for both ρ , ρu , ρv and E components of the non-well-balanced solution.

Table 2.9 Example 2.7: L^1 -errors for the non-well-balanced CU scheme.

$N \times N$	ρ	ρu	ρv	E	u	v	p
50×50	2.54E-03	0.00E+00	1.02E-04	1.16E-03	0.00E+00	1.72E-04	4.64E-04
100×100	1.07E-03	0.00E+00	1.54E-04	7.93E-04	0.00E+00	1.93E-04	3.17E-04
200×200	3.96E-04	0.00E+00	5.04E-05	2.66E-04	0.00E+00	6.39E-05	1.06E-04

Next, we add a small perturbation to the initial pressure (compare with (2.84)):

$$p(x, y, 0) = p_0 e^{-\frac{\rho_0 g y}{p_0}} + \eta e^{-\frac{100 \rho_0 g}{p_0} ((x-0.3)^2 + (y-0.3)^2)}, \quad \eta = 10^{-3}.$$

In Figures 2.9 and 2.10 (upper row), we plot the pressure computed by both the well-balanced and non-well-balanced CU schemes at time $T = 0.15$ using 50×50 uniform cells. As one can clearly see, the well-balanced CU scheme can capture the small pressure perturbation much more accurately than the non-well-balanced one. When the mesh is refined to 200×200 uniform cells, the non-well-balanced solution becomes better, but still

less accurate than the well-balanced one, see Figure 2.10 (lower row).

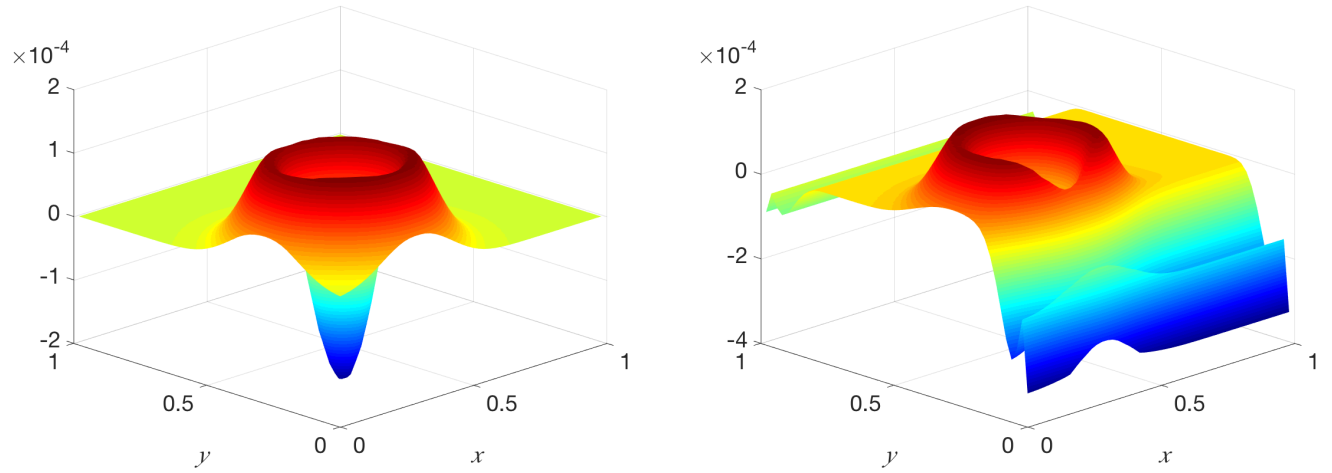


Figure 2.9 Example 2.7: Pressure perturbation computed by the well-balanced (left) and non-well-balanced (right) CU schemes using 50×50 uniform cells.

Example 2.8—Explosion.

In the second 2-D example, we compare the performance of well-balanced and non-well-balanced CU schemes in an explosion setting and demonstrate nonphysical shock waves generated by non-well-balanced scheme.

We solve the system (2.73) with $g = 0.118$ in the computational domain $[0, 3] \times [0, 3]$, subject to the following initial data:

$$\rho(x, y, 0) \equiv 1, \quad u(x, y, 0) \equiv 0, \quad p(x, y, 0) = 1 - g y + \begin{cases} 0.005, & (x - 1.5)^2 + (y - 1.5)^2 < 0.01, \\ 0, & \text{otherwise.} \end{cases}$$

Zero-order extrapolation is used as the boundary conditions in all of the directions.

We use a uniform grid with 101×101 cells and compute the solution by both the well-balanced and non-well-balanced CU schemes until the final time $T = 2.4$. At first, a circular

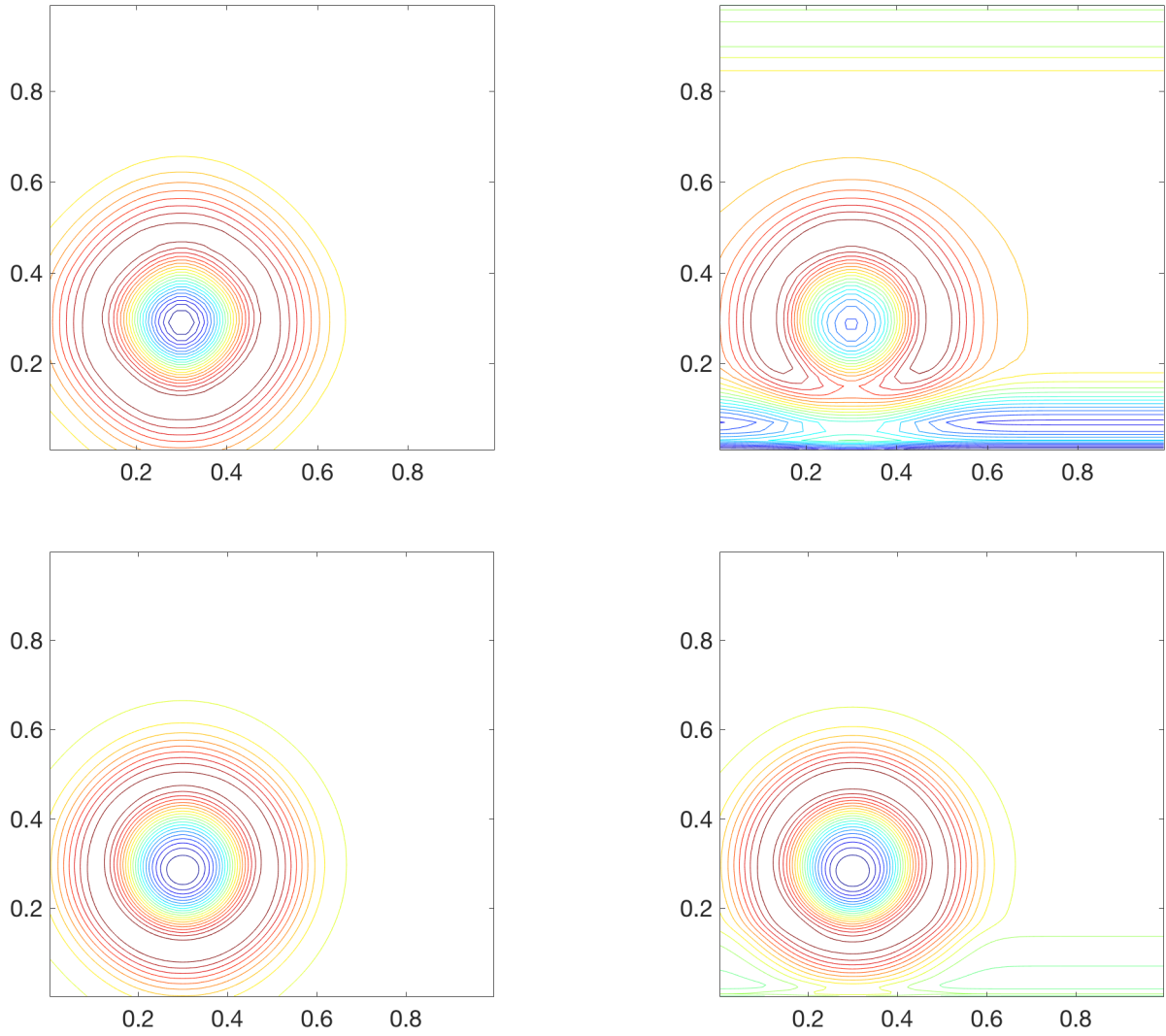


Figure 2.10 Example 2.7: Contour plot of the pressure perturbation computed by well-balanced (left column) and non-well-balanced (right column) CU schemes using 50×50 (upper row) and 200×200 (lower row) uniform cells.

shock wave is developed and later on it transmits through the boundary. Due to the heat generated by the explosion, the gas at the center expands and its density decreases generating a positive vertical momentum at the center of the domain. In Figures 2.11 and 2.12, we plot the solution (ρ and $\sqrt{u^2 + v^2}$ at times $t = 1.2, 1.8$ and 2.4) computed by the well-balanced and non-well-balanced schemes, respectively. As one can see, the well-balanced scheme accurately captures the behavior of the solution at all stages, while the non-well-balanced scheme produces significant oscillations at the smaller time $t = 1.2$, which totally dominate the solution, especially its velocity field, by the final time $T = 2.4$.

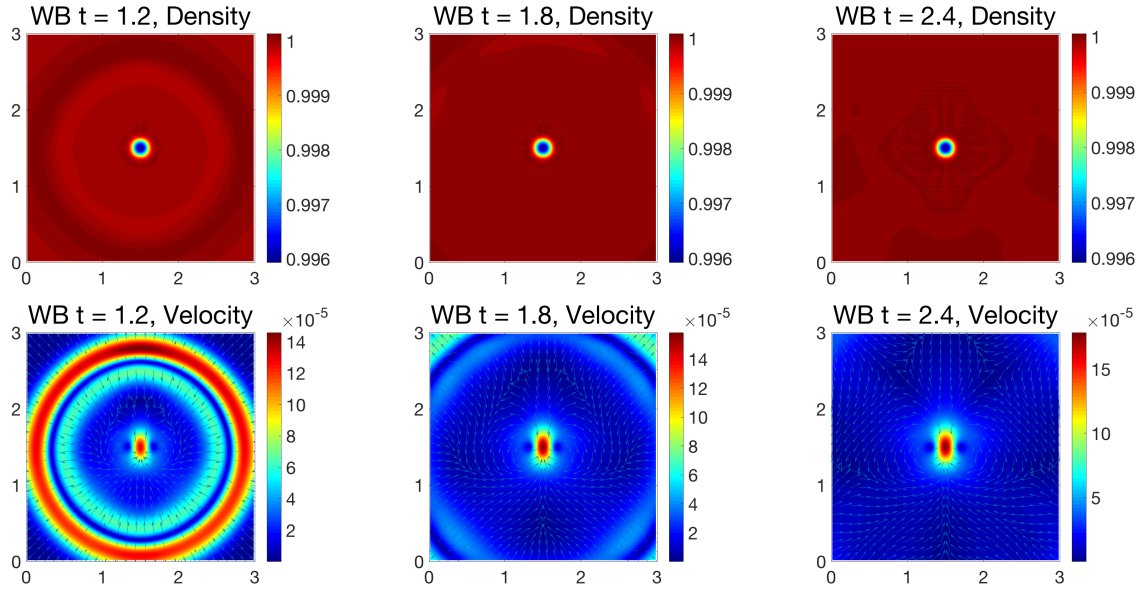


Figure 2.11 Example 2.8: Density (ρ) and velocity ($\sqrt{u^2 + v^2}$) computed by the well-balanced CU scheme.

2.5 Conclusions

In this chapter, we developed a well-balanced second-order central-upwind scheme for various types of balance laws. Particularly, we first considered 2×2 systems of balance laws,

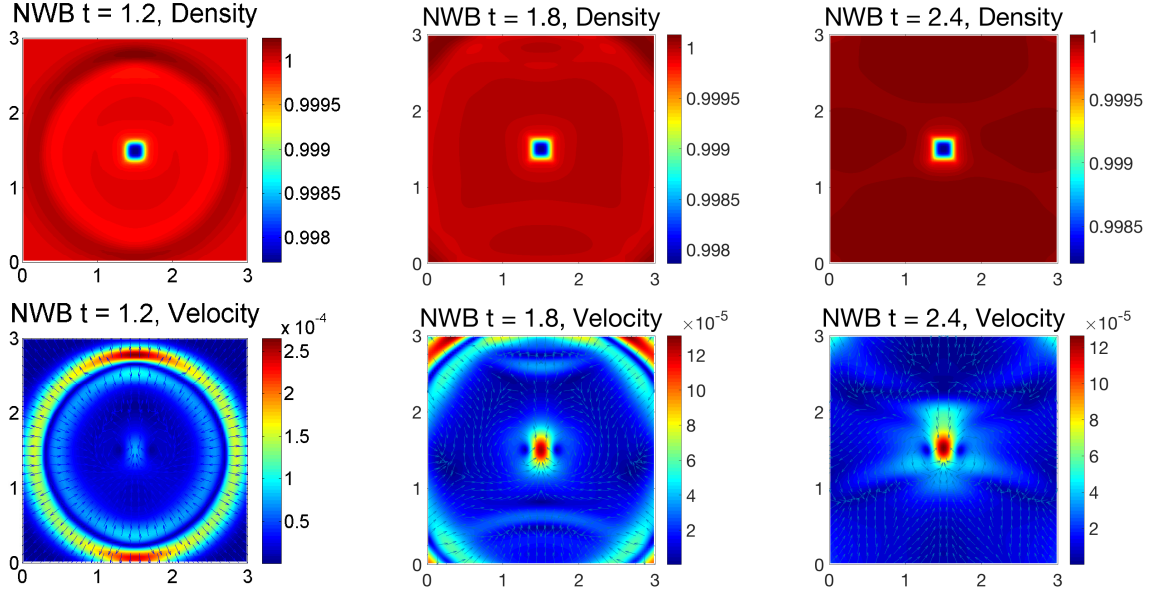


Figure 2.12 Example 2.8: Density (ρ) and velocity ($\sqrt{u^2 + v^2}$) computed by the non-well-balanced CU scheme.

which is used to model, for instance, gas flow in high-pressure transmission pipelines and traffic flow with relaxation. We presented the results of one-dimensional model, in which, steady states are captured exactly by the proposed well-balanced scheme. As an ongoing study, several physical models including the two-dimensional systems will be examined.

Furthermore, we considered one- and two-dimensional Euler equations of gas dynamics under gravitational field. We applied the developed well-balanced central-upwind scheme to numerous systems including both linear and nonlinear gravitational potentials and proved that steady state solutions and their small perturbations are preserved by the new well-balanced scheme. As a consecutive work, non-smooth steady-states with the strong shock formation will be worth to test the performance of the well-balanced scheme.

Part II

Kinetic Chemotaxis Models

CHAPTER 3

An Asymptotic Preserving Scheme for Kinetic Chemotaxis Models in Two Space Dimensions

The contents of this chapter have been submitted to Kinetic and Related Models, [32].

3.1 Introduction

Chemotaxis is the movement of cells along the chemical gradient in a medium and it is often modeled by systems of PDEs. The classical PDE chemotaxis model is the Patlak-Keller-Segel (PKS) system [87–89, 134], which is derived at the macroscopic level in terms of the cell density and chemoattractant concentration. In the 2-D case, this model reads as

$$\rho_t = \nabla \cdot (D \nabla \rho - \chi \rho \nabla S), \quad (3.1)$$

$$\tau S_t = \alpha \Delta S - \beta S + \gamma \rho, \quad (3.2)$$

where $\mathbf{x} = (x, y) \in \Omega \subset \mathbb{R}^2$ are spatial variables and t is time, $\rho(\mathbf{x}, t)$ is the cell density and $S(\mathbf{x}, t)$ is the chemoattractant concentration, D and α are positive diffusion constants, χ is the chemotactic sensitivity constant, and the positive constants γ and β stand for the

production and degradation rates of the chemoattractant, respectively. The constant τ determines the type of the system: It is parabolic-parabolic if $\tau = 1$ and parabolic-elliptic for $\tau = 0$. In recent years, several modifications of the PKS system have also been studied; see, e.g., [22, 33, 70–72, 94, 135] and references therein.

In order to describe the chemotaxis at the cellular (microscopic) level, a class of Boltzmann-type kinetic equations has been developed. A stochastic approach based on the velocity-jump process was introduced in [147] and was later used in the framework of kinetic chemotaxis models in [3, 129, 145]. The velocity-jump process characterizes the movement in two phases, namely, *run* and *tumble*. During the *run* phase, cells move (almost) linearly with constant speed and in the *tumble* phase, they reorient their motion with a new velocity and direction. The Boltzmann-type kinetic model reads as

$$f_t + \mathbf{v} \cdot \nabla_{\mathbf{x}} f = \int_V (T[S]f' - T^*[S]f) d\mathbf{v}', \quad (3.3)$$

where $f := f(\mathbf{x}, t, \mathbf{v})$ is the probability density function (pdf) of cells at the position \mathbf{x} with the velocity $\mathbf{v} = (u, v) \in V \subset \mathbb{R}^2$ at a given time t , and $f' := f(\mathbf{x}, t, \mathbf{v}')$. In (3.3), $T[S]$ is the turning kernel operator, which describes the velocity change from \mathbf{v}' to \mathbf{v} at (\mathbf{x}, t) , that is, $T[S] := T[S](\mathbf{x}, t, \mathbf{v}, \mathbf{v}')$ and $T^*[S] := T[S](\mathbf{x}, t, \mathbf{v}', \mathbf{v})$. Specifying the turning kernel T is a crucial point in the kinetic chemotaxis modeling, which will be discussed in the §3.2. Notice that the microscopic pdf f is related to the macroscopic cell density ρ in the following way:

$$\rho(\mathbf{x}, t) := \int_V f(\mathbf{x}, t, \mathbf{v}) d\mathbf{v}. \quad (3.4)$$

Applying the parabolic scaling to (3.3) yields the following non-dimensionalized kinetic equation (see, e.g., [25, 68, 130]):

$$\varepsilon f_t + \mathbf{v} \cdot \nabla_{\mathbf{x}} f = \frac{1}{\varepsilon} \int_V (T_\varepsilon[S]f' - T_\varepsilon^*[S]f) d\mathbf{v}' \quad (3.5)$$

with the non-dimensional scaling parameter (mean-free path) ε and the new notations: $f := f_\varepsilon(\mathbf{x}, t, \mathbf{v})$, $f' := f_\varepsilon(\mathbf{x}, t, \mathbf{v}')$, $T_\varepsilon[S] := T_\varepsilon[S](\mathbf{x}, t, \mathbf{v}, \mathbf{v}')$ and $T_\varepsilon^*[S] := T_\varepsilon[S](\mathbf{x}, t, \mathbf{v}', \mathbf{v})$.

The question of convergence (in the singular limit as $\varepsilon \rightarrow 0$) of the kinetic model (3.5) to the PKS system (3.1), (3.2) has been extensively studied. More precisely, the global in time convergence was proven in the parabolic-elliptic case in [25]. In the parabolic-parabolic case, only local convergence results were established; see [76]. We also refer the reader to [130] for more results on the limiting process.

It is well-known that if the total number of cells is sufficiently large, a concentration phenomenon may occur and can be modeled by both the PKS (3.1), (3.2) and kinetic-chemotaxis (3.5), (3.2) systems. It should be observed that under the assumption that no-flux conditions are imposed at the boundary of the domain Ω , the total mass

$$M := \int_{\Omega} \rho(x, t) dx \tag{3.6}$$

is conserved for both models, but the solution behavior depends on the value of M . For instance, the solution of the 2-D PKS system (3.1), (3.2) may develop δ -type singularities in finite time if M is larger than some critical value M_c ; see, e.g., [21, 34, 52, 65–67, 69, 78, 124]. Otherwise, the solution of (3.1), (3.2) exists globally in time. In the parabolic-elliptic case ($\tau = 0$), the critical mass values are explicitly available, while this is not the case for the parabolic-parabolic system ($\tau = 1$); see, e.g., [135]. The kinetic-chemotaxis system (3.5), (3.2) exhibits a similar behavior, which depends, however, not only on the value of the initial mass M , but also on the choice of the specific kernel T_ε ; see, e.g., [15, 25]. At the same time, the kinetic-chemotaxis system provides a more detailed description of the underlying cell dynamics and thus may be advantageous in a variety of applications.

In this chapter, we develop an efficient and accurate numerical method for the kinetic-chemotaxis system (3.5), (3.2). As it was discussed before, one of the difficulties in achieving this goal is related to the fact that the studied system is stiff when $0 < \varepsilon \ll 1$. If a naïve numerical discretization is used, then one may need to take both spatial and temporal discretization parameters to be proportional to $\mathcal{O}(\varepsilon)$ or even $\mathcal{O}(\varepsilon^2)$ due to stability restrictions, which may become unaffordable for small ε . To overcome this difficulty, we develop an asymptotic-preserving (AP) scheme, which yields a consistent approximation of the limiting macroscopic PKS system as $\varepsilon \rightarrow 0$ and is stable on a coarse spatio-temporal grid with the mesh parameters being independent of ε . The AP methods were first introduced

in [82] to solve kinetic equations in diffusive regimes and were later generalized for a variety of kinetic models; see, e.g., [39, 40, 44, 47, 74, 75, 79, 84, 107].

The AP property of our numerical approach is achieved by implementing an operator splitting technique combined with an idea of the even-odd formulation; see, e.g., [23, 85]. We split the system (3.5), (3.2) into the following two parts: a stiff nonlinear relaxation equations for the pdf and a non-stiff linear transport system coupled with the macroscopic equation (3.2) for the chemoattractant concentration. The nonlinear system is solved exactly, while the linear transport part is then solved by a second-order upwind method and the chemoattractant equation is treated by the spectral method.

3.2 Local Turning Kernel

In this section, we select a specific turning kernel T_ε , which models the reorientation process of the cells and will be used in the kinetic equation (3.5). To this end, we first write the formal asymptotic expansion (see, e.g., [23, 25, 48, 68, 130]):

$$T_\varepsilon[S] = T_0[S] + \varepsilon T_1[S] + \mathcal{O}(\varepsilon^2). \quad (3.7)$$

Here, the leading term $T_0[S] = F(v) > 0$ is the bounded velocity distribution at the equilibrium, which satisfies the following assumptions:

$$\int_V F(v) dv = 1 \quad \text{and} \quad F(v) = F(|v|). \quad (3.8)$$

The coefficient of the second term in (3.7), $T_1[S]$, describes the new favorable direction of the cells and we consider the positive *taxis* towards the chemoattractant.

Throughout this chapter, we employ the turning kernel operator introduced in [15], which represents a small perturbation of the equilibrium state:

$$T_\varepsilon[S](x, t, v, v') = F(v) + \varepsilon(v \cdot \nabla S(x, t))_+, \quad (3.9)$$

where $a_+ := \max(a, 0)$. Consequently, the kinetic equation (3.5) becomes:

$$\varepsilon f_t + \mathbf{v} \cdot \nabla_x f = \frac{\rho}{\varepsilon} [F(\mathbf{v}) + \varepsilon(\mathbf{v} \cdot \nabla S)_+] - \frac{1}{\varepsilon} (1 + \varepsilon \mathcal{J} |\nabla S|) f, \quad \mathcal{J} := \int_V \left(\frac{\mathbf{v} \cdot \nabla S}{|\nabla S|} \right)_+ d\mathbf{v}. \quad (3.10)$$

We note that alternative turning kernels have also been studied; see, e.g., [25, 76, 77]. It should be observed that the solution properties depend on the choice of the kernel. For instance, it was shown in [25] that the kinetic model (3.5), (3.2) with certain global kernel operators has a global solution for any initial mass. On the other hand, if the local kernel operator (3.9) is used, the solution may blow up. Indeed, as it has been proven in [15] for the parabolic-elliptic case, if the total mass $M > M_c = \frac{16\pi}{|V|}$, then the solution blows up, while if $M < m_c = \frac{0.806\pi}{|V|}$, then a classical solution exists globally in time. We also note that in the parabolic-parabolic case, the criteria for blow up or global existence are not explicitly known. In this chapter we develop an AP numerical method for the kinetic chemotaxis model (3.10), (3.2) and then use it to numerically investigate possible blowup scenarios in the parabolic-parabolic case.

3.3 Numerical Method

In this section, we present an AP scheme for the kinetic equation (3.10) coupled with the chemoattractant concentration equation (3.2). To this end, in §3.3.1, we first rewrite the system (3.5), (3.2) in the form convenient for numerical simulations using an even-odd formulation; see, e.g. [23, 85]. Then, in §3.3.2, we implement the Strang splitting approach, [146], by separating stiff and non-stiff parts of the system. In this setup, the stiff subsystem is solved exactly as described in §3.3.2.1, while the non-stiff subsystem becomes a system of linear transport equations, which is solved by a second-order upwind method presented in §3.3.2.2.

3.3.1 Even-Odd Formulation

In this section, we follow [23, 85] and introduce new variables r_1 , j_1 , r_2 and j_2 by considering the so-called even-odd formulation. We assume that $\mathbf{v} \in V := \{\mathbf{v} \mid |\mathbf{v}| = v_0\}$ and denote by

$V^+ := \{v = (u, v) \in V \mid u > 0, v > 0\}$. From now on, we consider $v \in V^+$ only and rewrite equation (3.10) as the system of four equations obtained by substituting (u, v) , $(-u, -v)$, $(u, -v)$, and $(-u, v)$ into (3.10):

$$\begin{aligned}
& \varepsilon f_t(u, v) + u f_x(u, v) + v f_y(u, v) \\
& \quad = \frac{\rho}{\varepsilon} [F(u, v) + \varepsilon(u S_x + v S_y)_+] - \frac{1}{\varepsilon} (1 + \varepsilon \mathcal{J} |\nabla S|) f(u, v), \\
& \varepsilon f_t(-u, -v) - u f_x(-u, -v) - v f_y(-u, -v) \\
& \quad = \frac{\rho}{\varepsilon} [F(-u, -v) - \varepsilon(u S_x + v S_y)_+] - \frac{1}{\varepsilon} (1 + \varepsilon \mathcal{J} |\nabla S|) f(-u, -v), \\
& \varepsilon f_t(u, -v) + u f_x(u, -v) - v f_y(u, -v) \\
& \quad = \frac{\rho}{\varepsilon} [F(u, -v) + \varepsilon(u S_x - v S_y)_+] - \frac{1}{\varepsilon} (1 + \varepsilon \mathcal{J} |\nabla S|) f(u, -v), \\
& \varepsilon f_t(-u, v) - u f_x(-u, v) + v f_y(-u, v) \\
& \quad = \frac{\rho}{\varepsilon} [F(-u, v) - \varepsilon(u S_x - v S_y)_+] - \frac{1}{\varepsilon} (1 + \varepsilon \mathcal{J} |\nabla S|) f(-u, v),
\end{aligned} \tag{3.11}$$

where $f(\pm u, \pm v)$ is used instead of $f(x, t, \pm u, \pm v)$ for the sake of simplicity. We then define the new variables

$$\begin{aligned}
r_1(u, v) &:= \frac{1}{2} [f(u, -v) + f(-u, v)], & r_2(u, v) &:= \frac{1}{2} [f(u, v) + f(-u, -v)], \\
j_1(u, v) &:= \frac{1}{2\varepsilon} [f(u, -v) - f(-u, v)], & j_2(u, v) &:= \frac{1}{2\varepsilon} [f(u, v) - f(-u, -v)],
\end{aligned} \tag{3.12}$$

with a one-to-one correspondence between them and f :

$$f(u, v) = \begin{cases} r_2 + \varepsilon j_2, & u > 0, v > 0, \\ r_2 - \varepsilon j_2, & u < 0, v < 0, \\ r_1 + \varepsilon j_1, & u > 0, v < 0, \\ r_1 - \varepsilon j_1, & u < 0, v > 0. \end{cases} \tag{3.13}$$

It is instructive to point out that the macroscopic cell density ρ can be obtained from (3.4) and (3.12) in terms of the new variables r_1 and r_2 :

$$\rho(x, t) = 2 \int_{V^+} [r_1(x, t, v) + r_2(x, t, v)] dv. \quad (3.14)$$

Substituting (3.13) into (3.11), yields the following system:

$$\begin{aligned} (r_1)_t + u(j_1)_x - v(j_1)_y &= \frac{\rho}{2\varepsilon^2} [2F(u, v) + \varepsilon |uS_x - vS_y|] - \frac{1}{\varepsilon^2} (1 + \varepsilon \mathcal{J} |\nabla S|) r_1, \\ (j_1)_t + \frac{1}{\varepsilon^2} u(r_1)_x - \frac{1}{\varepsilon^2} v(r_1)_y &= \frac{\rho}{2\varepsilon^2} (uS_x - vS_y) - \frac{1}{\varepsilon^2} (1 + \varepsilon \mathcal{J} |\nabla S|) j_1, \\ (r_2)_t + u(j_2)_x + v(j_2)_y &= \frac{\rho}{2\varepsilon^2} [2F(u, v) + \varepsilon |uS_x + vS_y|] - \frac{1}{\varepsilon^2} (1 + \varepsilon \mathcal{J} |\nabla S|) r_2, \\ (j_2)_t + \frac{1}{\varepsilon^2} u(r_2)_x + \frac{1}{\varepsilon^2} v(r_2)_y &= \frac{\rho}{2\varepsilon^2} (uS_x + vS_y) - \frac{1}{\varepsilon^2} (1 + \varepsilon \mathcal{J} |\nabla S|) j_2. \end{aligned} \quad (3.15)$$

Since the left-hand sides of the second and fourth equations in (3.15) include stiff terms with the $\frac{1}{\varepsilon^2}$ coefficients, we add and subtract $u(r_1)_x - v(r_1)_y$ and $u(r_2)_x + v(r_2)_y$ from the second and fourth equations, respectively, so that we finally obtain the following system for r_1, j_1, r_2 and j_2 :

$$\begin{aligned} (r_1)_t + u(j_1)_x - v(j_1)_y &= \frac{\rho}{2\varepsilon^2} (2F(u, v) + \varepsilon |uS_x - vS_y|) - \frac{1}{\varepsilon^2} (1 + \varepsilon \mathcal{J} |\nabla S|) r_1, \\ (j_1)_t + u(r_1)_x - v(r_1)_y &= \frac{\rho}{2\varepsilon^2} (uS_x - vS_y) - \frac{1}{\varepsilon^2} [(1 + \varepsilon \mathcal{J} |\nabla S|) j_1 + (1 - \varepsilon^2) u(r_1)_x - (1 - \varepsilon^2) v(r_1)_y], \\ (r_2)_t + u(j_2)_x + v(j_2)_y &= \frac{\rho}{2\varepsilon^2} (2F(u, v) + \varepsilon |uS_x + vS_y|) - \frac{1}{\varepsilon^2} (1 + \varepsilon \mathcal{J} |\nabla S|) r_2, \\ (j_2)_t + u(r_2)_x + v(r_2)_y &= \frac{\rho}{2\varepsilon^2} (uS_x + vS_y) - \frac{1}{\varepsilon^2} [(1 + \varepsilon \mathcal{J} |\nabla S|) j_2 + (1 - \varepsilon^2) u(r_2)_x + (1 - \varepsilon^2) v(r_2)_y], \end{aligned} \quad (3.16)$$

in which, all of the stiff terms are moved to the right-hand side.

3.3.2 Operator Splitting

In order to develop an efficient numerical method, we implement the operator splitting, in which the left-hand (non-stiff) and right-hand (stiff) sides of the system (3.16) are treated separately. To this end, we first introduce the vector $\mathbf{q} := (r_1, j_1, r_2, j_2)^T$ and write the system (3.16), (3.2) in the following form:

$$\begin{cases} \mathbf{q}_t + A_1 \mathbf{q}_x + A_2 \mathbf{q}_y = \mathcal{R}, \\ \tau S_t = \alpha \Delta S - \beta S + \gamma \rho, \end{cases} \quad (3.17)$$

where

$$A_1 = \begin{pmatrix} 0 & u & 0 & 0 \\ u & 0 & 0 & 0 \\ 0 & 0 & 0 & u \\ 0 & 0 & u & 0 \end{pmatrix}, \quad A_2 = \begin{pmatrix} 0 & -v & 0 & 0 \\ -v & 0 & 0 & 0 \\ 0 & 0 & 0 & v \\ 0 & 0 & v & 0 \end{pmatrix}, \quad (3.18)$$

and

$$\mathcal{R} = \begin{pmatrix} \frac{\rho}{2\varepsilon^2}(2F(u, v) + \varepsilon|uS_x - vS_y|) - \frac{1}{\varepsilon^2}(1 + \varepsilon \mathcal{J}|\nabla S|)r_1 \\ \frac{\rho}{2\varepsilon^2}(uS_x - vS_y) - \frac{1}{\varepsilon^2}[(1 + \varepsilon \mathcal{J}|\nabla S|)j_1 + (1 - \varepsilon^2)u(r_1)_x - (1 - \varepsilon^2)v(r_1)_y] \\ \frac{\rho}{2\varepsilon^2}(2F(u, v) + \varepsilon|uS_x + vS_y|) - \frac{1}{\varepsilon^2}(1 + \varepsilon \mathcal{J}|\nabla S|)r_2 \\ \frac{\rho}{2\varepsilon^2}(uS_x + vS_y) - \frac{1}{\varepsilon^2}[(1 + \varepsilon \mathcal{J}|\nabla S|)j_2 + (1 - \varepsilon^2)u(r_2)_x + (1 - \varepsilon^2)v(r_2)_y] \end{pmatrix}.$$

We then implement the splitting approach by considering the following two subsystems:

$$\begin{cases} \mathbf{q}_t = \mathcal{R}, \\ \tau S_t = 0, \end{cases} \quad (3.19)$$

$$\begin{cases} \mathbf{q}_t + A_1 \mathbf{q}_x + A_2 \mathbf{q}_y = \mathbf{0}, \\ \tau S_t = \alpha \Delta S - \beta S + \gamma \rho. \end{cases} \quad (3.20)$$

We note that in the subsystem (3.19), only the \mathbf{q} variable is evolved in time while S remains unchanged there.

Assuming that the solution at time t is available, we evolve it to the next time level using an operator splitting algorithm, [122, 123, 146], of either the first order:

$$\begin{pmatrix} \mathbf{q}(\mathbf{x}, t + \Delta t, \mathbf{v}) \\ S(\mathbf{x}, t + \Delta t) \end{pmatrix} \approx \mathcal{L}_2(\Delta t) \mathcal{L}_1(\Delta t) \begin{pmatrix} \mathbf{q}(\mathbf{x}, t, \mathbf{v}) \\ S(\mathbf{x}, t) \end{pmatrix}, \quad (3.21)$$

or the second-order:

$$\begin{pmatrix} \mathbf{q}(\mathbf{x}, t + \Delta t, \mathbf{v}) \\ S(\mathbf{x}, t + \Delta t) \end{pmatrix} \approx \mathcal{L}_1(\Delta t/2) \mathcal{L}_2(\Delta t) \mathcal{L}_1(\Delta t/2) \begin{pmatrix} \mathbf{q}(\mathbf{x}, t, \mathbf{v}) \\ S(\mathbf{x}, t) \end{pmatrix}. \quad (3.22)$$

Here, \mathcal{L}_1 and \mathcal{L}_2 stand for numerical solution operators for the stiff, (3.19), and non-stiff, (3.20), subsystems, respectively.

Remark 3.3.1 It should be observed that the order of the operators in (3.21) and (3.22) is interchangeable.

Remark 3.3.2 For simplicity of presentation, we will describe the numerical schemes used to solve each one of the subsystems (3.19) and (3.20) in the context of the first-order operator splitting (3.21). We also use the first-order splitting in the proof of the AP property of the proposed scheme. However, in all of the numerical experiments reported in §3.5, we implement the second-order operator splitting (3.22) to decrease the effect of splitting errors on the computed solutions.

Before proceeding with the description of numerical methods for the subsystems (3.19) and (3.20), we consider a computational domain, $\Omega \times V^+$, where $\Omega = [-L_x, L_x] \times [-L_y, L_y]$ and V^+ was introduced in the beginning of §3.3.1. The spatial domain Ω is partitioned into uniform Cartesian cells $C_{i,j} := [x_{i-\frac{1}{2}}, x_{i+\frac{1}{2}}] \times [y_{j-\frac{1}{2}}, y_{j+\frac{1}{2}}]$ of size $\Delta x \Delta y$ with the cell centers $(x_i, y_j) = (x_{i-\frac{1}{2}} + \Delta x/2, y_{j-\frac{1}{2}} + \Delta y/2)$; $i = 1, \dots, N_x$, $j = 1, \dots, N_y$. We also introduce a uniform grid in the velocity domain V^+ consisting of N_θ grid points:

$$\mathbf{v}_k = (v_0 \cos \theta_k, v_0 \sin \theta_k), \quad \theta_k = (k - 1/2)\Delta\theta, \quad \Delta\theta = \frac{\pi/2}{N_\theta}, \quad k = 1, \dots, N_\theta. \quad (3.23)$$

We also denote by $\rho_{i,j}^n \approx \rho(x_i, y_j, t^n)$, $S_{i,j}^n \approx S(x_i, y_j, t^n)$, $\mathbf{q}_{i,j,k}^n \approx \mathbf{q}(x_i, y_j, t^n, \mathbf{v}_k)$, and $F_k := F(\mathbf{v}_k)$.

3.3.2.1 \mathcal{L}_1 : Numerical Solution of the Stiff Subsystem (3.19)

In this section, we present a numerical scheme for the stiff subsystem (3.19). We start by solving the equations for r_1 and r_2 ,

$$\begin{aligned}(r_1)_t &= \frac{\rho}{2\varepsilon^2}(2F(u, v) + \varepsilon|uS_x - vS_y|) - \frac{1}{\varepsilon^2}(1 + \varepsilon\mathcal{J}|\nabla S|)r_1, \\ (r_2)_t &= \frac{\rho}{2\varepsilon^2}(2F(u, v) + \varepsilon|uS_x + vS_y|) - \frac{1}{\varepsilon^2}(1 + \varepsilon\mathcal{J}|\nabla S|)r_2,\end{aligned}\tag{3.24}$$

keeping in mind that the chemoattractant concentration S satisfies $\tau S_t = 0$.

It is instructive to point out that not only S , but also the macroscopic cell density ρ does not change in time during this substep. Indeed, from (3.14) and (3.24) we obtain

$$\begin{aligned}\rho_t &= 2 \int_{V^+} [r_1 + r_2] dv = \frac{\rho}{\varepsilon^2} \left[\int_{V^+} 4F(v) dv + \varepsilon \int_{V^+} (|uS_x - vS_y| + |uS_x + vS_y|) dv \right] \\ &\quad - \frac{2}{\varepsilon^2}(1 + \varepsilon\mathcal{J}|\nabla S|) \int_{V^+} [r_1 + r_2] dv = 0,\end{aligned}$$

which follows directly from (3.8) and the definition of \mathcal{J} in (3.10).

We assume that the numerical solution is available at time level $t = t^n$ and denote by

$$\begin{pmatrix} q_{i,j,k}^* \\ S_{i,j}^* \end{pmatrix} := \mathcal{L}_1(\Delta t) \begin{pmatrix} q_{i,j,k}^n \\ S_{i,j}^n \end{pmatrix}.\tag{3.25}$$

Taking into account that $\rho_{i,j}^* = \rho_{i,j}^n$ and $S_{i,j}^* = S_{i,j}^n$, we obtain the following semi-discrete approximations for $(r_1)_{i,j,k}^*$ and $(r_2)_{i,j,k}^*$ from (3.24):

$$\begin{aligned}\frac{d}{dt}(r_1)_{i,j,k}^* + \frac{1}{\varepsilon^2}(1 + \varepsilon\mathcal{J}|\nabla S_{i,j}^n|)(r_1)_{i,j,k}^* &= \frac{\rho_{i,j}^n}{2\varepsilon^2}(2F_k + \varepsilon|u_k(S_x)_{i,j}^n - v_k(S_y)_{i,j}^n|), \\ \frac{d}{dt}(r_2)_{i,j,k}^* + \frac{1}{\varepsilon^2}(1 + \varepsilon\mathcal{J}|\nabla S_{i,j}^n|)(r_2)_{i,j,k}^* &= \frac{\rho_{i,j}^n}{2\varepsilon^2}(2F_k + \varepsilon|u_k(S_x)_{i,j}^n + v_k(S_y)_{i,j}^n|).\end{aligned}\tag{3.26}$$

Here, we approximate the derivatives $(S_x)_{i,j}^n$ and $(S_y)_{i,j}^n$ with the central differences,

$$(S_x)_{i,j}^n = \frac{S_{i+1,j}^n - S_{i-1,j}^n}{2\Delta x}, \quad (S_y)_{i,j}^n = \frac{S_{i,j+1}^n - S_{i,j-1}^n}{2\Delta y},$$

and compute $|\nabla S_{i,j}^n| = \sqrt{((S_x)_{i,j}^n)^2 + ((S_y)_{i,j}^n)^2}$.

The linear ODEs in (3.26) are then solved exactly in time to obtain

$$\begin{aligned} (r_1)_{i,j,k}^* &= \eta_{i,j} (r_1)_{i,j,k}^n + \frac{1 - \eta_{i,j}}{1 + \varepsilon \mathcal{J} |\nabla S_{i,j}^n|} \left(F_k + \frac{\varepsilon}{2} |u_k(S_x)_{i,j}^n - v_k(S_y)_{i,j}^n| \right) \rho_{i,j}^n, \\ (r_2)_{i,j,k}^* &= \eta_{i,j} (r_2)_{i,j,k}^n + \frac{1 - \eta_{i,j}}{1 + \varepsilon \mathcal{J} |\nabla S_{i,j}^n|} \left(F_k + \frac{\varepsilon}{2} |u_k(S_x)_{i,j}^n + v_k(S_y)_{i,j}^n| \right) \rho_{i,j}^n, \end{aligned} \quad (3.27)$$

where

$$\eta_{i,j} = \exp \left\{ -\frac{\Delta t}{\varepsilon^2} (1 + \varepsilon \mathcal{J} |\nabla S_{i,j}^n|) \right\}.$$

We now solve the equations for j_1 and j_2 :

$$\begin{aligned} (j_1)_t &= \frac{\rho}{2\varepsilon^2} (uS_x - vS_y) - \frac{1}{\varepsilon^2} \left[(1 + \varepsilon \mathcal{J} |\nabla S|) j_1 + (1 - \varepsilon^2) u(r_1)_x - (1 - \varepsilon^2) v(r_1)_y \right], \\ (j_2)_t &= \frac{\rho}{2\varepsilon^2} (uS_x + vS_y) - \frac{1}{\varepsilon^2} \left[(1 + \varepsilon \mathcal{J} |\nabla S|) j_2 + (1 - \varepsilon^2) u(r_2)_x + (1 - \varepsilon^2) v(r_2)_y \right]. \end{aligned} \quad (3.28)$$

Equipped with the updated values of $(r_1)_{i,j,k}^*$ and $(r_2)_{i,j,k}^*$, we use the central differences to compute

$$\begin{aligned} ((r_m)_x)_{i,j,k}^* &= \frac{(r_m)_{i+1,j,k}^* - (r_m)_{i-1,j,k}^*}{2\Delta x}, \\ ((r_m)_y)_{i,j,k}^* &= \frac{(r_m)_{i,j+1,k}^* - (r_m)_{i,j-1,k}^*}{2\Delta y}, \quad m = 1, 2, \end{aligned} \quad (3.29)$$

substitute them into (3.28) and arrive at the following semi-discrete approximations for

$(j_1)_{i,j,k}^*$ and $(j_2)_{i,j,k}^*$:

$$\begin{aligned}
\frac{d}{dt}(j_1)_{i,j,k}^* + \frac{1}{\varepsilon^2}(1 + \varepsilon \mathcal{J} |\nabla S_{i,j}^*|)(j_1)_{i,j,k}^* = \\
-\frac{1}{\varepsilon^2} \left[(1 - \varepsilon^2) u_k((r_1)_x)_{i,j,k}^* - (1 - \varepsilon^2) v_k((r_1)_y)_{i,j,k}^* \right] + \frac{\rho_{i,j}^n}{2\varepsilon^2} \left[u_k(S_x)_{i,j}^n - v_k(S_y)_{i,j}^n \right], \\
\frac{d}{dt}(j_2)_{i,j,k}^* + \frac{1}{\varepsilon^2}(1 + \varepsilon \mathcal{J} |\nabla S_{i,j}^*|)(j_2)_{i,j,k}^* = \\
-\frac{1}{\varepsilon^2} \left[(1 - \varepsilon^2) u_k((r_2)_x)_{i,j,k}^* + (1 - \varepsilon^2) v_k((r_2)_y)_{i,j,k}^* \right] + \frac{\rho_{i,j}^n}{2\varepsilon^2} \left[u_k(S_x)_{i,j}^n + v_k(S_y)_{i,j}^n \right].
\end{aligned} \tag{3.30}$$

Finally, we solve the linear ODEs (3.30) exactly to obtain $(j_1)_{i,j,k}^*$ and $(j_2)_{i,j,k}^*$ (for the sake of brevity, we omit the precise formulae).

3.3.2.2 \mathcal{L}_2 : Numerical Solution of the Non-Stiff Subsystem (3.20)

In this section, we describe the numerical solution operator \mathcal{L}_2 and denote by

$$\begin{pmatrix} \mathbf{q}_{i,j,k}^{n+1} \\ S_{i,j}^{n+1} \end{pmatrix} := \mathcal{L}_2(\Delta t) \begin{pmatrix} \mathbf{q}_{i,j,k}^* \\ S_{i,j}^* \end{pmatrix} = \mathcal{L}_2(\Delta t) \mathcal{L}_1(\Delta t) \begin{pmatrix} \mathbf{q}_{i,j,k}^n \\ S_{i,j}^n \end{pmatrix}.$$

As one can see from (3.20), the linear hyperbolic system

$$\mathbf{q}_t + A_1 \mathbf{q}_x + A_2 \mathbf{q}_y = \mathbf{0} \tag{3.31}$$

with the constant coefficient matrices A_1 and A_2 given by (3.18) is, in fact, decoupled from the chemoattractant concentration equation. The latter is either the Poisson equation

$$\alpha \Delta S = \beta S - \gamma \rho, \tag{3.32}$$

if $\tau = 0$, or the parabolic equation

$$S_t = \alpha \Delta S - \beta S + \gamma \rho. \tag{3.33}$$

if $\tau = 1$. Therefore, we will first evolve the solution of (3.31) to obtain $\mathbf{q}_{i,j,k}^{n+1}$, from which the values of the macroscopic density $\rho_{i,j}^{n+1}$ will be calculated and used in either (3.32) or (3.33)

to compute $S_{i,j}^{n+1}$.

Upwind method for (3.31).

We begin with the derivation of a second-order semi-discrete upwind approximation for the system (3.31). To this end, we first introduce the matrix

$$Q = \begin{pmatrix} -1 & 1 & 0 & 0 \\ 1 & 1 & 0 & 0 \\ 0 & 0 & -1 & 1 \\ 0 & 0 & 1 & 1 \end{pmatrix},$$

which is used to simultaneously diagonalize the matrices A_1 and A_2 . We then define a change of variables $U := Q^{-1}q$ and rewrite the system (3.31) in the diagonal form:

$$U_t + B_1 U_x + B_2 U_y = 0, \quad (3.34)$$

where B_1 and B_2 are the following diagonal matrices:

$$B_1 := Q^{-1}A_1Q = \text{diag}(-u, u, -u, u), \quad B_2 := Q^{-1}A_2Q = \text{diag}(v, -v, -v, v).$$

Next, we split B_1 and B_2 into the sum of non-negative and non-positive definite matrices:

$$\begin{aligned} B_1 &= B_1^+ + B_1^-, \quad B_1^+ := \text{diag}(0, u, 0, u), \quad B_1^- := \text{diag}(-u, 0, -u, 0), \\ B_2 &= B_2^+ + B_2^-, \quad B_2^+ := \text{diag}(v, 0, 0, v), \quad B_2^- := \text{diag}(0, -v, -v, 0), \end{aligned}$$

and rearrange (3.34) in an equivalent form:

$$U_t + B_1^+ U_x + B_1^- U_x + B_2^+ U_y + B_2^- U_y = 0.$$

Multiplying the last equation by Q , we recover the original system (3.31):

$$q_t + A_1^+ q_x + A_1^- q_x + A_2^+ q_y + A_2^- q_y = 0, \quad (3.35)$$

where

$$A_1^+ := QB_1^+Q^{-1} = \frac{1}{2} \begin{pmatrix} u & u & 0 & 0 \\ u & u & 0 & 0 \\ 0 & 0 & u & u \\ 0 & 0 & u & u \end{pmatrix}, \quad A_1^- := QB_1^-Q^{-1} = \frac{1}{2} \begin{pmatrix} -u & u & 0 & 0 \\ u & -u & 0 & 0 \\ 0 & 0 & -u & u \\ 0 & 0 & u & -u \end{pmatrix},$$

$$A_2^+ := QB_2^+Q^{-1} = \frac{1}{2} \begin{pmatrix} v & -v & 0 & 0 \\ -v & v & 0 & 0 \\ 0 & 0 & v & v \\ 0 & 0 & v & v \end{pmatrix}, \quad A_2^- := QB_2^-Q^{-1} = \frac{1}{2} \begin{pmatrix} -v & -v & 0 & 0 \\ -v & -v & 0 & 0 \\ 0 & 0 & -v & v \\ 0 & 0 & v & -v \end{pmatrix}.$$

We note that A_1^+ and A_2^+ are non-negative definite, while A_1^- and A_2^- are non-positive definite so that and one can easily design upwind finite-difference schemes for the system (3.35). According to the upwind approach, we introduce the second-order forward and backward finite-difference approximations for the spatial derivatives in (3.35):

$$(q_x^+)_{i,j,k} = \frac{-q_{i+2,j,k} + 4q_{i+1,j,k} - 3q_{i,j,k}}{2\Delta x}, \quad (q_x^-)_{i,j,k} = \frac{3q_{i,j,k} - 4q_{i-1,j,k} + q_{i-2,j,k}}{2\Delta x},$$

$$(q_y^+)_{i,j,k} = \frac{-q_{i,j+2,k} + 4q_{i,j+1,k} - 3q_{i,j,k}}{2\Delta y}, \quad (q_y^-)_{i,j,k} = \frac{3q_{i,j,k} - 4q_{i,j-1,k} + q_{i,j-2,k}}{2\Delta y},$$

which are then used to construct the following second-order semi-discrete upwind scheme for (3.31):

$$\frac{d}{dt} \mathbf{q}_{i,j,k} = -A_1^+(\mathbf{q}_x^-)_{i,j,k} - A_1^-(\mathbf{q}_x^+)_{i,j,k} - A_2^+(\mathbf{q}_y^-)_{i,j,k} - A_2^-(\mathbf{q}_y^+)_{i,j,k}. \quad (3.36)$$

The system of time dependent ODEs (3.36) should be numerically integrated in time using a stable and sufficiently accurate ODE solver. For example, using the first-order forward Euler method, a fully discretization of (3.36) can be written in the flux form as follows:

$$\mathbf{q}_{i,j,k}^{n+1} = \mathbf{q}_{i,j,k}^* - \frac{\Delta t}{\Delta x} (\mathbf{H}_{i+\frac{1}{2},j,k} - \mathbf{H}_{i-\frac{1}{2},j,k}) - \frac{\Delta t}{\Delta y} (\mathbf{G}_{i,j+\frac{1}{2},k} - \mathbf{G}_{i,j-\frac{1}{2},k}), \quad (3.37)$$

where

$$\begin{aligned} H_{i+\frac{1}{2},j,k} &= A_1^+ \frac{3q_{i,j,k}^* - q_{i-1,j,k}^*}{2} + A_1^- \frac{3q_{i+1,j,k}^* - q_{i+2,j,k}^*}{2}, \\ G_{i,j+\frac{1}{2},k} &= A_2^+ \frac{3q_{i,j,k}^* - q_{i,j-1,k}^*}{2} + A_2^- \frac{3q_{i,j+1,k}^* - q_{i,j+2,k}^*}{2}. \end{aligned} \quad (3.38)$$

It is important to stress that according to the definitions in (3.12), both r_1 and r_2 (and hence ρ , see (3.14)) should be positive, which is not guaranteed unless the scheme (3.37), (3.38) is used with a very small (possibly impractical) timestep Δt . We therefore implement a draining timestep technique, which was introduced in [12]. To this end, we denote by

$$(\Delta t_{i,j,k}^{\text{dr}})^{(m)} := \frac{\Delta x \Delta y (r_m^*)_{i,j,k}}{\Delta y [(H_{i+\frac{1}{2},j,k}^{(m)})_+ + (-H_{i-\frac{1}{2},j,k}^{(m)})_+] + \Delta x [\max(G_{i,j+\frac{1}{2},k}^{(m)})_+ + (-G_{i,j-\frac{1}{2},k}^{(m)})_+] + \delta},$$

where $m = 1, 2$. We then replace the first ($m = 1$) and third ($m = 2$) equations in (3.37) with

$$(r_m)_{i,j,k}^{n+1} = (r_m^*)_{i,j,k} - \frac{\Delta t_{i+\frac{1}{2},j,k}^{(m)} H_{i+\frac{1}{2},j,k}^{(m)} - \Delta t_{i-\frac{1}{2},j,k}^{(m)} H_{i-\frac{1}{2},j,k}^{(m)}}{\Delta x} - \frac{\Delta t_{i,j+\frac{1}{2},k}^{(m)} G_{i,j+\frac{1}{2},k}^{(m)} - \Delta t_{i,j-\frac{1}{2},k}^{(m)} G_{i,j-\frac{1}{2},k}^{(m)}}{\Delta y},$$

where

$$\begin{aligned} \Delta t_{i+\frac{1}{2},j,k}^{(m)} &= \min(\Delta t, (\Delta t_{i,j,k}^{\text{dr}})^{(m)}), \quad I = i + \frac{1}{2} - \frac{\text{sgn}(H_{i+\frac{1}{2},j,k}^{(m)})}{2}, \\ \Delta t_{i,j+\frac{1}{2},k}^{(m)} &= \min(\Delta t, (\Delta t_{i,j,k}^{\text{dr}})^{(m)}), \quad J = j + \frac{1}{2} - \frac{\text{sgn}(G_{i,j+\frac{1}{2},k}^{(m)})}{2}. \end{aligned} \quad (3.39)$$

It can be easily verified that now $(r_1)_{i,j,k}^{n+1} \geq 0$ and $(r_3)_{i,j,k}^{n+1} \geq 0$, and thus $\rho_{i,j}^{n+1}$, which is computed from (3.14) using the midpoint rule, is non-negative, namely,

$$\rho_{i,j}^{n+1} = 2\nu_0 \sum_{k=1}^{N_\theta} [(r_1)_{i,j,k}^{n+1} + (r_2)_{i,j,k}^{n+1}] \Delta \theta \geq 0, \quad \forall i, j. \quad (3.40)$$

Remark 3.3.3 Even though, we show here only one forward Euler step, in all of our computations below, we solve the semi-discrete system (3.36) using the three-stage third-order SSP Runge-Kutta method: see, e.g., [58, 60, 144] and Appendix A.1. Since SSP methods consist of a convex combination of forward Euler steps, the computed values of $(r_1)_{i,j,k}^{n+1}$ and $(r_2)_{i,j,k}^{n+1}$,

as well as $\rho_{i,j}^{n+1}$, are still guaranteed to be non-negative.

Spectral methods for (3.32) and (3.33).

Equipped with the point values of the macroscopic density, $\rho_{i,j}^{n+1}$ at time level $t = t^{n+1}$, we implement the spectral method to update the values of the chemoattractant concentration S . To this end, we remind the reader that the Neumann boundary conditions are imposed for both S and ρ . Therefore, the discrete Fourier coefficients $\widehat{S}_{\ell,m}(t)$ and $\widehat{\rho}_{\ell,m}(t)$ can be computed from the available point values $S_{i,j}(t)$ and $\rho_{i,j}(t)$, respectively, using the fast cosine Fourier transform and the solution at time t can be approximated by

$$\begin{aligned} S(x, y, t) &\approx \sum_{\ell,m} \widehat{S}_{\ell,m}(t) \cos\left(\frac{\pi \ell x}{L_x}\right) \cos\left(\frac{\pi m y}{L_y}\right), \\ \rho(x, y, t) &\approx \sum_{\ell,m} \widehat{\rho}_{\ell,m}(t) \cos\left(\frac{\pi \ell x}{L_x}\right) \cos\left(\frac{\pi m y}{L_y}\right). \end{aligned} \quad (3.41)$$

Substituting (3.41) into (3.2) yields

$$\tau \frac{d}{dt} \widehat{S}_{\ell,m}(t) + \omega_{\ell,m} \widehat{S}_{\ell,m}(t) = \gamma \widehat{\rho}_{\ell,m}(t), \quad \omega_{\ell,m} := \alpha(\ell^2 + m^2) + \beta. \quad (3.42)$$

In the elliptic ($\tau = 0$) case, the values $\widehat{S}_{\ell,m}^{n+1}$ are immediately computed from

$$\widehat{S}_{\ell,m}^{n+1} = \frac{\gamma}{\omega_{\ell,m}} \widehat{\rho}_{\ell,m}^{n+1}. \quad (3.43)$$

In the parabolic ($\tau \neq 0$) case, equation (3.42) can be solved exactly on the interval $[t^n, t^{n+1}]$:

$$\widehat{S}_{\ell,m}^{n+1} = e^{-\omega_{\ell,m} \Delta t} \widehat{S}_{\ell,m}^n + \gamma \int_{t^n}^{t^{n+1}} \widehat{\rho}_{\ell,m}(s) e^{-\omega_{\ell,m}(s-t^n-\Delta t)} ds.$$

We then approximate the integral in the last equation using the trapezoidal rule to obtain

$$\widehat{S}_{\ell,m}^{n+1} = e^{-\omega_{\ell,m} \Delta t} \widehat{S}_{\ell,m}^n + \frac{\gamma \Delta t}{2} [\widehat{\rho}_{\ell,m}^n + e^{-\omega_{\ell,m} \Delta t} \widehat{\rho}_{\ell,m}^{n+1}]. \quad (3.44)$$

Finally, we use the inverse fast cosine Fourier transform to compute the point values $\{S_{i,j}^{n+1}\}$ out of the set of the discrete Fourier coefficients $\{\widehat{S}_{\ell,m}^{n+1}\}$.

3.4 AP Property

As was mentioned in the Introduction §3.1, the solutions of the studied kinetic-chemotaxis model are expected to converge to the corresponding solutions of PKS system as $\varepsilon \rightarrow 0$. In this section, we show that the proposed numerical scheme for (3.10), (3.2) provides a consistent discretization of (3.1), (3.2) in the limiting $\varepsilon \rightarrow 0$ case. In other words, the numerical method is AP. For the simplicity of the presentation, we prove the AP property for the first-order splitting (3.21) and note that a straightforward extension to the second-order splitting (3.22) can be derived.

We first observe that when $\varepsilon \rightarrow 0$ the equations in (3.27) reduce to

$$(r_1)_{i,j,k}^* = \rho_{i,j}^n F_k, \quad (r_2)_{i,j,k}^* = \rho_{i,j}^n F_k. \quad (3.45)$$

We then substitute (3.45) into (3.30) and derive the following formulae in the $\varepsilon \rightarrow 0$ limit:

$$\begin{aligned} (j_1)_{i,j,k}^* &= \frac{\rho_{i,j}^n}{2} [u_k(S_x)_{i,j}^n - v_k(S_y)_{i,j}^n] - u_k F_k(\rho_x)_{i,j}^n + v_k F_k(\rho_y)_{i,j}^n, \\ (j_2)_{i,j,k}^* &= \frac{\rho_{i,j}^n}{2} [u_k(S_x)_{i,j}^n + v_k(S_y)_{i,j}^n] - u_k F_k(\rho_x)_{i,j}^n - v_k F_k(\rho_y)_{i,j}^n, \end{aligned} \quad (3.46)$$

where $(\rho_x)_{i,j}^n$ and $(\rho_y)_{i,j}^n$ are obtained from (3.29) and (3.40) and equal to

$$(\rho_x)_{i,j}^n = \frac{\rho_{i+1,j}^n - \rho_{i-1,j}^n}{2\Delta x}, \quad (\rho_y)_{i,j}^n = \frac{\rho_{i,j+1}^n - \rho_{i,j-1}^n}{2\Delta y}.$$

Next, we consider the first and third equations in the semi-discrete upwind scheme

(3.36), which after the forward Euler time discretization read as

$$\begin{aligned}
\frac{(r_1)_{i,j,k}^{n+1} - (r_1)_{i,j,k}^*}{\Delta t} &= -\frac{1}{2} \left[u_k((r_1)_x^-)_{i,j,k}^* + u_k((j_1)_x^-)_{i,j,k}^* - u_k((r_1)_x^+)_{i,j,k}^* + u_k((j_1)_x^+)_{i,j,k}^* \right. \\
&\quad \left. + v_k((r_1)_y^-)_{i,j,k}^* - v_k((j_1)_y^-)_{i,j,k}^* - v_k((r_1)_y^+)_{i,j,k}^* - v_k((j_1)_y^+)_{i,j,k}^* \right], \\
\frac{(r_2)_{i,j,k}^{n+1} - (r_2)_{i,j,k}^*}{\Delta t} &= -\frac{1}{2} \left[u_k((r_2)_x^-)_{i,j,k}^* + u_k((j_2)_x^-)_{i,j,k}^* - u_k((r_2)_x^+)_{i,j,k}^* + u_k((j_2)_x^+)_{i,j,k}^* \right. \\
&\quad \left. + v_k((r_2)_y^-)_{i,j,k}^* + v_k((j_2)_y^-)_{i,j,k}^* - v_k((r_2)_y^+)_{i,j,k}^* + v_k((j_2)_y^+)_{i,j,k}^* \right].
\end{aligned} \tag{3.47}$$

Substituting (3.45) and (3.46) into (3.47), adding the above two equations and multiplying by 2 yield

$$\begin{aligned}
2[(r_1)_{i,j,k}^{n+1} + (r_2)_{i,j,k}^{n+1}] &= 4\rho_{i,j}^n F_k - \Delta t \left[(\Delta x)^3 (\rho_{xxx})_{i,j}^n u_k F_k + (\Delta y)^3 (\rho_{yyy})_{i,j}^n v_k F_k \right. \\
&\quad \left. + 2((\rho S_x)_x)_{i,j}^n u_k^2 + 2(\rho S_y)_y)_{i,j}^n v_k^2 - 4(\rho_{xx})_{i,j}^n u_k^2 F_k - 4(\rho_{yy})_{i,j}^n v_k^2 F_k \right],
\end{aligned} \tag{3.48}$$

where we have used the following notations:

$$\begin{aligned}
(\rho_{xx})_{i,j}^n &:= \frac{-\rho_{i+3,j}^n + 4\rho_{i+2,j}^n + \rho_{i+1,j}^n - 8\rho_{i,j}^n + \rho_{i-1,j}^n + 4\rho_{i-2,j}^n - \rho_{i-3,j}^n}{8(\Delta x)^2}, \\
(\rho_{yy})_{i,j}^n &:= \frac{-\rho_{i,j+3}^n + 4\rho_{i,j+2}^n + \rho_{i,j+1}^n - 8\rho_{i,j}^n + \rho_{i,j-1}^n + 4\rho_{i,j-2}^n - \rho_{i,j-3}^n}{8(\Delta y)^2}, \\
(\rho_{xxx})_{i,j}^n &:= \frac{\rho_{i+2,j}^n - 4\rho_{i+1,j}^n + 6\rho_{i,j}^n - 4\rho_{i-1,j}^n + \rho_{i-2,j}^n}{(\Delta x)^4}, \\
(\rho_{yyy})_{i,j}^n &:= \frac{\rho_{i,j+2}^n - 4\rho_{i,j+1}^n + 6\rho_{i,j}^n - 4\rho_{i,j-1}^n + \rho_{i,j-2}^n}{(\Delta y)^4}, \\
((\rho S_x)_x)_{i,j}^n &:= \frac{1}{8(\Delta x)^2} \left[-\rho_{i+2,j}^n (S_{i+3,j}^n - S_{i+1,j}^n) + 4\rho_{i+1,j}^n (S_{i+2,j}^n - S_{i,j}^n) \right. \\
&\quad \left. - 4\rho_{i-1,j}^n (S_{i,j}^n - S_{i-2,j}^n) + \rho_{i-2,j}^n (S_{i-2,j}^n - S_{i-3,j}^n) \right], \\
((\rho S_y)_y)_{i,j}^n &:= \frac{1}{8(\Delta y)^2} \left[-\rho_{i,j+2}^n (S_{i,j+3}^n - S_{i,j+1}^n) + 4\rho_{i,j+1}^n (S_{i,j+2}^n - S_{i,j}^n) \right. \\
&\quad \left. - 4\rho_{i,j-1}^n (S_{i,j}^n - S_{i,j-2}^n) + \rho_{i,j-2}^n (S_{i,j-2}^n - S_{i,j-3}^n) \right].
\end{aligned}$$

We now multiply (3.48) by $v_0 \Delta \theta$, sum it over all k , and use (3.40) to obtain

$$\begin{aligned}
\rho_{i,j}^{n+1} &= \rho_{i,j}^n v_0 \sum_{k=1}^{N_\theta} 4F_k \Delta \theta \\
&\quad - v_0 \Delta t \left[(\Delta x)^3 (\rho_{xxxx})_{i,j}^n \sum_{k=1}^{N_\theta} u_k F_k \Delta \theta + (\Delta y)^3 (\rho_{yyyy})_{i,j}^n \sum_{k=1}^{N_\theta} v_k F_k \Delta \theta \right. \\
&\quad \left. + 2((\rho S_x)_x)_{i,j}^n \sum_{k=1}^{N_\theta} u_k^2 \Delta \theta + 2((\rho S_y)_y)_{i,j}^n \sum_{k=1}^{N_\theta} v_k^2 \Delta \theta \right. \\
&\quad \left. - 4(\rho_{xx})_{i,j}^n \sum_{k=1}^{N_\theta} u_k^2 F_k \Delta \theta - 4(\rho_{yy})_{i,j}^n \sum_{k=1}^{N_\theta} v_k^2 F_k \Delta \theta \right].
\end{aligned} \tag{3.49}$$

We finally use (3.8), (3.23), and the approximation property of the midpoint rule to establish the following estimates and identities:

$$\begin{aligned}
v_0 \sum_{k=1}^{N_\theta} 4F_k \Delta \theta &= 1 + \mathcal{O}((\Delta \theta)^2), \\
v_0 \sum_{k=1}^{N_\theta} u_k F_k \Delta \theta &\leq \frac{v_0^2}{4} + \mathcal{O}((\Delta \theta)^2), \quad v_0 \sum_{k=1}^{N_\theta} v_k F_k \Delta \theta \leq \frac{v_0^2}{4} + \mathcal{O}((\Delta \theta)^2), \\
2v_0 \sum_{k=1}^{N_\theta} u_k^2 \Delta \theta &= 2v_0 \sum_{k=1}^{N_\theta} v_k^2 \Delta \theta = v_0 \sum_{k=1}^{N_\theta} (u_k^2 + v_k^2) \Delta \theta = \sum_{k=1}^{N_\theta} v_0^4 \Delta \theta \approx \chi, \\
4v_0 \sum_{k=1}^{N_\theta} u_k^2 F_k \Delta \theta &= 4v_0 \sum_{k=1}^{N_\theta} v_k^2 F_k \Delta \theta = 2v_0 \sum_{k=1}^{N_\theta} (u_k^2 + v_k^2) F_k \Delta \theta = 2 \sum_{k=1}^{N_\theta} v_0^4 F_k \Delta \theta \approx D,
\end{aligned}$$

which can be used to show that (3.49) provides a consistent approximation of (3.1).

3.5 Numerical Results

In this section, we test the proposed AP scheme on several numerical examples and also study the behavior of the solutions of the kinetic-chemotaxis system (3.10), (3.2) in the $\varepsilon \rightarrow 0$ regime. In all of the examples below, we take $v_0 = 1$ and $N_\theta = 32$. The parameter $\varepsilon = 1$ in Example 1 and $\varepsilon = 10^{-5}$ in all other examples.

Example 3.1—Parabolic-Elliptic System

In this example taken from [23], we consider the system (3.10), (3.2) in the parabolic-elliptic ($\tau = 0$) and non-stiff ($\varepsilon = 1$) regime with $\alpha = \gamma = 1$, $\beta = 0$, and $F(v) \equiv 1/(2\pi)$. The system is solved on the domain $\Omega = [-2, 2] \times [-2, 2]$ and subject to the following Gaussian-shaped initial data:

$$f(x, y, 0, v) = \frac{1}{2\pi} \rho(x, y, 0), \quad \rho(x, y, 0) = \frac{15M}{\pi} e^{-15(x^2+y^2)},$$

where M is a total mass.

According to the theoretical results in [15], there are two critical mass thresholds: if $M > M_c = 8$, the solution blows up in finite time, while if $M < m_c = 0.403$, a global classical solution exists. It is still, however, unclear whether the solution remains bounded if $m_c \leq M \leq M_c$.

We investigate the solution behavior by computing the ratio $\|\rho\|_\infty/M$ for different values of M . We run the computations on a uniform grid with $N_x = N_y = 128$ until final time $T = 6$. The results are presented in Figure 3.1 for $M = 1, 5, 7, 8$ and 9. As one can see, when $M = 1$ the maximum density decays for all times while for other values of M the solution exhibits an initial growth. For $M = 5$ and $M = 7$, the maximum density decays at later times and the solution clearly remains bounded. At the same time, for $M = 9$, which is above the critical threshold $M_c = 8$, the maximum density increases and eventually saturates. In fact, this solution blows up and its maximum saturation phenomenon is attributed to the fact that the magnitude of finite-difference approximations of δ -type singularities is always proportional to $1/(\Delta x \Delta y)$. The blowup is also confirmed by the data presented in the Figure 3.2 (right), where we plot the time evolution of $\|\rho\|_\infty$ computed on three consecutive meshes: as one can see, at time $T = 6$ the value of $\|\rho\|_\infty$ increases by a factor of four as the grid is refined. This behavior of $\|\rho\|_\infty$ is clearly different from the one observed in the case of $M = 7 < M_c$ shown in Figure 3.2 (left).

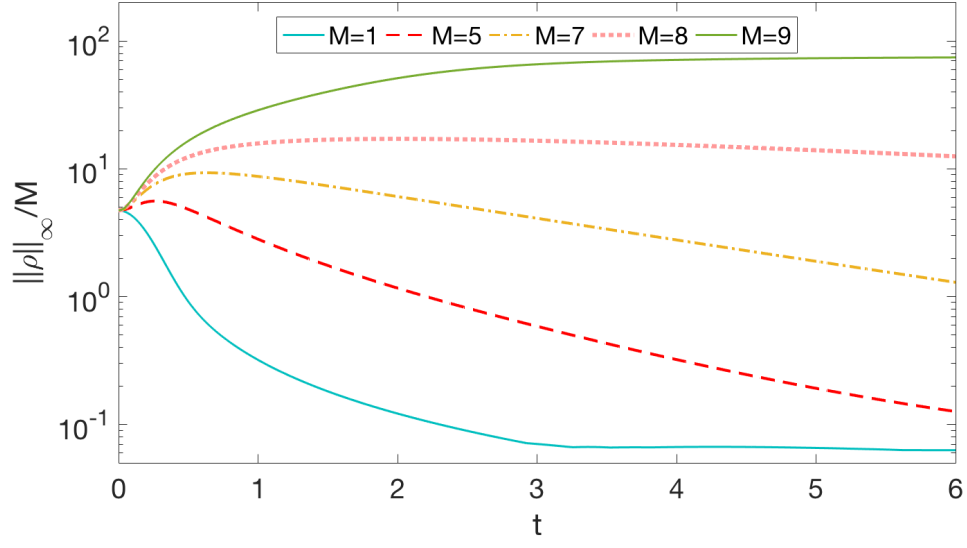


Figure 3.1 Example 3.1: Behavior of $\|\rho\|_\infty/M$ in time for varying values of M ; $N_x = N_y = 128$.

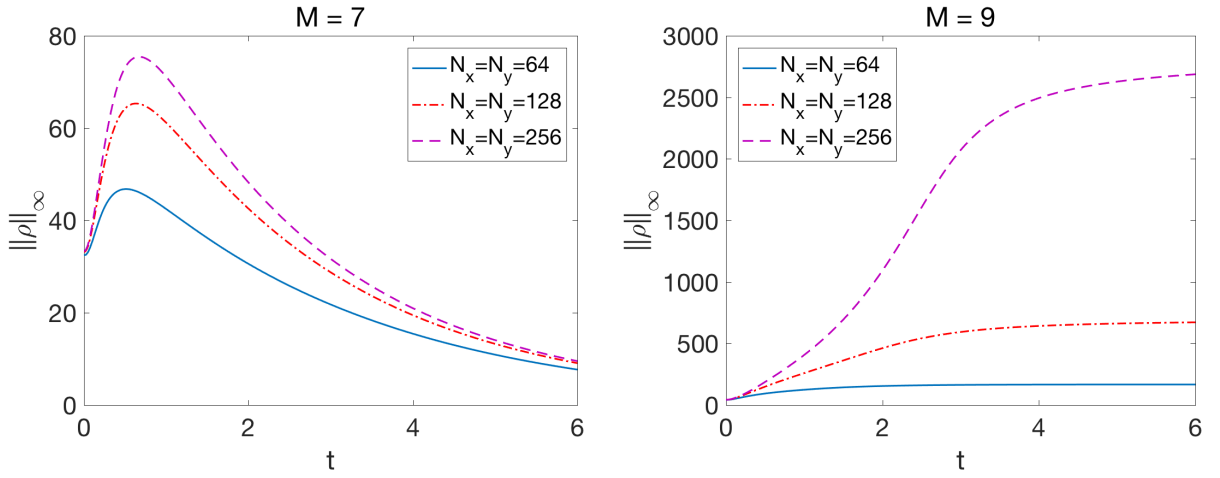


Figure 3.2 Example 3.1: Behavior of $\|\rho\|_\infty$ in time for $M = 7$ (left) and $M = 9$ (right) on three consecutive meshes.

Example 3.2—Parabolic-Parabolic System: Blowup at the Center

In this example, we consider the system (3.10), (3.2) in the parabolic-parabolic ($\tau = 1$) and stiff ($\varepsilon \ll 1$) regime with $\alpha = \beta = \gamma = 1$, and $F(v) \equiv 1/(2\pi)$. The system is solved on the domain $\Omega = [-1/2, 1/2] \times [-1/2, 1/2]$ and subject to the following initial data:

$$f(x, y, 0, v) = \frac{1}{2\pi} \rho(x, y, 0), \quad \rho(x, y, 0) = \frac{100M}{\pi} e^{-100(x^2+y^2)}, \quad (3.50)$$

where M is a total mass.

Example 3.2a.

We first consider the case when the initial chemoattractant concentration is a Gaussian-shaped function given by

$$S(x, y, 0) = 500e^{-50(x^2+y^2)}. \quad (3.51)$$

We study the time evolution of maximum density for three different values of the initial mass, $M = 1, 8$ and 11 . In Figure 3.3, we plot $\|\rho\|_\infty$ as a function of time for four consecutive meshes. We conclude that the behavior of the solution depends on the total mass: if M is large enough, the maximum norm of the cell density grows rapidly and saturates after blowup due to the finite-difference approximation limitation as discussed in Example 1. However, for smaller M , the maximum density first increases and then decreases without blowing up.

The blowup phenomenon is illustrated in Figure 3.4, where we plot the computed density at the post-blowup time $T = 5 \times 10^{-4}$ for $M = 11$ on two different grids with $N_x = N_y = 128$ (left) and $N_x = N_y = 256$ (right).

Example 3.2b.

We then consider the same initial boundary value problem with zero initial chemoattractant:

$$S(x, y, 0) = 0. \quad (3.52)$$

In this case, the spiky structure at the center of the computational domain develops

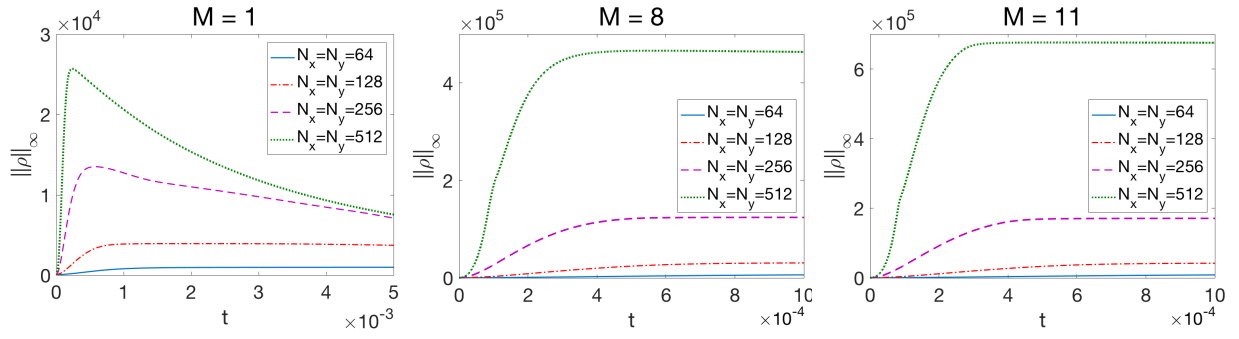


Figure 3.3 Example 3.2a: Behavior of $\|\rho\|_\infty$ in time for $M = 1$ (left), $M = 8$ (middle) and $M = 11$ (right) on four consecutive meshes.

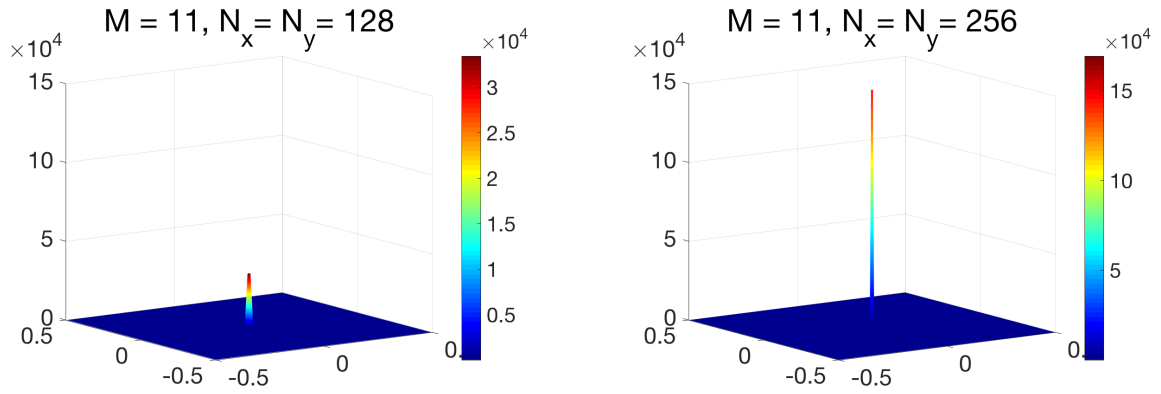


Figure 3.4 Example 3.2a: The density $\rho(x, y, T = 0.0005)$ for $M = 11$ computed on the meshes with: $N_x = N_y = 128$ (left) and $N_x = N_y = 256$ (right).

much slower than in Example 2a, since S is not concentrated at the center initially. This seems to affect the value of the critical mass. For instance, when $M = 8$, the solution does not blow up in contrast to Example 2a; see Figure 3.5 (left), where we plot $\|\rho\|_\infty$ as a function of time for three consecutive meshes. When larger values of M are considered, the solution blows up as expected; see Figure 3.5. It should be pointed out, however, that one can observe rapid change in the solution magnitudes for both $M = 9.5$ and $M = 11$, but these changes occur after the blowup times. The latter can be estimated as $t = 0.24$ (for $M = 9.5$) and $t = 0.058$ (for $M = 11$), since of these times the ratio of $\|\rho\|_\infty$ computed on the 256×256 and 128×128 grids becomes 4.

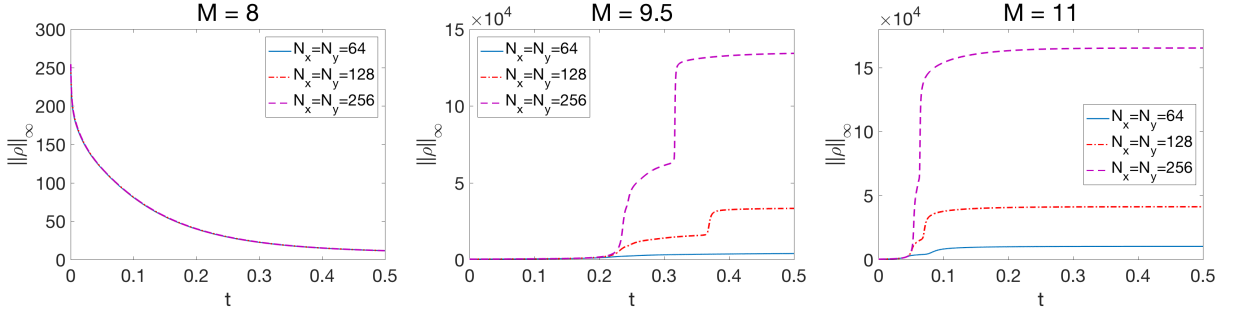


Figure 3.5 Example 3.2b: Behavior of $\|\rho\|_\infty$ in time for $M = 8$ (left), $M = 9.5$ (middle) and $M = 11$ (right) on three consecutive meshes.

We conclude this example with a self-convergence study. To this end, we take a small final time $T = 0.01$ and measure the experimental convergence rate for the density in the L^∞ -norm by computing

$$\text{rate}_{4N} = \log_2 \left(\frac{\|e_{2N}\|_\infty}{\|e_{4N}\|_\infty} \right),$$

where $\|e_{2N}\|_\infty := \frac{\|\rho_N - \rho_{2N}\|_\infty}{\max\{\rho_{2N}\}}$ is the estimated relative L^∞ -error, and ρ_N is the solution computed on a mesh with $N = N_x = N_y$.

The results presented in Table 3.1 clearly demonstrate the second order of accuracy of the proposed AP scheme.

Table 3.1 Example 3.2b: L^∞ - errors for $M = 8, 9.5$ and 11 (from left to right).

	$M = 8$		$M = 9.5$		$M = 11$	
N	$\ e_{2N}\ _\infty$	rate $_{4N}$	$\ e_{2N}\ _\infty$	rate $_{4N}$	$\ e_{2N}\ _\infty$	rate $_{4N}$
32	1.5680E-02	-	2.9056E-02	-	4.9613E-02	-
64	3.2150E-03	2.2860	8.1861E-03	1.8276	1.6752E-02	1.5663
128	8.4486E-04	1.9280	2.1204E-03	1.9488	4.5867E-03	1.8688
256	2.0985E-04	2.0093	5.3892E-04	1.9761	1.1662E-03	1.9756

Example 3.3—Parabolic-Parabolic System: Blowup at the Corner

In our last example, we study the model (3.10), (3.2) in the parabolic-parabolic ($\tau = 1$) and stiff ($\varepsilon \ll 1$) regime with $\alpha = \beta = \gamma = 1$, and $F(v) \equiv 1/(2\pi)$. The system is solved on the domain $\Omega = [-1/2, 1/2] \times [-1/2, 1/2]$ and subject to the same initial data as in Example 2b, but shifted by $(0.25, 0.25)$ from the center of the domain:

$$f(x, y, 0, v) = \frac{1}{2\pi} \rho(x, y, 0), \quad \rho(x, y, 0) = \frac{100M}{\pi} e^{-100((x-0.25)^2 + (y-0.25)^2)}, \quad S(x, y, 0) = 0, \quad (3.53)$$

where M stands for a total mass.

According to the analytical results in [65] and the numerical simulations in [31], the solution of the PKS model with the corresponding initial and boundary conditions moves towards the upper right corner of the computational domain and blows up there. In view of these results, it is interesting to numerically investigate whether the solution of the kinetic chemotaxis model behaves similarly.

In Figures 3.6 - 3.8, we plot the density computed on the uniform grid with $N_x = N_y = 128$ for $M = 3, 7$ and 11 . The time evolution is shown on each of these figures (from left to right). As one can see, in all of the cases, even when $M = 3$, the solution blows up though the blowup time is much smaller for larger values of M . One can also clearly see that the solutions propagate towards the upper corner of the computational domain. However, when $M = 11$, the solution blows up much earlier than it would reach the corner. We have also performed the same numerical experiments with $\varepsilon = 10^{-8}$ and the obtained results were very similar. This indicated that for larger initial masses the solutions of the kinetic chemotaxis model may not converge to the corresponding PKS solution.

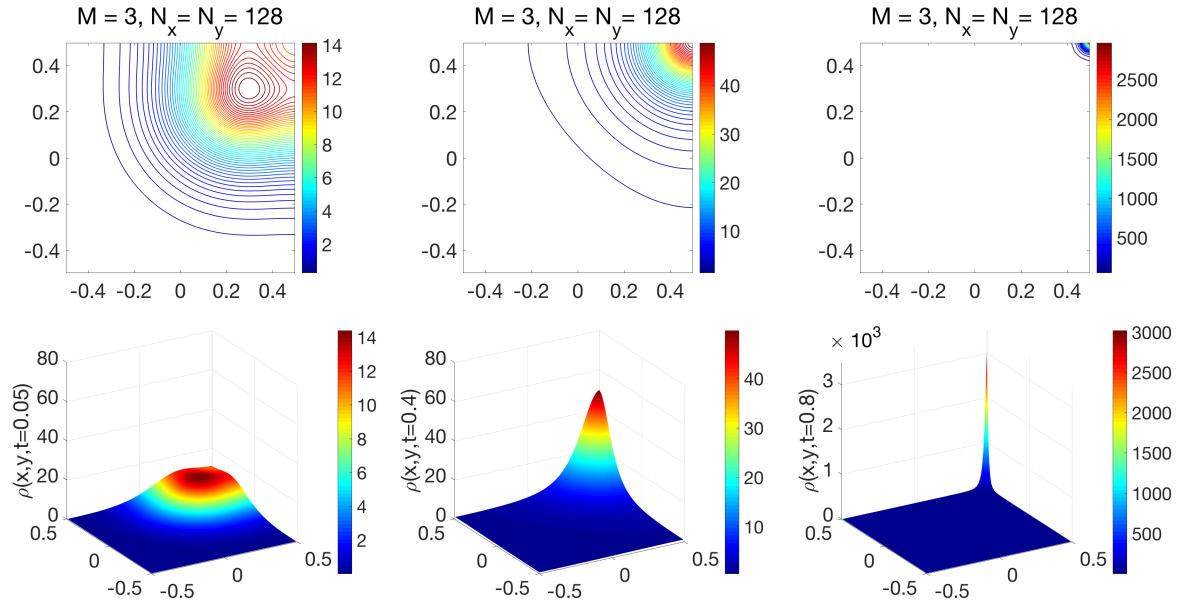


Figure 3.6 Example 3.3: The displacement of the density for $M = 3$.

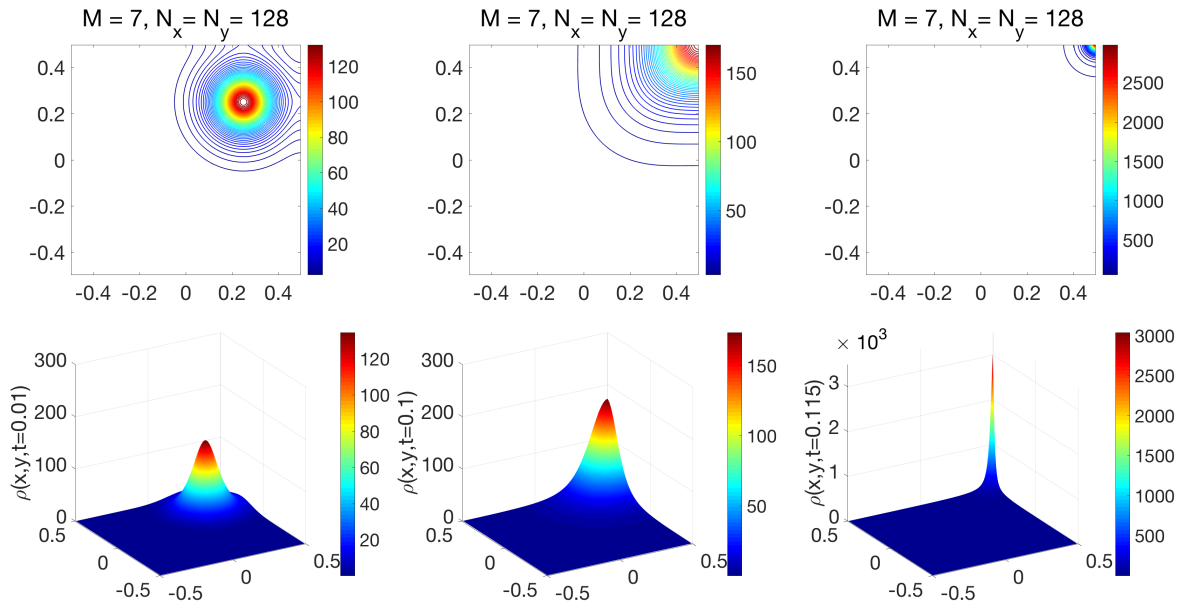


Figure 3.7 Example 3.3: The displacement of the density for $M = 7$.

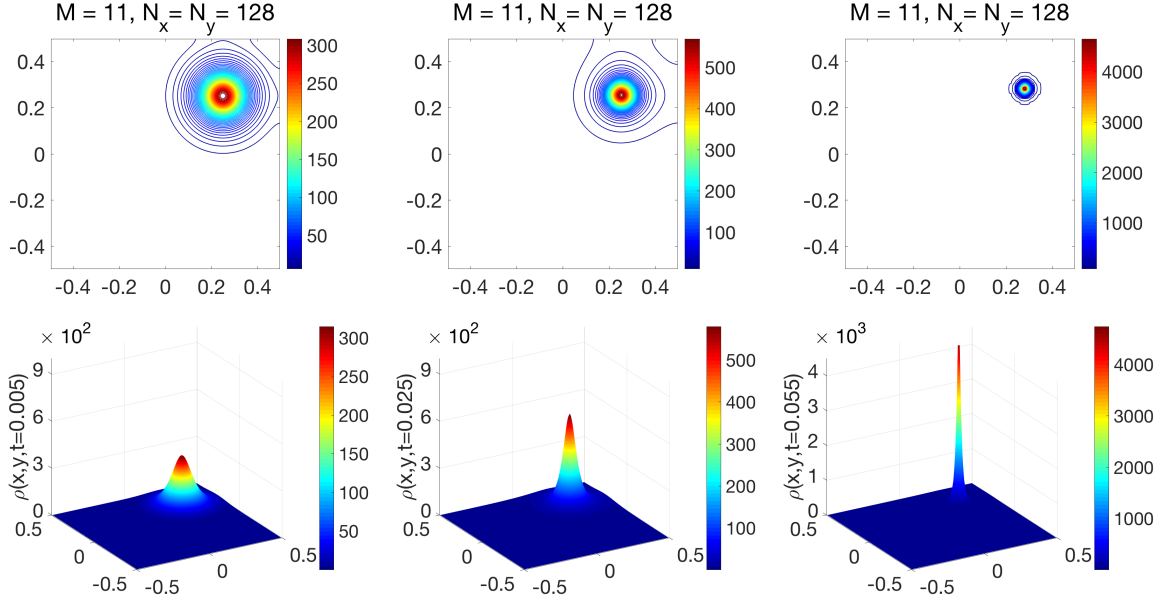


Figure 3.8 Example 3.3: The displacement of the density for $M = 11$.

3.6 Conclusions

In this chapter, we derived and studied a new asymptotic preserving method for the kinetic chemotaxis model in two space dimensions. For time evolution of the cell distribution we used the Boltzmann-type kinetic equation with a local turning kernel operator, which describes the change in cell orientation. For the chemoattractant both the elliptic and parabolic cases were considered. The Patlak-Keller-Segel model for chemotaxis can be recovered in the singular limit of the kinetic model, when the mean free path converges to 0. It is well-known that the solutions of both the kinetic and Patlak-Keller-Segel models may blow up in finite time, when the initial mass is larger than a critical mass. The critical values, however, are different for macroscopic and kinetic models.

Computing these blowing up solutions requires a reliable and efficient approximation of singular functions or distributions. Our numerical method was based on the so-called even-odd decoupling followed by the Strang splitting and a suitable combination of the evolution of the chemoattractant, relaxation and transport steps for the evolution of cell density. Using the splitting allows one to exactly solve the stiff relaxation system whereas

the transport system is linear and is numerically solved using an upwind approach. The macroscopic equations for the chemoattractant were treated by the spectral method.

We proved that as far as the global solution exists, our numerical scheme is asymptotic preserving and yields a consistent approximation of the Patlak-Keller-Segel model when the mean free path converges to 0. Our numerical experiments indicated that in the blowing up regime, the solutions of the kinetic chemotaxis and Patlak-Keller-Segel systems may behave differently. To the best of our knowledge, this does not contradict the theoretical results since after the blowup time the solutions can only be understood as measure-valued solutions for which no rigorous analysis is available. Moreover, in the numerical examples, we considered initial data which is not necessarily spherically symmetric. However, in the literature, the spherical symmetry is one of the assumptions for the existence of the solution to the kinetic chemotaxis model, see e.g. [15, 23].

In future work, we intend to study the kinetic model with global turning kernels and to analyze whether there is a global weak solution for both parabolic and elliptic chemoattractant equation for general two dimensional initial data.

BIBLIOGRAPHY

- [1] N. B. ABDALLAH, P. DEGOND, F. DELUZET, V. LATOCHA, R. TALAALOUT, AND M. VIGNAL, *Diffusion limits of kinetic models*, in Hyperbolic Problems: Theory, Numerics, Applications, Springer, 2003, pp. 3–17.
- [2] R. ABGRALL, *On essentially non-oscillatory schemes on unstructured meshes: analysis and implementation*, J. Comput. Phys., 114 (1994), pp. 45–58.
- [3] W. ALT, *Biased random walk models for chemotaxis and related diffusion approximations*, J. Math. Biol., 9 (1980), pp. 147–177.
- [4] P. ARMINJON, M.-C. VIALON, AND A. MADRANE, *A finite volume extension of the Lax-Friedrichs and Nessyahu-Tadmor schemes for conservation laws on unstructured grids*, Int. J. Comput. Fluid Dyn., 9 (1997), pp. 1–22.
- [5] E. AUDUSSE, F. BOUCHUT, M.-O. BRISTEAU, R. KLEIN, AND B. PERTHAME, *A fast and stable well-balanced scheme with hydrostatic reconstruction for shallow water flows*, SIAM J. Sci. Comput., 25 (2004), pp. 2050–2065.
- [6] A. AW AND M. RASCLE, *Resurrection of second order models of traffic flow*, SIAM J. Appl. Math., 60 (2000), pp. 916–944.
- [7] M. K. BANDA, M. HERTY, AND A. KLAR, *Gas flow in pipeline networks*, Netw. Heterog. Media, 1 (2006), pp. 41–56.
- [8] A. BELLOUQUID AND J. TAGOUDJEU, *An asymptotic preserving scheme for kinetic models for chemotaxis phenomena*, arXiv preprint arXiv:1507.05182, (2015).
- [9] M. BEN-ARTZI AND J. FALCOVITZ, *Generalized Riemann problems in computational fluid dynamics*, vol. 11 of Cambridge Monographs on Applied and Computational Mathematics, Cambridge University Press, Cambridge, 2003.
- [10] F. BIANCO, G. PUPPO, AND G. RUSSO, *High order central schemes for hyperbolic systems of conservation laws*, SIAM J. Sci. Comput., 21 (1999), pp. 294–322.
- [11] A. BOLLERMANN, G. CHEN, A. KURGANOV, AND S. NOELLE, *A well-balanced reconstruction of wet/dry fronts for the shallow water equations*, Journal of Scientific Computing, 56 (2013), pp. 267–290.
- [12] A. BOLLERMANN, S. NOELLE, AND M. LUKÁČOVÁ-MEDVIĐOVÁ, *Finite volume evolution Galerkin methods for the shallow water equations with dry beds*, Commun. Comput. Phys., 10 (2011), pp. 371–404.

- [13] N. BOTTA, R. KLEIN, S. LANGENBERG, AND S. LÜTZENKIRCHEN, *Well-balanced finite volume methods for nearly hydrostatic flows*, J. Comput. Phys., 196 (2004), pp. 539–565.
- [14] F. BOUCHUT, *Nonlinear stability of finite volume methods for hyperbolic conservation laws and well-balanced schemes for sources*, Frontiers in Mathematics, Birkhäuser Verlag, Basel, 2004.
- [15] N. BOURNAVEAS AND V. CALVEZ, *Critical mass phenomenon for a chemotaxis kinetic model with spherically symmetric initial data*, 26 (2009), pp. 1871–1895.
- [16] A. BRESSAN, S. CANIC, M. GARAVELLO, M. HERTY, AND B. PICCOLI, *Flow on networks: recent results and perspectives*, European Mathematical Society-Surveys in Mathematical Sciences, 1 (2014), pp. 47–11.
- [17] J. BROUWER, I. GASSER, AND M. HERTY, *Gas pipeline models revisited: Model hierarchies, nonisothermal models, and simulations of networks*, Multiscale Model. Simul., 9 (2011), pp. 601–623.
- [18] S. BRYSON, Y. EPSHTEYN, A. KURGANOV, AND G. PETROVA, *Well-balanced positivity preserving central-upwind scheme on triangular grids for the Saint-Venant system*, M2AN Math. Model. Numer. Anal., 45 (2011), pp. 423–446.
- [19] S. BRYSON, A. KURGANOV, D. LEVY, AND G. PETROVA, *Semi-discrete central-upwind schemes with reduced dissipation for Hamilton-Jacobi equations*, IMA J. Numer. Anal., 25 (2005), pp. 113–138.
- [20] S. BRYSON AND D. LEVY, *High-order semi-discrete central-upwind schemes for multi-dimensional Hamilton-Jacobi equations*, J. Comput. Phys., 189 (2003), pp. 63–87.
- [21] V. CALVEZ AND J. A. CARRILLO, *Volume effects in the Keller–Segel model: energy estimates preventing blow-up*, J. Math. Pures Appl. (9), 86 (2006), pp. 155–175.
- [22] V. CALVEZ, B. PERTHAME, AND M. SHARIFI TABAR, *Modified Keller–Segel system and critical mass for the log interaction kernel*, in Stochastic analysis and partial differential equations, vol. 429 of Contemp. Math., Amer. Math. Soc., Providence, RI, 2007, pp. 45–62.
- [23] J. A. CARRILLO AND B. YAN, *An asymptotic preserving scheme for the diffusive limit of kinetic systems for chemotaxis*, Multiscale Modeling & Simulation, 11 (2013), pp. 336–361.

- [24] F. A. CHALUB AND J. F. RODRIGUES, *A class of kinetic models for chemotaxis with threshold to prevent overcrowding*, Port. Math. (N.S.), 63 (2006), pp. 227–250.
- [25] F. A. C. C. CHALUB, P. A. MARKOWICH, B. PERTHAME, AND C. SCHMEISER, *Kinetic models for chemotaxis and their drift-diffusion limits*, Monatsh. Math., 142 (2004), pp. 123–141.
- [26] P. CHANDRASHEKAR AND C. KLINGENBERG, *A second order well-balanced finite volume scheme for Euler equations with gravity*, SIAM Journal on Scientific Computing, 37 (2015), pp. B382–B402.
- [27] A. CHERTOCK, S. CUI, A. KURGANOV, Ş. N. ÖZCAN, AND E. TADMOR, *Well-balanced central-upwind schemes for the Euler equations with gravitation*, (2015). Submitted.
- [28] A. CHERTOCK, S. CUI, A. KURGANOV, AND T. WU, *Well-balanced positivity preserving central-upwind scheme for the shallow water system with friction terms*, International Journal for numerical methods in fluids, 78 (2015), pp. 355–383.
- [29] A. CHERTOCK, M. DUDZINSKI, A. KURGANOV, AND M. LUKÁČOVÁ-MEDVIĐOVÁ, *Well-balanced schemes for the shallow water equations with Coriolis forces*, (2016). Submitted.
- [30] A. CHERTOCK, M. HERTY, AND Ş. N. ÖZCAN, *Well-balanced central-upwind schemes for 2×2 systems of balance laws*, (2016). Submitted.
- [31] A. CHERTOCK AND A. KURGANOV, *A positivity preserving central-upwind scheme for chemotaxis and haptotaxis models*, Numer. Math., 111 (2008), pp. 169–205.
- [32] A. CHERTOCK, A. KURGANOV, M. LUKÁČOVÁ-MEDVIĐOVÁ, AND Ş. N. ÖZCAN, *An asymptotic preserving scheme for kinetic chemotaxis models in two space dimensions*, (2017). Submitted.
- [33] A. CHERTOCK, A. KURGANOV, X. WANG, AND Y. WU, *On a chemotaxis model with saturated chemotactic flux*, Kinet. Relat. Models, 5 (2012), pp. 51–95.
- [34] S. CHILDRESS AND J. PERCUS, *Nonlinear aspects of chemotaxis*, Math. Biosci., 56 (1981), pp. 217–237.
- [35] I. CHRISTOV AND B. POPOV, *New nonoscillatory central schemes on unstructured triangulations for hyperbolic systems of conservation laws*, J. Comput. Phys., 227 (2008), pp. 5736–5757.

- [36] B. COCKBURN, C. JOHNSON, C.-W. SHU, AND E. TADMOR, *Advanced numerical approximation of nonlinear hyperbolic equations*, in CIME Lecture Notes, A. Quarteroni, ed., vol. 1697 of Lecture Notes in Mathematics, Springer-Verlag, 1998.
- [37] R. M. COLOMBO, *Hyperbolic phase transitions in traffic flow*, SIAM J. Appl. Math., 63 (2002), pp. 708–721 (electronic).
- [38] L. A. CONSTANTIN AND A. KURGANOV, *Adaptive central-upwind schemes for hyperbolic systems of conservation laws*, in Hyperbolic problems: theory, numerics, applications (Osaka, 2004), Yokohama Publishers, 2006, pp. 95–103.
- [39] A. CRESTETTO, N. CROUSEILLES, AND M. LEMOU, *Asymptotic-preserving scheme based on a finite volume/particle-in-cell coupling for Boltzmann-BGK-like equations in the diffusion scaling*, in Finite volumes for complex applications. VII. Elliptic, parabolic and hyperbolic problems, vol. 78 of Springer Proc. Math. Stat., Springer, Cham, 2014, pp. 827–835.
- [40] N. CROUSEILLES AND M. LEMOU, *An asymptotic preserving scheme based on a micro-macro decomposition for collisional Vlasov equations: Diffusion and high-field scaling limits*, Kinet. Relat. Models, 4 (2011), pp. 441–477.
- [41] A. DE SAINT-VENANT, *Théorie du mouvement non-permanent des eaux, avec application aux crues des rivières et à l'introduction des marées dans leur lit*, C.R. Acad. Sci. Paris, 73 (1871), pp. 147–154.
- [42] P. J. DELLAR AND R. SALMON, *Shallow water equations with a complete Coriolis force and topography*, Phys. Fluids, 17 (2005), pp. 106601–19.
- [43] V. DESVEAUX, M. ZENK, C. BERTHON, AND C. KLINGENBERG, *A well-balanced scheme to capture non-explicit steady states in the Euler equations with gravity*, Internat. J. Numer. Methods Fluids, 81 (2016), pp. 104–127.
- [44] G. DIMARCO AND L. PARESCHI, *Asymptotic preserving implicit-explicit Runge-Kutta methods for nonlinear kinetic equations*, SIAM J. Numer. Anal., 51 (2013), pp. 1064–1087.
- [45] C. EMAKO AND M. TANG, *Well-balanced and asymptotic preserving schemes for kinetic models*, arXiv preprint arXiv:1603.03171, (2016).
- [46] S. FAN, M. HERTY, AND B. SEIBOLD, *Comparative model accuracy of a data-fitted generalized Aw-Rascle-Zhang model*, Netw. Heterog. Media, 9 (2014), pp. 239–268.

- [47] F. FILBET AND S. JIN, *A class of asymptotic-preserving schemes for kinetic equations and related problems with stiff sources*, J. Comput. Phys., 229 (2010), pp. 7625–7648.
- [48] F. FILBET, P. LAURENÇOT, AND B. PERTHAME, *Derivation of hyperbolic models for chemosensitive movement*, Journal of Mathematical Biology, 50 (2005), pp. 189–207.
- [49] U. S. FJORDHOLM, S. MISHRA, AND E. TADMOR, *Well-balanced and energy stable schemes for the shallow water equations with discontinuous topography*, J. Comput. Phys., 230 (2011), pp. 5587–5609.
- [50] L. FORESTIER-COSTE, S. GÖTTLICH, AND M. HERTY, *Data-fitted second-order macroscopic production models*, SIAM journal on applied mathematics, 75 (2015), pp. 999–1014.
- [51] K. FRIEDRICHS, *Symmetric hyperbolic linear differential equations*, Comm. Pure Appl. Math., 7 (1954), pp. 345–392.
- [52] H. GAJEWSKI, K. ZACHARIAS, AND K. GRÖGER, *Global behaviour of a reaction-diffusion system modelling chemotaxis*, Mathematische Nachrichten, 195 (1998), pp. 77–114.
- [53] J. M. GALLARDO, C. PARÉS, AND M. CASTRO, *On a well-balanced high-order finite volume scheme for shallow water equations with topography and dry areas*, Journal of Computational Physics, 227 (2007), pp. 574–601.
- [54] T. GALLOUËT, J.-M. HÉRARD, AND N. SEGUIN, *Some approximate Godunov schemes to compute shallow water equations with topography*, Comput. & Fluids, 32 (2003), pp. 479–513.
- [55] M. GILES, *Analysis of the accuracy of shock-capturing in the steady quasi-1D-Euler equations*, Int. J. Comput. Fluid Dynam., 5 (1996), pp. 247–258.
- [56] E. GODLEWSKI AND P.-A. RAVIART, *Numerical approximation of hyperbolic systems of conservation laws*, vol. 118 of Applied Mathematical Sciences, Springer-Verlag, New York, 1996.
- [57] S. GODUNOV, *A difference method for numerical calculation of discontinuous solutions of the equations of hydrodynamics*, Mat. Sb. (N.S.), 47 (89) (1959), pp. 271–306.
- [58] S. GOTTLIEB, D. I. KETCHESON, AND C.-W. SHU, *Strong stability preserving Runge-Kutta and multistep time discretizations*, World Scientific Publishing Co. Pte. Ltd., Hackensack, NJ, 2011.
- [59] S. GOTTLIEB AND C.-W. SHU, *Total variation diminishing Runge-Kutta schemes*, Mathematics of computation of the American Mathematical Society, 67 (1998), pp. 73–85.

- [60] S. GOTTLIEB, C.-W. SHU, AND E. TADMOR, *Strong stability-preserving high-order time discretization methods*, SIAM Rev., 43 (2001), pp. 89–112.
- [61] J. M. GREENBERG AND A. Y. LEROUX, *A well-balanced scheme for the numerical processing of source terms in hyperbolic equations*, SIAM J. Numer. Anal., 33 (1996), pp. 1–16.
- [62] A. HARTEN, *High resolution schemes for hyperbolic conservation laws*, J. Comput. Phys., 49 (1983), pp. 357–393.
- [63] A. HARTEN, B. ENGQUIST, S. OSHER, AND S. CHAKRAVARTHY, *Uniformly high-order accurate essentially nonoscillatory schemes. III*, J. Comput. Phys., 71 (1987), pp. 231–303.
- [64] A. HARTEN AND S. OSHER, *Uniformly high-order accurate nonoscillatory schemes. I*, SIAM J. Numer. Anal., 24 (1987), pp. 279–309.
- [65] M. HERRERO AND J. VELÁZQUEZ, *A blow-up mechanism for a chemotaxis model*, Ann. Scuola Normale Superiore, 24 (1997), pp. 633–683.
- [66] M. A. HERRERO, E. MEDINA, AND J. VELÁZQUEZ, *Finite-time aggregation into a single point in a reaction-diffusion system*, Nonlinearity, 10 (1997), p. 1739.
- [67] M. A. HERRERO AND J. J. VELÁZQUEZ, *Chemotactic collapse for the Keller–Segel model*, Journal of Mathematical Biology, 35 (1996), pp. 177–194.
- [68] T. HILLEN AND H. G. OTHMER, *The diffusion limit of transport equations derived from velocity-jump processes*, SIAM J. Appl. Math., 61 (2000), pp. 751–775 (electronic).
- [69] T. HILLEN AND K. PAINTER, *Global existence for a parabolic chemotaxis model with prevention of overcrowding*, Adv. in Appl. Math., 26 (2001), pp. 280–301.
- [70] T. HILLEN AND K. PAINTER, *A user’s guide to PDE models for chemotaxis*, J. Math. Biol., 58 (2009), pp. 183–217.
- [71] D. HORSTMANN, *From 1970 until present: The Keller–Segel model in chemotaxis and its consequences I*, Jahresber. DMV, 105 (2003), pp. 103–165.
- [72] ———, *From 1970 until now: The Keller–Segel model in chemotaxis and its consequences II*, Jahresber. DMV, 106 (2004), pp. 51–69.
- [73] J. HU, S. JIN, AND Q. LI, *Asymptotic-preserving schemes for multiscale hyperbolic and kinetic equations*, Handbook of Numerical Analysis, (2016).

- [74] J. HU, S. JIN, AND L. WANG, *An asymptotic-preserving scheme for the semiconductor Boltzmann equation with two-scale collisions: A splitting approach*, Kinet. Relat. Models, 8 (2015), pp. 707–723.
- [75] J. HU, Q. LI, AND L. PARESCHI, *Asymptotic-preserving exponential methods for the quantum Boltzmann equation with high-order accuracy*, J. Sci. Comput., 62 (2015), pp. 555–574.
- [76] H. J. HWANG, K. KANG, AND A. STEVENS, *Drift-diffusion limits of kinetic models for chemotaxis: a generalization*, Discrete Contin. Dyn. Syst. Ser. B, 5 (2005), pp. 319–334.
- [77] ———, *Global solutions of nonlinear transport equations for chemosensitive movement*, SIAM journal on mathematical analysis, 36 (2005), pp. 1177–1199.
- [78] W. JÄGER AND S. LUCKHAUS, *On explosions of solutions to a system of partial differential equations modelling chemotaxis*, Transactions of the american mathematical society, 329 (1992), pp. 819–824.
- [79] J. JANG, F. LI, J.-M. QIU, AND T. XIONG, *Analysis of asymptotic preserving DG-IMEX schemes for linear kinetic transport equations in a diffusive scaling*, SIAM J. Numer. Anal., 52 (2014), pp. 2048–2072.
- [80] G.-S. JIANG AND C.-W. SHU, *Efficient implementation of weighted ENO schemes*, J. Comput. Phys., 126 (1996), pp. 202–228.
- [81] G.-S. JIANG AND E. TADMOR, *Nonoscillatory central schemes for multidimensional hyperbolic conservation laws*, SIAM J. Sci. Comput., 19 (1998), pp. 1892–1917 (electronic).
- [82] S. JIN, *Efficient asymptotic-preserving (ap) schemes for some multiscale kinetic equations*, SIAM Journal on Scientific Computing, 21 (1999), pp. 441–454.
- [83] S. JIN, *A steady-state capturing method for hyperbolic systems with geometrical source terms*, M2AN Math. Model. Numer. Anal., 35 (2001), pp. 631–645.
- [84] ———, *Asymptotic preserving (AP) schemes for multiscale kinetic and hyperbolic equations: A review*, Riv. Mat. Univ. Parma, 3 (2012), pp. 177–2016.
- [85] S. JIN, L. PARESCHI, AND G. TOSCANI, *Diffusive relaxation schemes for multiscale discrete-velocity kinetic equations*, SIAM J. Numer. Anal., 35 (1998), pp. 2405–2439 (electronic).

- [86] S. JIN AND X. WEN, *Two interface-type numerical methods for computing hyperbolic systems with geometrical source terms having concentrations*, SIAM J. Sci. Comput., 26 (2005), pp. 2079–2101 (electronic).
- [87] E. F. KELLER AND L. A. SEGEL, *Initiation of slime mold aggregation viewed as an instability*, J. Theor. Biol., 26 (1970), pp. 399–415.
- [88] ———, *Model for chemotaxis*, J. Theor. Biol., 30 (1971), pp. 225–234.
- [89] ———, *Traveling bands of chemotactic bacteria: A theoretical analysis*, J. Theor. Biol., 30 (1971), pp. 235–248.
- [90] D. KRÖNER, *Numerical schemes for conservation laws*, Wiley-Teubner Series Advances in Numerical Mathematics, John Wiley & Sons Ltd., Chichester, 1997.
- [91] A. KURGANOV AND D. LEVY, *Third-order semi-discrete central scheme for conservation laws and convection-diffusion equations*, SIAM J. Sci. Comput., 22 (2000), pp. 1461–1488.
- [92] ———, *Central-upwind schemes for the Saint-Venant system*, M2AN Math. Model. Numer. Anal., 36 (2002), pp. 397–425.
- [93] A. KURGANOV AND C.-T. LIN, *On the reduction of numerical dissipation in central-upwind schemes*, Commun. Comput. Phys., 2 (2007), pp. 141–163.
- [94] A. KURGANOV AND M. LUKÁČOVÁ-MEDVIĐOVÁ, *Numerical study of two-species chemotaxis models*, Discrete Contin. Dyn. Syst. Ser. B, 19 (2014), pp. 131–152.
- [95] A. KURGANOV, S. NOELLE, AND G. PETROVA, *Semi-discrete central-upwind scheme for hyperbolic conservation laws and Hamilton-Jacobi equations*, SIAM J. Sci. Comput., 23 (2001), pp. 707–740.
- [96] A. KURGANOV AND G. PETROVA, *Central schemes and contact discontinuities*, M2AN Math. Model. Numer. Anal., 34 (2000), pp. 1259–1275.
- [97] ———, *A third-order semi-discrete genuinely multidimensional central scheme for hyperbolic conservation laws and related problems*, Numer. Math., 88 (2001), pp. 683–729.
- [98] ———, *Central-upwind schemes on triangular grids for hyperbolic systems of conservation laws*, Numer. Methods Partial Differential Equations, 21 (2005), pp. 536–552.
- [99] ———, *Adaptive central-upwind schemes for Hamilton-Jacobi equations with non-convex hamiltonians*, J. Sci. Comput., 27 (2006), pp. 323–333.

- [100] —, *A second-order well-balanced positivity preserving central-upwind scheme for the Saint-Venant system*, Commun. Math. Sci., 5 (2007), pp. 133–160.
- [101] —, *A central-upwind scheme for nonlinear water waves generated by submarine landslides*, in Hyperbolic problems: theory, numerics, applications (Lyon 2006), S. Benzoni-Gavage and D. Serre, eds., Springer, 2008, pp. 635–642.
- [102] A. KURGANOV, G. PETROVA, AND B. POPOV, *Adaptive semi-discrete central-upwind schemes for nonconvex hyperbolic conservation laws*, SIAM J. Sci. Comput., 29 (2007), pp. 2381–2401.
- [103] A. KURGANOV AND E. TADMOR, *New high resolution central schemes for nonlinear conservation laws and convection-diffusion equations*, J. Comput. Phys., 160 (2000), pp. 241–282.
- [104] —, *New high-resolution semi-discrete central scheme for Hamilton–Jacobi equations*, J. Comput. Phys., 160 (2000), pp. 720–742.
- [105] —, *Solution of two-dimensional Riemann problems for gas dynamics without Riemann problem solvers*, Numer. Methods Partial Differential Equations, 18 (2002), pp. 584–608.
- [106] P. LAX, *Weak solutions of nonlinear hyperbolic equations and their numerical computation*, Comm. Pure Appl. Math., 7 (1954), pp. 159–193.
- [107] M. LEMOU AND L. MIEUSSSENS, *A new asymptotic preserving scheme based on micro-macro formulation for linear kinetic equations in the diffusion limit*, SIAM J. Sci. Comput., 31 (2008), pp. 334–368.
- [108] R. LEVEQUE, *Balancing source terms and flux gradients in high-resolution Godunov methods: The quasi-steady wave-propagation algorithm*, J. Comput. Phys., 146 (1998), pp. 346–365.
- [109] —, *Finite volume methods for hyperbolic problems*, Cambridge Texts in Applied Mathematics, Cambridge University Press, Cambridge, 2002.
- [110] R. LEVEQUE AND D. BALE, *Wave propagation methods for conservation laws with source terms*, Internat. Ser. of Numer. Math., 130 (1999), pp. 609–618.
- [111] D. LEVY, G. PUPPO, AND G. RUSSO, *Central WENO schemes for hyperbolic systems of conservation laws*, M2AN Math. Model. Numer. Anal., 33 (1999), pp. 547–571.
- [112] —, *Compact central WENO schemes for multidimensional conservation laws*, SIAM J. Sci. Comput., 22 (2000), pp. 656–672 (electronic).

- [113] G. LI AND Y. XING, *High order finite volume WENO schemes for the Euler equations under gravitational fields*, J. Comput. Phys., 316 (2016), pp. 145–163.
- [114] K.-A. LIE AND S. NOELLE, *An improved quadrature rule for the flux-computation in staggered central difference schemes in multidimensions*, J. Sci. Comput., 63 (2003), pp. 1539–1560.
- [115] ———, *On the artificial compression method for second-order nonoscillatory central difference schemes for systems of conservation laws*, SIAM J. Sci. Comput., 24 (2003), pp. 1157–1174.
- [116] M. J. LIDTHILL AND G. B. WHITHAM, *On kinematic waves. II. A theory of traffic flow on long crowded roads*, Proc. Roy. Soc. London. Ser. A., 229 (1955), pp. 317–345.
- [117] S. LIOTTA, V. ROMANO, AND G. RUSSO, *Central schemes for balance laws of relaxation type*, SIAM J. Numer. Anal., 38 (2000), pp. 1337–1356.
- [118] X.-D. LIU AND S. OSHER, *Nonoscillatory high order accurate self-similar maximum principle satisfying shock capturing schemes. I*, SIAM J. Numer. Anal., 33 (1996), pp. 760–779.
- [119] X.-D. LIU, S. OSHER, AND T. CHAN, *Weighted essentially non-oscillatory schemes*, J. Comput. Phys., 115 (1994), pp. 200–212.
- [120] X.-D. LIU AND E. TADMOR, *Third order nonoscillatory central scheme for hyperbolic conservation laws*, Numer. Math., 79 (1998), pp. 397–425.
- [121] J. LUO, K. XU, AND N. LIU, *A well-balanced symplecticity-preserving gas-kinetic scheme for hydrodynamic equations under gravitational field*, SIAM J. Sci. Comput., 33 (2011), pp. 2356–2381.
- [122] G. I. MARCHUK, *Metody rasshchepleniya*, (Russian) [Splitting Methods] “Nauka”, Moscow, 1988.
- [123] ———, *Splitting and alternating direction methods*, in Handbook of numerical analysis, Vol. I, Handb. Numer. Anal., I, North-Holland, Amsterdam, 1990, pp. 197–462.
- [124] T. NAGAI, *Blowup of nonradial solutions to parabolic-elliptic systems modeling chemotaxis in two-dimensional domains*, J. Inequal. Appl., 6 (2001), pp. 37–55.
- [125] C. NEGULESCU, *Asymptotic-preserving schemes. Modeling, simulation and mathematical analysis of magnetically confined plasmas*, Rivista di Matematica della Università di Parma, 4 (2013), pp. 265–343.

- [126] H. NESSYAHU AND E. TADMOR, *Nonoscillatory central differencing for hyperbolic conservation laws*, J. Comput. Phys., 87 (1990), pp. 408–463.
- [127] S. NOELLE, Y. XING, AND C.-W. SHU, *High-order well-balanced schemes*, in Numerical methods for balance laws, vol. 24 of Quad. Mat., Dept. Math., Seconda Univ. Napoli, Caserta, 2009, pp. 1–66.
- [128] A. OSIADACZ, *Simulation and analysis of gas networks*, Gulf Publishing Company, Houston, 1989.
- [129] H. OTHMER, S. DUNBAR, AND W. ALT, *Models of dispersal in biological systems*, J. Math. Biol., 26 (1988), pp. 263–298.
- [130] H. G. OTHMER AND T. HILLEN, *The diffusion limit of transport equations II: Chemotaxis equations*, SIAM J. Appl. Math., 62 (2002), pp. 1222–1250 (electronic).
- [131] L. PARESCHI, *Central differencing based numerical schemes for hyperbolic conservation laws with relaxation terms*, SIAM J. Numer. Anal., 39 (2001), pp. 1395–1417.
- [132] L. PARESCHI, G. PUPPO, AND G. RUSSO, *Central Runge-Kutta schemes for conservation laws*, SIAM J. Sci. Comput., 26 (2005), pp. 979–999 (electronic).
- [133] L. PARESCHI AND G. RUSSO, *Implicit-Explicit Runge-Kutta schemes and applications to hyperbolic systems with relaxation*, J. Sci. Comput., 25 (2005), pp. 129–155.
- [134] C. PATLAK, *Random walk with persistence and external bias*, Bull. Math: Biophys., 15 (1953), pp. 311–338.
- [135] B. PERTHAME, *PDE models for chemotactic movements: parabolic, hyperbolic and kinetic*, Appl. Math., 49 (2004), pp. 539–564.
- [136] B. PERTHAME AND C. SIMEONI, *A kinetic scheme for the Saint-Venant system with a source term*, Calcolo, 38 (2001), pp. 201–231.
- [137] M. RICCHIUTO AND A. BOLLERMANN, *Stabilized residual distribution for shallow water simulations*, Journal of Computational Physics, 228 (2009), pp. 1071–1115.
- [138] G. RUSSO, *Central schemes for conservation laws with application to shallow water equations*, in Trends and Applications of Mathematics to Mechanics, Springer Milan, 2005, pp. 225–246.
- [139] ———, *High-order shock-capturing schemes for balance laws*, in Numerical solutions of partial differential equations, Adv. Courses Math. CRM Barcelona, Birkhäuser, Basel, 2009, pp. 59–147.

- [140] G. RUSSO AND A. KHE, *High order well-balanced schemes based on numerical reconstruction of the equilibrium variables*, in *Waves and Stability in Continuous Media*, vol. 1, 2010, pp. 230–241.
- [141] J. SHI, C. HU, AND C.-W. SHU, *A technique of treating negative weights in WENO schemes*, *J. Comput. Phys.*, 175 (2002), pp. 108–127.
- [142] C.-W. SHU, *Total-variation-diminishing time discretizations*, *SIAM J. Sci. Comput.*, 6 (1988), pp. 1073–1084.
- [143] ———, *High-order finite difference and finite volume WENO schemes and discontinuous Galerkin methods for CFD*, *Int. J. Comput. Fluid Dyn.*, 17 (2003), pp. 107–118.
- [144] C.-W. SHU AND S. OSHER, *Efficient implementation of essentially non-oscillatory shock-capturing schemes*, *J. Comput. Phys.*, 77 (1988), pp. 439–471.
- [145] A. STEVENS AND H. G. OTHMER, *Aggregation, blowup, and collapse: the abc's of taxis in reinforced random walks*, *SIAM Journal on Applied Mathematics*, 57 (1997), pp. 1044–1081.
- [146] G. STRANG, *On the construction and comparison of difference schemes*, *SIAM J. Numer. Anal.*, 5 (1968), pp. 506–517.
- [147] D. W. STROOCK, *Some stochastic processes which arise from a model of the motion of a bacterium*, *Probability Theory and Related Fields*, 28 (1974), pp. 305–315.
- [148] P. SWEBY, *High resolution schemes using flux limiters for hyperbolic conservation laws*, *SIAM J. Numer. Anal.*, 21 (1984), pp. 995–1011.
- [149] C. T. TIAN, K. XU, K. L. CHAN, AND L. C. DENG, *A three-dimensional multidimensional gas-kinetic scheme for the Navier-Stokes equations under gravitational fields*, *J. Comput. Phys.*, 226 (2007), pp. 2003–2027.
- [150] E. TORO, *Riemann solvers and numerical methods for fluid dynamics: A practical introduction*, Springer-Verlag, Berlin, Heidelberg, third ed., 2009.
- [151] R. TOUMA, U. KOLEY, AND C. KLINGENBERG, *Well-balanced unstaggered central schemes for the Euler equations with gravitation*, *SIAM J. Sci. Comput.*, 38 (2016), pp. B773–B807.
- [152] B. VAN LEER, *Towards the ultimate conservative difference scheme. V. A second-order sequel to Godunov's method*, *J. Comput. Phys.*, 32 (1979), pp. 101–136.

- [153] N. VAUCHELET, *Kinetic description and asymptotics for bacterial chemotaxis*, IFAC Proceedings Volumes, 46 (2013), pp. 269–274.
- [154] Y. XING AND C.-W. SHU, *High order well-balanced WENO scheme for the gas dynamics equations under gravitational fields*, J. Sci. Comput., 54 (2013), pp. 645–662.
- [155] Y. XING, C.-W. SHU, AND S. NOELLE, *On the advantage of well-balanced schemes for moving-water equilibria of the shallow water equations*, J. Sci. Comput., 48 (2011), pp. 339–349.
- [156] K. XU, J. LUO, AND S. CHEN, *A well-balanced kinetic scheme for gas dynamic equations under gravitational field*, Adv. Appl. Math. Mech., 2 (2010), pp. 200–210.
- [157] H. C. YEE, *A class of high-resolution explicit and implicit shock-capturing methods*, (1989).

APPENDIX

APPENDIX A

Time Integration

A.1 The Third-Order Strong Stability Preserving Runge-Kutta Methods

We consider the following ODE system:

$$\frac{d}{dt}\mathbf{q} = \mathcal{L}(\mathbf{q}), \tag{A.1}$$

where \mathbf{q} is the vector of unknowns and \mathcal{L} is the spatial discretization.

To solve the system (A.1) in a highly accurate and stable way, we choose the three-stage third-order strong stability preserving (SSP) Runge-Kutta method (see for the details, e.g., [58–60, 142, 144]) which is a convex combination of forward Euler steps:

$$\begin{aligned}
\mathbf{q}_{(0)} &= \mathbf{q}^n, \\
\mathbf{q}_{(1)} &= \mathbf{q}_{(0)} + \Delta t \mathcal{L}(\mathbf{q}_{(0)}), \\
\mathbf{q}_{(2)} &= \frac{3}{4}\mathbf{q}_{(0)} + \frac{1}{4}\mathbf{q}_{(1)} + \frac{1}{4}\Delta t \mathcal{L}(\mathbf{q}_{(1)}), \\
\mathbf{q}^{n+1} &= \frac{1}{3}\mathbf{q}_{(0)} + \frac{2}{3}\mathbf{q}_{(2)} + \frac{2}{3}\Delta t \mathcal{L}(\mathbf{q}_{(2)}),
\end{aligned} \tag{A.2}$$

where $\mathbf{q}^n = \mathbf{q}(\cdot, t^n)$.

Remark A.1.1 Recall that the SSP Runge-Kutta method has been used for time integration of the semi-discrete schemes described in Sections 2.1.1, 2.1.2 and 3.3.2.2.

For instance, in the case of 1-D discretization of the scheme in (2.2), the system (A.1) is to be replaced by

$$\frac{d}{dt} \bar{\mathbf{q}}_j = -\frac{\mathcal{F}_{j+\frac{1}{2}} - \mathcal{F}_{j-\frac{1}{2}}}{\Delta x} + \bar{\mathbf{S}}_j, \tag{A.3}$$

with the corresponding numerical fluxes and source term for each $j = j_L, \dots, j_R$.

Similarly, in the 2-D scheme (2.12), the system (A.1) is given as:

$$\frac{d}{dt} \bar{\mathbf{q}}_{j,k} = -\frac{\mathcal{F}_{j+\frac{1}{2},k} - \mathcal{F}_{j-\frac{1}{2},k}}{\Delta x} - \frac{\mathcal{G}_{j,k+\frac{1}{2}} - \mathcal{G}_{j,k-\frac{1}{2}}}{\Delta y} + \bar{\mathbf{S}}_{j,k}, \tag{A.4}$$

for $j = j_L, \dots, j_R$ and $k = k_L, \dots, k_R$.

Lastly, the SSP Runge-Kutta method is applied to solve the system (3.36) with the following modification in (A.1):

$$\frac{d}{dt} \mathbf{q}_{i,j,k} = -A_1^+(\mathbf{q}_x^-)_{i,j,k} - A_1^-(\mathbf{q}_x^+)_{i,j,k} - A_2^+(\mathbf{q}_y^-)_{i,j,k} - A_2^-(\mathbf{q}_y^+)_{i,j,k}, \tag{A.5}$$

for each $i = 1, \dots, N_x$, $j = 1, \dots, N_y$, and $k = 1, \dots, N_\theta$.